Amplification of
optically driven phonons

Dissertation

zur Erlangung des Doktorgrades an der Fakultät für

Mathematik, Informatik und Naturwissenschaften

Fachbereich Physik

der Universität Hamburg

Vorgelegt vor

Andrea Cartella

aus Brescia, Italien

Hamburg

2017

Gutachter/in der Dissertation:	Prof. Dr. Andrea Cavalleri
	Prof. Dr. Daniela Pfannkuche
Zusammensetzung der Prüfungsauscommission:	Prof. Dr. Andrea Cavalleri
	Prof. Dr. Daniela Pfannkuche
	Prof. Dr. Wilfried Wurth
	Prof. Dr. Franz Kärtner
	Prof. Dr. Michael Rübhausen
Datum der Disputation:	04/05/2018
Vorsitzender des Prüfungsausschusses:	Prof. Dr. Michael Rübhausen
Vorsitzender des Promotionsausschusses:	Prof. Dr. Wolfgang Hansen
Dekan der Fakultät MIN:	Prof. Dr. Heinrich Graener
Leiter des Fachbereich Physik:	Prof. Dr. Michael Potthoff

Hiermit erkläre ich an Eides statt, dass ich die vorliegende Dissertationsschrift selbst verfasst und keine anderen als die angegebenen Quellen und Hilfsmittel benutzt habe. Diese Arbeit lag noch keiner anderen Person oder Prüfungsbehörde im Rahmen einer Prüfung vor.

I hereby declare, on oath, that I have written the present dissertation on my own and have not used other than the mentioned resources and aids. This work has never been presented to other persons or evaluation panels in the context of an examination.

<div align="right">

Andrea Cartella

Hamburg, 2017

</div>

Untershift / Signature:

Datum / Date:

for Elena and my parents

Abstract

The amplification of light has had an exceptional impact on both science and technology. The amplification of other bosonic excitations, like phonons or magnons, is also believed to uncover new important physical phenomena. In particular, the amplification of resonantly driven optical phonons which are of great interest due to their connection to structural phase transitions has not been experimentally demonstrated yet. The aim of this thesis is the investigation of the possibility to amplify optically driven lattice vibrations.

To this end, coherent mid-infrared optical pulses were used to resonantly excite large amplitude oscillations of the Si-C stretching mode in silicon carbide. Upon this excitation, the reflectivity at all wavelengths throughout the reststrahlen band was observed to increase above one, as probed by second time-delayed pulses. This striking result evidences the amplification of the probe pulse, and, by extension, that of the optical phonon itself.

The microscopic mechanism for this phonon amplification is understood in terms of the anharmonic response of the driven mode. Because of the large amplitude ionic displacement, the high frequency permittivity and the phonon oscillator strength, which are constant in the linear regime, reveal quadratic dependence on the phonon coordinate. This makes them oscillate at twice the frequency of the exciting light field and act as a parametric drive in the equation of motion for the lattice dynamics. This model was implemented in finite difference time domain simulations, which reproduced well the experimental results.

Overall, the present study reports on the first experimental evidence of optical phonons parametric amplification, and provides a deeper insight into nonlinear lattice dynamics.

Zusammenfassung

Die Verstärkung von Licht beeinflusst Wissenschaft und Technik in einer außergewöhnlichen Weise. Ähnlich wichtige neue physikalische Phänomene werden von der Möglichkeit der Verstärkung anderer bosonischer Quantenobjekte wie zum Beispiel Phononen und Magnonen erwartet. Insbesondere die Verstärkung resonant getriebener optischer Phononen, die aufgrund ihrer Verbindung zu strukturellen Phasenübergänge von besonderer Bedeutung sind, wurde bis heute nicht experimentell nachgewiesen. Das Ziel der vorliegenden Arbeit ist es, diese Möglichkeit der Verstärkung optisch angeregter Gitterschwingungen zu erforschen.

Zu diesem Zweck wurden kohärente mittelinfrarote Lichtpulse zur resonanten Anregung der Si-C Dehnungsmode in Siliziumcarbid genutzt. Diese Anregung führte zu einer Erhöhung der Reflektivität größer als eins bei allen Wellenlängen innerhalb des Reststrahlenbandes, wie durch zeitverzögerte optische Pulse gemessen wurde. Dieses Ergebnis beweist die Verstärkung der Abfragepulse, und damit einhergehend die Verstärkung des optischen Phonons selbst.

Der mikroskopische Mechanismus dieser Phononverstärkung kann im Sinne einer anharmonischen Antwort der angeregten Mode verstanden werden. Aufgrund der großen Amplitude der Auslenkung der Gitterionen erfahren sowohl die Dielektrizitätszahl bei hohen Frequenzen als auch die Oszillatorstärke des Phonons, die in der linearen Systemantwort jeweils konstant sind, eine quadratische Abhängigkeit von der Phononkoordinate. Dadurch oszillieren diese Größen bei der doppelten Frequenz des eingestrahlten Lichtfeldes und wirken entsprechend als parametrische Kraft auf das Kristallgitter. Dieses Modell wurde in einer Simulation nach der Finite-

Differenzen-Methode im Zeitbereich implementiert, welche die experimentellen Ergebnisse reproduzierte.

Insgesamt berichtet die vorliegende Arbeit den ersten experimentellen Nachweis der parametrischen Verstärkung optischer Phononen und gibt damit einen tiefen Einblick in die nichtlineare Gitterdynamik von Festkörpern.

Table of contents

Table of contents

Introduction

Amplification of light has changed dramatically the 20th century science and technology. Stimulated emission of photons led for example to the development of lasers [1], which are nowadays ubiquitous in the everyday life of billions of people. Shortly after the construction of the first laser, the drastically increased available light intensities allowed to uncover other mechanisms for light amplification. Such mechanisms are based on the nonlinear response of optical media [2], like optical parametric amplification, and are routinely employed for the frequency conversion of intense laser pulses and in four wave mixing processes.

The amplification of other bosonic excitations like phonons or magnons is likely to have an equally transformative impact on modern condensed matter physics and technology.

In particular, the ability to amplify and control such collective excitations with light fields paved the way for the explorations of new interesting physical phenomena. For example the amplification of spin waves through parametric pumping with microwaves has led to remarkable fundamental discoveries, leading to the high-temperature condensation of magnons [3], as well as to applicative spintronics-oriented studies aimed at the control of spin currents on the micrometer scale [4].

Phonons and their fluctuations are related to fundamental quantum

physical phenomena like squeezed states [5, 6], and to structural phase transitions [7] that can in principle be functionalized. The manipulation of phonon fluctuations close to such phase transitions, as well as their amplification, is therefore a possible new way of controlling interesting material properties. The amplification of acoustic [8, 9] and optical [10] phonons under intense laser and magnetic fields has been long studied theoretically. Acoustic mode amplification has been reported experimentally, for example in semiconductor superlattices driven by electrical currents [11] or bias voltages [12], and in optically excited ruby [13]. Optical phonons, on the other hand, have been successfully amplified only by drifting electrons in semiconductor nanostructures [14].

It is the aim of this thesis to investigate the possibility of amplifying optically driven lattice vibrations. The amplification of resonantly driven optical phonons is notably interesting, as the lattice vibrations amplitude plays a pivotal role in strong-field optical excitation capable of controlling material's functionalities. The melting of magnetic order [15, 16], light induced superconductivity [17, 18, 19, 20] and insulator to metal transitions [21, 22] have been induced by the strong resonant excitation of optical phonons with intense light fields. Additionally, pairs of lattice vibrations optically driven to large amplitudes were proven to induce effective magnetic fields to control magnons [23]. Many of these results are understood in the framework of nonlinear phononics [24, 25, 26, 27], a recently disclosed rich playground where the anharmonic coupling of the pumped phonon modes to other degrees of freedom allows for the material's control. In this context, however, the possible anharmonic response of the driven mode itself has so far been overlooked.

Indeed, for very large vibrational amplitudes in the range of few per-

cent of the interatomic distances, the response of the driven phonon can be expected to become anharmonic [28]. Such anharmonic response might uncover a series of higher order nonlinear phononics phenomena, among which the parametric amplification of the mode itself. This effect could increase the vibrational lattice oscillations, with potential performative improvements of the nonlinear-phononics-based material control.

In a more general context, phononic parametric amplification would extend the parallelism between the amplification of phonons and that of photons.The anharmonic phonon response may be conducive to a series of *phononic counterparts* of various optical nonlinearities, such as phononic four wave mixing or soliton formation, capable of coherently transferring energy among lattice modes or leading to mechanical waves propagating without damping inside materials.

Structure of the thesis

In this thesis the nonlinear response of optically driven phonons is investigated in the Si-C stretching mode of the prototypical dielectric silicon carbide. Chapter 1 presents the optical properties of infrared active phonons as they are deduced from the Lorentz model. In chapter 2 the nonlinear phonon response is modeled as an higher order expansion of such model supported by first principle DFT calculations, and is shown to suggest the onset of phonon amplification. This theoretical prediction is validated experimentally in chapter 3 with time-resolved time-domain-spectroscopy, a technique suitably extended to cover the interesting frequency region extending up to 33 THz. In chapter 4 the pump-probe response of SiC based on the model of chapter 2 is simulated in the framework of FDTD, showing

good agreement with the experimental results and confirming the hypothesis of optical phonon amplification.

Details on the experimental methods and on the implementation of FDTD to simulate the pump-probe response of SiC are to be found in appendices A and B, respctively.

Finally, appendices C and D report optical developments aimed at the control of the spectral phase and bandwidth, respectively, of laser pulses analogous to those used in the experiments presented in the main body of the thesis.

Chapter 1

Linear optical properties of IR-active phonons

The interaction of light with an infrared active optical phonon in the linear regime is described by the Lorentz model, where the phonon is treated like a charged harmonic oscillator which is set in motion by the light alternating electric field. This lays the foundation stone for the investigation of the nonlinear phonon dynamics carried out in this thesis, as the response of the lattice to very intense laser pulses will be studied in terms of an extension to this model. For this reason, the first chapter describes the linear light-phonon interaction, reporting the equations governing the lattice dynamics and the resulting optical properties that can be measured in the experiments.

1.1   Infrared active phonons

Crystals are characterized by a periodic arrangement of atoms in the three dimensional space, known as the crystal lattice. If one atom is displaced

from its equilibrium position, it is subjected to interatomic restoring forces, which maintain the solid together [29]. In the *harmonic approximation*, valid for small displacments x, such restoring forces F are considered linearly proportional to the displacement, $F = -\gamma x$. Thus, upon displacement, the atoms oscillate around their equilibrium positions with some specific frequencies. Furthermore, because of the interatomic forces the atoms cannot vibrate independently from one another, and can be treated as a set of coupled oscillators whose vibrations can be described as superposition of normal modes, often referred to as phonons. A phonon is formally defined as a quantum of vibrational energy arising from the oscillation of atoms within a crystal. However, when crystals interact with light, the occupation number is usually high enough so that the phonon population can be treated classically. For this reason from now on the term phonon will be used referring to vibrational normal modes.

The behavior of atoms vibrating along one normal mode coordinate can be described by a simple model, consisting of a set of spheres connected by springs. Figure 1.1 shows the example case of a diatomic chain in which neighbouring spheres have different masses. Assuming that each sphere is only interacting with its nearest neighbours, the equations of motions for the spheres of the n-th cell can be written as follows:

$$
\begin{aligned}
m\frac{\partial^2 a_n}{\partial t^2} &= \gamma\left(b_n + b_{n-1} - 2a_n\right) \\
M\frac{\partial^2 b_n}{\partial t^2} &= \gamma\left(a_{n+1} + a_n - 2b_n\right).
\end{aligned}
\tag{1.1}
$$

These equations allow for travelling wave solutions of the form:

$$
a_n = a e^{i(nkd - \omega t)} \qquad b_n = b e^{i(nkd - \omega t)}
\tag{1.2}
$$
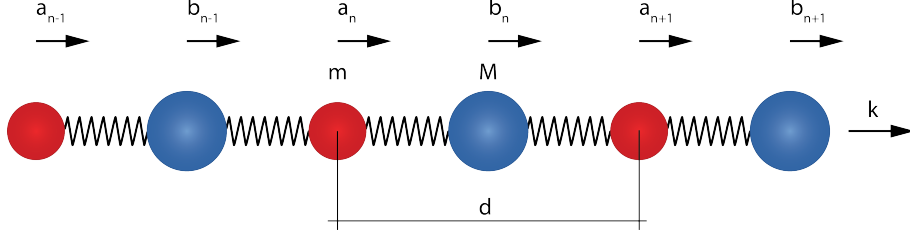
Figure 1.1: Diatomic chain of atoms represented as a set of spheres with different masses m and M, connected by springs with force constant γ. The unit cells are labeled by the index n, and the displacement of the spheres within each cell with respect to their equilibrium positions are labeled a and b.

where d is the distance between two spheres with the same mass, k is the wavevector and ω the frequency. Substituting these into equations 1.1 leads to:

$$-m\omega^2 a = \gamma b \left(1 + e^{+ikd}\right) - 2\gamma a \tag{1.3}$$

$$-M\omega^2 b = \gamma a \left(1 + e^{-ikd}\right) - 2\gamma b. \tag{1.4}$$

The solution of these equations gives:

$$mM\omega^4 - 2\gamma(m + M)\omega^2 + 2\gamma^2 \left[1 - \cos(kd)\right] = 0, \tag{1.5}$$

which is the phonon dispersion curve. The solutions relevant for the description of the phonons interaction with light are those for which $k \approx 0$, since the momentum carried by light is very small. In this approximation $\cos(kd) \approx 1 - \frac{1}{2}k^2 d^2$ and the two roots become:

$$\omega^2 = \frac{\gamma}{2(m + M)} k^2 d^2 \tag{1.6}$$

$$\omega^2 = 2\gamma \left(\frac{1}{m} + \frac{1}{M}\right). \tag{1.7}$$

a)

b)

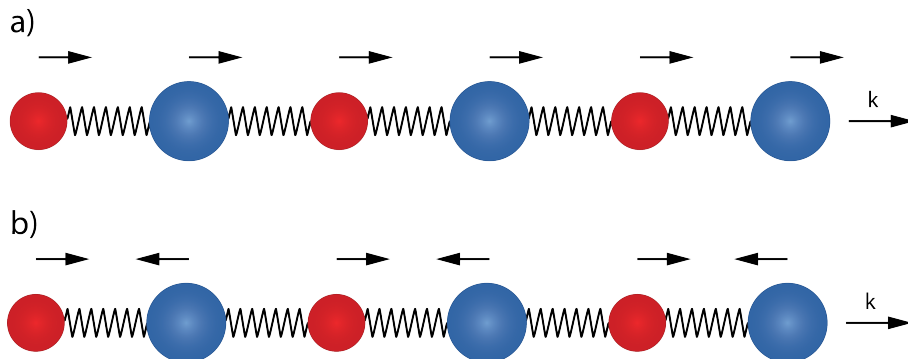Figure 1.2: Schematic representation of the masses movement in (a) *acoustic* and (b) *optical* modes. The masses movement is always the same in all the unit cells. In the acoustic modes the masses within one unit cell move in phase, while in the optical modes they move out of phase.

These two branches of solutions allow to separate the normal modes in two categories, depending on the relative motions of the spheres. In the solutions of equation 1.6, adjacent spheres are moving in the same direction, i.e. in phase, as shown in Fig. 1.2(a). This is easily seen by substituting equation 1.6 into equation 1.3 in the limit of $k = 0$, which leads to $a = b$. In this case the normal modes are at very low frequency, and are called *acoustic*. Equation 1.7 describes solutions in which the spheres are moving in opposite directions, i.e. out of phase [see Fig. 1.2(b)], as can be seen substituting equation 1.7 into equation 1.3 in the limit of $k = 0$, which leads to $a = -\frac{M}{m}b$. Such normal modes are at higher frequencies and are called *optical*. The nomenclature comes from the fact that if the two ions in the unit cell are positively and negatively charged, when they are displaced they create a dipole, and the mode can couple to the electric field of a light wave. These subset of optical phonons are called *infrared active* because their eigenfrequencies span the infrared portion of the electromagnetic spectrum, typically from a few to tens of THz. Since electromagnetic
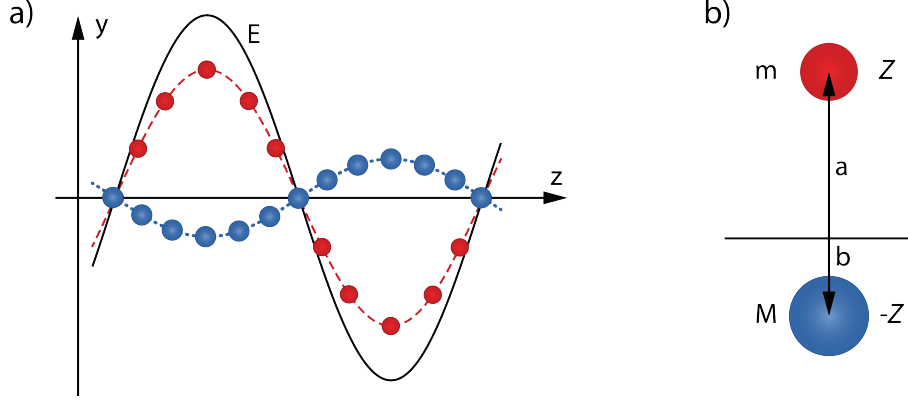
Figure 1.3: (a) Schematic representation of a *transverse optical infrared active* phonon. The wave is propagating in the z direction, while the positive (red) and negative (blue) ions are displaced in the y direction. The black solid line depicts the external electric field E due to the light wave. (b) Displacement of the ions within one unit cell. The positive ions have mass m, charge Z, and are displaced by a vector a, while the negative ions have mass M, charge $-Z$, and are displaced by a vector b.

waves are transverse, they can couple to transverse infrared active modes, in which the displacement of the ions is perpendicular to the propagation direction, as shown in Fig. 1.3(a). This situation can be modeled as shown in Fig. 1.3(b), with ions of mass m and charge Z displaced by a distance a in one direction, and ions of mass M and charge $-Z$ displaced in the opposite direction by a distance b. The equations of motion for the ions can be written (in a similar fashion to Eq. 1.1) as:

$$
\begin{aligned}
m\frac{\partial^2 a}{\partial t^2} &= -\gamma\left(a - b\right) + ZE \\
M\frac{\partial^2 b}{\partial t^2} &= \gamma\left(a - b\right) - ZE,
\end{aligned}
\tag{1.8}
$$

where γ is the spring constant and E the applied electric field. It is convenient to describe the system in terms of a single equation, accounting for the response of the mode as a whole. Defining the effective displacement

W, the effective mass μ and the mode eigenfrequency Ω_{TO} as:

$$W := a - b$$
$$\frac{1}{\mu} := \frac{1}{m} + \frac{1}{M} \tag{1.9}$$
$$\Omega_{TO} := \frac{\gamma}{\mu},$$

equations 1.8 can be rewritten as:

$$\frac{\partial^2 W}{\partial t^2} + \Omega_{TO}^2 W = \frac{Z}{\mu} E. \tag{1.10}$$

This equation describes the motion of an undamped oscillator driven by a force proportional to E. Such oscillator, once set in motion, would perpetually oscillate. This un-physical scenario is due to the *harmonic approximation*, which assumes that the ions are moving in a parabolic potential, i.e. their restoring force is linearly proportional to the displacement.

In real solids, anharmonicities of the lattice potential allow for the energy transfer among different modes and result in a finite lifetime of the phonon oscillations. These effects can be introduced here via a phenomenological damping term, which leads to a new equation of motion of the form

$$\frac{\partial^2 W}{\partial t^2} + \Gamma \frac{\partial W}{\partial t} + \Omega_{TO}^2 W = \frac{Z}{\mu} E, \tag{1.11}$$

where Γ is a coefficient inversely proportional to the lifetime of the phonon mode. This equation successfully describes the interaction of an *infrared active* mode with an external electric field.

1.2   Optical properties of IR-active phonons

The direct interaction of *infrared active* phonons with light is reflected in the optical properties of the solid under consideration. These can be evaluated

by considering the interaction of the phonon with a monochromatic light wave of frequency ω. When dealing with solids, it is common to define a phonon coordinate:

$$Q = \sqrt{N\mu}\,W, \tag{1.12}$$

where N is the number of unit cells per unit volume. This allows to rewrite eq. 1.11 as:

$$\frac{\partial^2 Q}{\partial t^2} + \Gamma \frac{\partial Q}{\partial t} + \Omega_{TO}^2 Q = \sqrt{N/\mu}\,ZE. \tag{1.13}$$

The electromagnetic wave can be written as:

$$E(t) = E_0\left(e^{-i\omega t}\right), \tag{1.14}$$

where the phase term has been incorporated in the complex parameter E_0. For a driving frequency ω, Q takes solutions of the form

$$Q(t) = Q_0\left(e^{-i\omega t}\right), \tag{1.15}$$

where $|Q_0|$ is the amplitude of the phonon oscillations. The phonon response to the field is therefore calculated by substituting Eq. 1.14 and 1.15 in Eq. 1.13:

$$-\omega^2 Q_0 e^{-i\omega t} - i\Gamma\omega Q_0 e^{-i\omega t} + \Omega_{TO}^2 Q_0 e^{-i\omega t} = \sqrt{N/\mu}\,ZE_0 e^{-i\omega t} \tag{1.16}$$

which gives:

$$Q(t) = \frac{\sqrt{N/\mu}\,Z}{\Omega_{TO}^2 - \omega^2 - i\Gamma\omega}E_0 e^{-i\omega t}. \tag{1.17}$$

Equation 1.17 describes the behavior of the phonon oscillator in response to a monochromatic wave. In order to describe the material optical properties, this has to be incorporated into Maxwell's equations, which allow to propagate the effect of the interaction between E and Q in the far field. This is done by taking into account the polarization P, which in a medium

is defined as the dipole moment per unit volume. A single oscillator carries a dipole given by the product between the charge Z and the displacement W, therefore the polarization in the material due to the phonon is:

$$P_{phonon} = NZW = \frac{NZQ}{\sqrt{\mu N}} = \frac{NZ^2}{\mu} \frac{1}{\Omega_{TO}^2 - \omega^2 - i\Gamma\omega} E. \qquad (1.18)$$

The overall polarization in the sample comprises also other contributions, for example due to the electrons which are being polarized by the applied electric field. Since these contributions are not resonant with the phonon, they can be treated as a background polarization proportional to E, $P_\infty = \epsilon_0 \chi E$ where χ is the electric susceptibility. The optical properties of the material are then inserted into Maxwell's equations through the constitutive relation:

$$\vec{D} = \epsilon_0 \vec{E} + \vec{P} = \epsilon_0 \vec{E} + \vec{P}_\infty + \vec{P}_{phonon}. \qquad (1.19)$$

1.2.1   Relative permittivity

It is convenient to incorporate the overall sample response in the relative permittivity ϵ_r, defined such as $\vec{D} = \epsilon_0 \epsilon_r \vec{E}$. This leads to:

$$\epsilon_r(\omega) = 1 + \chi + \frac{NZ^2}{\epsilon_0 \mu} \frac{1}{\Omega_{TO}^2 - \omega^2 - i\Gamma\omega} \qquad (1.20)$$

which can be split into real and imaginary part, so that $\epsilon_r = \epsilon_1 + i\epsilon_2$:

$$\epsilon_1(\omega) = 1 + \chi + \frac{NZ^2}{\epsilon_0 \mu} \frac{\Omega_{TO}^2 - \omega^2}{\left(\Omega_{TO}^2 - \omega^2\right)^2 + (\Gamma\omega)^2}, \qquad (1.21)$$

$$\epsilon_2(\omega) = \frac{NZ^2}{\epsilon_0 \mu} \frac{\Gamma\omega}{\left(\Omega_{TO}^2 - \omega^2\right)^2 + (\Gamma\omega)^2} \qquad (1.22)$$
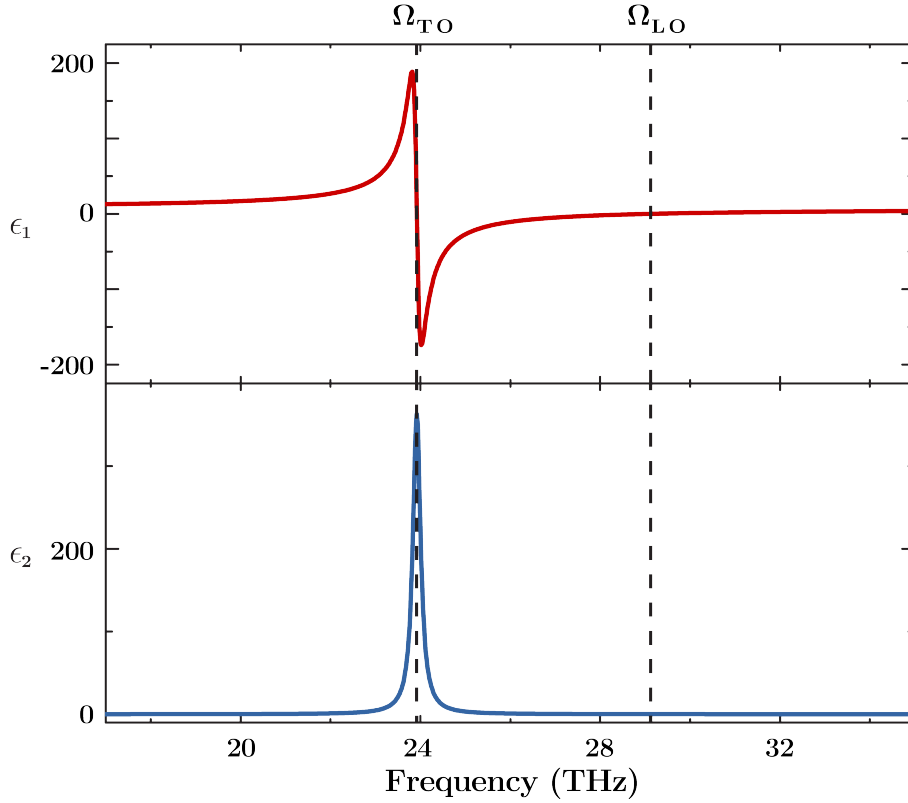
Figure 1.4: Frequency dependent real (ϵ_1) and imaginary (ϵ_2) parts of the relative permittivity. The material parameters used for the plots are those of hexagonal silicon carbide, with $\varepsilon_0 = 9.66$, $\varepsilon_\infty = 6.52$, $\Omega_{TO} = 24.9$ THz and $\Gamma = 0.2$ THz.

which are displayed in Fig. 1.4. It is important to notice that the frequency dependence of the permittivity ϵ_r is all due to the last term of Eq. 1.20, which is ultimately ascribed to the response of the phonon coordinate Q, as can be seen from Eq. 1.17. The real part of the permittivity, starting from a constant value for low frequencies, is strongly reshaped around the resonance, reaching a maximum when approaching Ω_{TO} from low frequencies. This reflects the fact that when the driver approaches the phonon eigen-

frequency, Q starts oscillating closer and closer to its mechanical resonance and therefore its amplitude is increased. Also, as expected from a mechanical oscillator, when driven just above resonance the phonon responds out of phase, resulting in the negative value of ϵ_1 above Ω_{TO}. The real part of ϵ_r then recovers and crosses zero at a characteristic frequency Ω_{LO}, that will be discussed later. In the region between Ω_{TO} and Ω_{LO}, the phonon oscillating out of phase with respect to the impinging electric field is responsible for the screening of the latter, and results in a region in which light cannot propagate into the material. ϵ_2, on the other hand, has a Lorentzian peak at Ω_{TO}, related to the absorption, whose width is given by the damping parameter Γ. In an oscillator without damping ($\Gamma = 0$), ϵ_1 would diverge at Ω_{TO}, and ϵ_2 would be zero at all frequencies. The asymptotic values of ϵ_r can be defined as:

$$
\varepsilon_0 := \epsilon_r(0) = 1 + \chi + \frac{NZ^2}{\epsilon_0 \mu \Omega_{TO}^2}
$$

$$
\varepsilon_\infty := \epsilon_r(\infty) = 1 + \chi
$$

(1.23)

so that the relative permittivity

$$
\epsilon_r(\omega) = \varepsilon_\infty + \frac{\Omega_{TO}^2 (\varepsilon_0 - \varepsilon_\infty)}{\Omega_{TO}^2 - \omega^2 - i\Gamma\omega}
$$

(1.24)

can be described in terms of the experimentally measurable quantities ε_0, ε_∞, Ω_{TO} and Γ. Assuming for simplicity a very small damping (i.e. $\Gamma = 0$), Ω_{LO} can be calculated from from eq. 1.24:

$$
\Omega_{LO}^2 = \frac{\varepsilon_0}{\varepsilon_\infty} \Omega_{TO}^2.
$$

(1.25)

The name Ω_{LO} comes from the electromagnetic theory, and in particular from Maxwell's equation:

$$
\nabla \cdot \vec{D} = 0,
$$

(1.26)

which is valid in absence of free charges. If we consider an electromagnetic wave of the form $\vec{E} = E_0 e^{-i(\vec{k}x - \omega t)}$, Eq. 1.26 implies that $\vec{k} \cdot \epsilon_0 \epsilon_r \vec{E} = 0$. When $\epsilon_r \neq 0$, like in vacuum, this implies that $\vec{k} \cdot \vec{E} = 0$ and therefore electromagnetic waves must be transverse, i.e. the electric field is perpendicular to the propagation direction. If $\epsilon_r = 0$, Maxwell's equations also allow for *longitudinal* solutions, in which the electric field can be parallel to the propagation direction.

1.2.2   Refractive index

The electrical permittivity ϵ encapsulates the phonon coordinate Q dynamics, as discussed in in section 1.2.1. However, the quantities directly measured in experiments are usually the refractive index n, and the absorption coefficient α. These two quantities can be encapsulated in the complex refractive index $\tilde{n} = n + ik$, where $k = \alpha c / 2\omega$, whose real and imaginary parts are plotted in Fig. 1.5. A monochromatic wave of frequency ω and initial amplitude E_0 would propagate in a material with refractive index $\tilde{n}$ according to

$$E(z, t) = E_0 e^{i(\omega \tilde{n} z / c - \omega t)}. \tag{1.27}$$

It is easily shown than the electric field amplitude reduces as $e^{-z\alpha/2}$, and therefore its intensity as $e^{-z\alpha}$, as expected from Beer's law which defines the absorption coefficient. The real part n of the refractive index, which is constant at low frequencies, has a sharp maximum around Ω_{TO}. This reflects the fact that close to resonance the high amplitude of the phonon oscillations make the material optically more dense. In fact the speed of
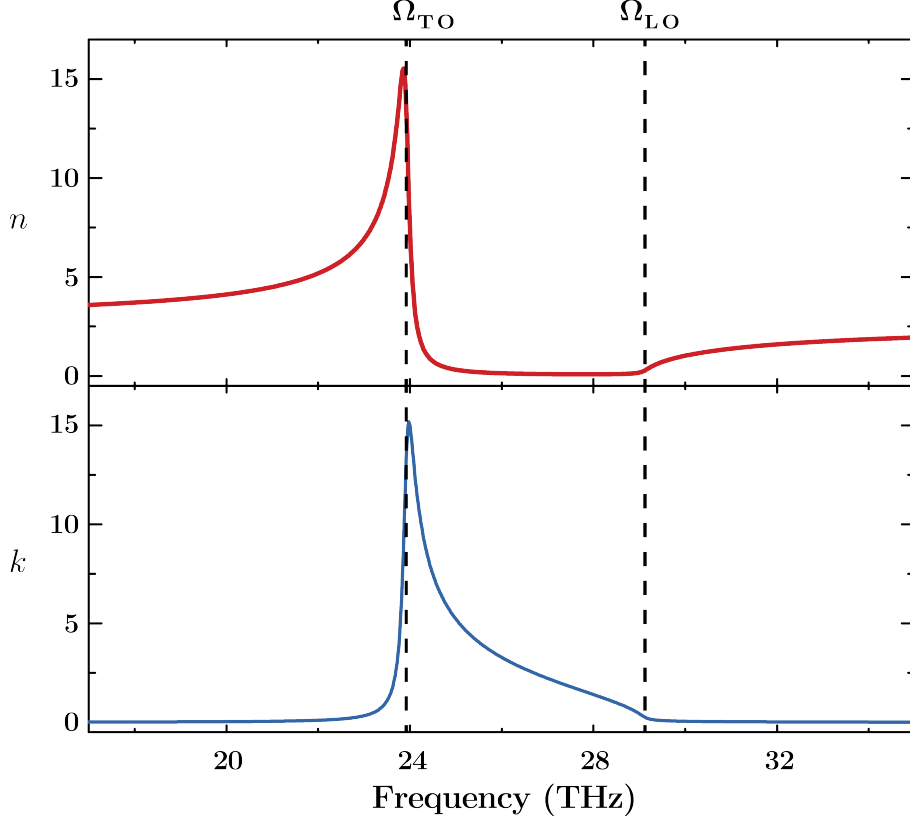
Figure 1.5: Frequency dependent real (n) and imaginary (k) parts of the complex refractive index. The material parameters used for the plots are those of hexagonal silicon carbide, with $\varepsilon_0 = 9.66$, $\varepsilon_\infty = 6.52$, $\Omega_{TO} = 24.9$ THz and $\Gamma = 0.2$ THz.

light in the material, proportional to c/n, is significantly reduced close to Ω_{TO}, as will be discussed in more details in section 1.3. The small value (which would be zero without damping Γ) of n for frequencies between Ω_{TO} and Ω_{LO} is another manifestation of the fact that in such region light cannot propagate in the material. The behavior of k is somehow complementary, being zero for frequencies outside the Ω_{TO} - Ω_{LO} region. In such region, k has a maximum close to Ω_{TO}, where the absorption of light is ascribed to the high amplitude of the phonon coordinate, leading to energy dissipation

towards other phonons through lattice anharmonicities.

The measured complex refractive index can be compared to the permittivity arising from the Lorentz model via the relations:

$$\epsilon_1 = n^2 - k^2 \tag{1.28}$$

$$\epsilon_2 = 2nk. \tag{1.29}$$

1.2.3 Reflectivity

Another relevant optical property of infrared active phonons is the reflectivity, which can also be measured experimentally. The peculiar reflectivity of an infrared active phonon is shown in Fig. 1.6. R, constant at low frequency, is highly enhanced towards Ω_{TO}, where it reaches values close to one, and remains very high up to $\omega \approx \Omega_{LO}$. This high reflectivity region is called *Reststrahlenband*, because the light that cannot enter the material (as already mentioned when discussing ϵ_r and $\tilde{n}$) gets mostly reflected. At a frequency slightly higher than Ω_{LO}, where ϵ_r is crossing one, R drops to zero. This happens because $\epsilon_r = 1$ implies that light can propagate in the material like it was in air, and therefore no light gets reflected at the sample surface.

The reflectivity is related to the refractive index by the relation:

$$R = \left| \frac{1 - \tilde{n}}{1 + \tilde{n}} \right|^2. \tag{1.30}$$

R, unlike $\tilde{n}$ and ϵ_r, is a real rather than complex quantity and therefore does not completely describe the interaction of light with the phonon. The complete information is instead contained in the reflection coefficient r,
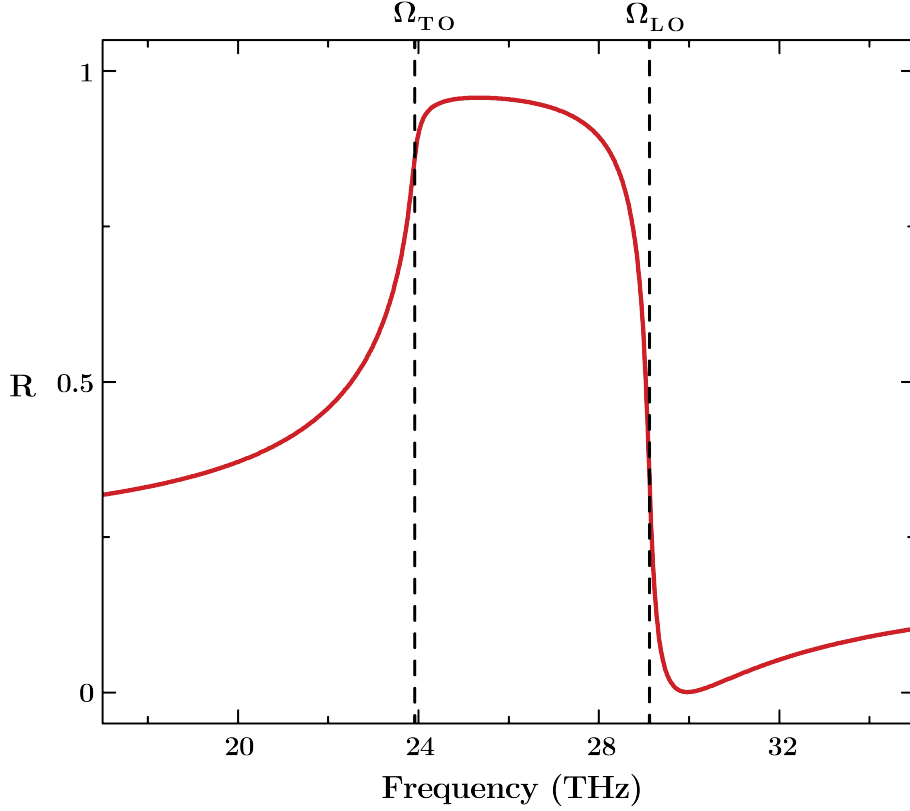
Figure 1.6: Frequency dependent reflectivity. The material parameters used for the plots are those of hexagonal silicon carbide, with $\varepsilon_0 = 9.66$, $\varepsilon_\infty = 6.52$, $\Omega_{TO} = 24.9$ THz and $\Gamma = 0.2$ THz.

which is the ratio between the incoming and reflected electric field. These two quantities are related by

$$R = |r|^2 \tag{1.31}$$

which shows that the phase information is lost when going from r to R. The reflectivity, albeit containing only part of the material properties, is easy to measure, since in most cases the detectors used in the experiments can only measure the light intensity, and not the electric field profile. The full material properties can still be retrieved, in the case of infrared active phonons, by fitting R with the model presented here. All the optical constants ε_0,

Ω_{TO}, and Γ of silicon carbide used throughout this thesis were obtained in this manner, with ϵ_∞ taken from literature data [30, 31].

1.3 Phonon-Polaritons

The optical properties of infrared active phonons introduced in section 1.2 describe the interaction of the lattice with light. In particular, the complex refractive index and the reflectivity allow for retrieving the parameters of a phonon by looking in the far field characteristics of the light reflected by it. All these quantities display peculiar features around Ω_{TO}, and this is due to the fact that at this frequency the light and the phonon are strongly coupled. When this happens, the system cannot be described anymore like a light wave nor like a phonon, and is usually referred to as *phonon-polariton.* In this region, the propagation of light inside the material is strongly affected by the interaction with the lattice, and experiences a very strong dispersion. In order to take a closer look at the behavior of the light propagating inside the material, Maxwell's equations must be taken into account. In a non magnetic material ($\mu_r = 1$) without free charges:

$$
\begin{aligned}
\nabla \cdot \vec{E} &= 0 \\
\nabla \cdot \vec{H} &= 0 \\
\nabla \times \vec{E} &= -\mu_0 \frac{\partial \vec{H}}{\partial t} \\
\nabla \times \vec{H} &= \epsilon_0 \epsilon_r \frac{\partial \vec{E}}{\partial t}.
\end{aligned}
\tag{1.32}
$$

Taking the curl of the third equation and substituting the fourth, together with the identity $\nabla \times \left(\nabla \times \vec{E} \right) = \nabla \left(\nabla \cdot \vec{E} \right) - \nabla^2 \vec{E}$ leads to the wave

equation

$$\nabla^2 \vec{E} = \frac{\epsilon_r}{c^2} \frac{\partial^2 \vec{E}}{\partial t^2} \tag{1.33}$$

where c is the speed of light in vacuum. The deviation of the propagation of light in the material with respect to that in vacuum is encapsulated in ϵ_r. The dispersion of the phonon polariton can therefore be evaluated by inserting the frequency dependent ϵ_r of Eq.1.24 in the dispersion relation $\omega^2 = c^2 k^2 / \epsilon_r$. In the simplified case in which $\Gamma = 0$, this leads to:

$$\varepsilon_\infty + \frac{\Omega_{TO}^2 (\varepsilon_0 - \varepsilon_\infty)}{\Omega_{TO}^2 - \omega^2} = \frac{c^2 k^2}{\omega^2}, \tag{1.34}$$

which is a fourth order equation in ω with solutions of the type;

$$\omega^2 = \frac{\Omega_{TO}^2 \varepsilon_0 + c^2 k^2}{2 \varepsilon_\infty} \pm \frac{1}{\epsilon_\infty} \sqrt{\left(\frac{\Omega_{TO}^2 \varepsilon_0 + c^2 k^2}{2} \right)^2 - c^2 k^2 \Omega_{TO}^2 \varepsilon_\infty}. \tag{1.35}$$

Taking the positive root of ω^2 gives two solutions, known as the upper and lower polariton branches.

The phonon polariton dispersion is shown in Fig. 1.7. The thin purple line represents the dispersion of light in vacuum according to $\omega = ck$, and the thin blue and red lines depict the dispersion of light in the material far away from the resonance at low and high frequency, respectively. Without resonance, ε_∞ would be equal to ε_0, and the light would be propagating at a speed $c/\sqrt{\varepsilon_0}$. The phonon resonance is depicted in Fig. 1.7 by the dashed line, and it has no dispersion, i.e. can be represented by a horizontal line, because the plot is only depicting a very small fraction of the Brillouin zone. This is consistent with equation 1.7 which shows that, for an optical mode in the limit of $k = 0$ where the light momentum is comparable with that of the phonon, the latter has no dispersion.The phonon-polariton dispersion then
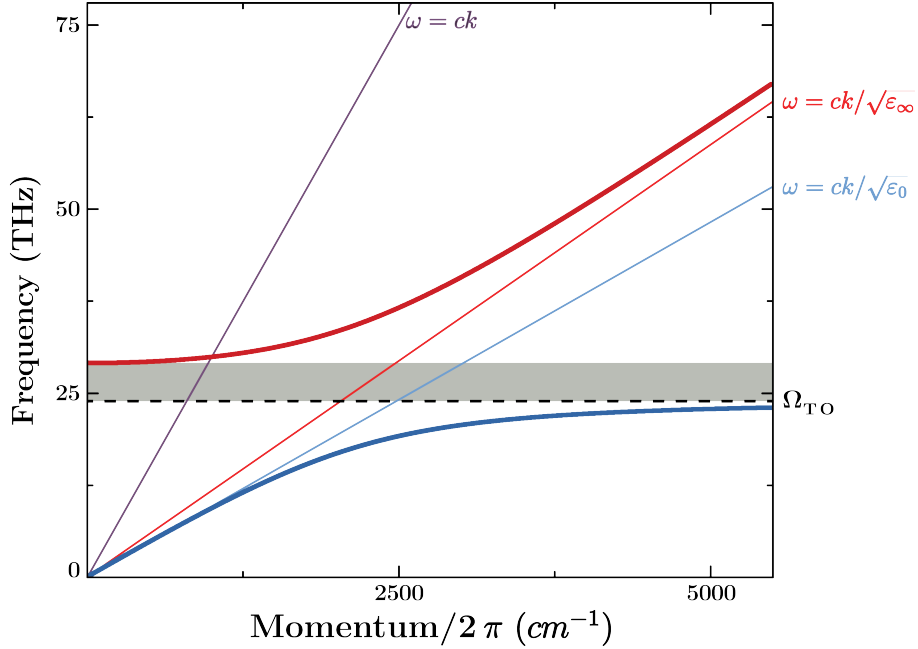
Figure 1.7: Dispersion of the upper (thick red line) and lower (thick blue line) polariton branches. The dashed line represents the optical phonon, which close to $k = 0$ does not disperse. The grey shaded area is the reststrahlenband, in which light cannot propagate. The thin red and blue lines represent the dispersion of light in the solid far away from the resonance at high and low frequencies, respectively. The purple line is the dispersion of light in vacuum.

arises from an avoided crossing between the phonon line and the thin blue photon line. The phonon-polariton displays different behaviors in different regions of the dispersion map. The lower branch, for example, has a *photon-like* behavior at low frequencies, while it behaves in a *phonon-like* fashion, with a very small velocity, when approaching Ω_{TO}. The upper branch, on the other hand, starts from a *phonon-like* behavior in its lowest frequency region, i.e. just above Ω_{LO}, and then has a *photon-like* character at high frequencies. The *reststrahlen band* region between Ω_{TO} and Ω_{LO} shown by the grey shading in Fig. 1.7 is effectively a bandgap, and arises from

the aforementioned avoided crossing. This corresponds to the frequency region in which ϵ_1 is negative, and the real part n of the refractive index is zero. Even if it is called Ω_{LO}, the upper limit of the reststrahlen band does not correspond to a longitudinal mode to which the light is coupling to. As a matter of fact light, propagating in air as a transverse wave, cannot couple to longitudinal modes in a bulk crystal (note that in Fig. 1.7 no line is displayed at Ω_{LO}). An important feature of the phonon-polariton dispersion relations is the fact that at frequencies close to the reststrahlen band, where the behavior is *phonon-like*, the group velocity $v_g = \partial\omega/\partial k$ is very small. This implies that at those frequencies polaritons can propagate in the material, but very slowly. These aspect has to be taken into account when the optical properties are measured in the time domain, like in the experiments described in this thesis. The electric field reflected from the material at these frequencies it is going to be detected at later times compared to that reflected in reststrahlen band.

1.4 Energy density functional description

The linear optical properties of infrared active phonons are usually derived from the Lorentz model, as previously discussed. This starts from the modeling of phonons as charged harmonic oscillators, and allows to calculate the permittivity ϵ_r starting from their equation of motion, in a *bottom-up* approach. A more formal *top-down* approach, based on a phenomenological energy density functional, is useful to describe the light-phonons interaction in a way easier to extend to the nonlinear regime which will be discussed later in this thesis [32, 33]. Such energy density functional can be written as:

$$L = \frac{1}{2}\Omega_{TO}^2 Q^2 - \frac{1}{2}\epsilon_0 \left(\varepsilon_\infty - 1\right) E^2 - \Omega_{TO}\sqrt{\epsilon_0 \left(\varepsilon_0 - \varepsilon_\infty\right)}QE. \qquad (1.36)$$

In this equation, the first term is the energy of the mechanical oscillator with eigenfrequency Ω_{TO} and normalized coordinate Q. The second term accounts for the energy of the electric field in the solid at frequencies far away from the oscillator eigenfrequency. This can be easily shown recalling that from eq. 1.23 follows $\varepsilon_\infty - 1 = \chi$, which is the susceptibility leading to the background polarization introduced in section 1.2. Finally, the third term in eq. 1.36 is taking into account the linear interaction between the oscillator Q and the electric field E.

From this energy density functional it is possible to retrieve the force acting on the mechanical oscillator:

$$F_Q = -\frac{\partial L}{\partial Q} = -\Omega_{TO}^2 Q + \Omega_{TO}\sqrt{\epsilon_0 \left(\varepsilon_0 - \varepsilon_\infty\right)}E. \qquad (1.37)$$

Combining the definitions of ε_0 and ε_∞ from eq. 1.23 it is possible to write:

$$\Omega_{TO}^2 \epsilon_0 \left(\varepsilon_0 - \varepsilon_\infty\right) = \frac{NZ^2}{\mu} \qquad (1.38)$$

and substituting into 1.37 leads to:

$$F_Q = -\Omega_{TO}^2 Q + \sqrt{N/\mu}ZE, \qquad (1.39)$$

which is equivalent to Eq. 1.13 derived in section 1.2 for the case of an undamped oscillator.

The polarization P can also be derived from the energy density functional via the relation:

$$P = -\frac{\partial L}{\partial E} = \epsilon_0 \left(\varepsilon_\infty - 1\right) E + \Omega_{TO}\sqrt{\epsilon_0 \left(\varepsilon_0 - \varepsilon_\infty\right)}Q. \qquad (1.40)$$

The first term in this equations gives a polarization equivalent to $P = \epsilon_0 \chi E$, which in section 1.2 was referred to as P_∞. The second term in eq. 1.40 leads, substituting eq. 1.38, to:

$$P = \sqrt{N/\mu} ZQ = \sqrt{N/\mu} \sqrt{N\mu} WZ = NZW, \qquad (1.41)$$

which is equivalent to P_{phonon} introduced in section 1.2.

Chapter 2

Phonon nonlinearities and amplification

The focus of this thesis is the investigation of the phonon response to very intense laser pulses, capable of displacing the ions by up to a few percent of the equilibrium interatomic distances. Under these circumstances, the lattice response is expected to exhibit a nonlinear behavior that the Lorentz model fails to describe. Therefore, an expansion of such model capable of describing the nonlinear optical properties of an infrared active mode is presented.

First principle DFT calculations are used to explore the nonlinear response of the lattice to very large applied static electric fields and consequently large ionic displacements.

These results are then incorporated in a model describing the dynamic response of the phonon to electric fields oscillating at frequencies close to its resonance and showing that a parametric amplification of the phonon coordinate oscillation is expected.

2.1   Nonlinear expansion of the polarization

The polarization induced in a material by an applied electric field entails two contributions, namely the resonant contribution P_{phonon} due to the displacement of the charged ions and the background contribution P_∞ ascribed to the screening of other phonons and electrons. When the electric fields interacting with the solid are very intense and ions displacement Q becomes large, the polarization becomes non-linear, and both these polarization terms have to be expanded.
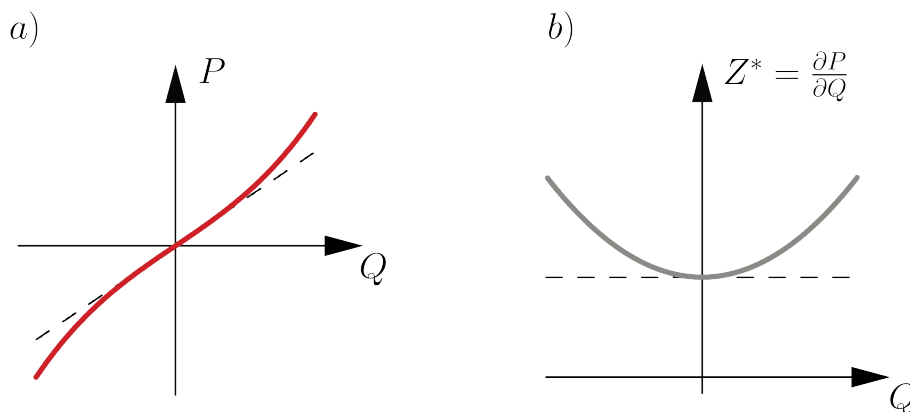
Figure 2.1:   (a) Resonant phonon contribution to the polarization, P_{phonon}. For small phonon coordinate displacements, the polarization is linear in Q, and the Born effective charge $Z^* = \partial P / \partial Q$ (b) is constant. When the displacement increases, the polarization deviates from linear, with a consequent increase of Z^*. It is important to note that the Born effective charge increase is quadratic in Q, i.e. it is independent on the direction of the phonon coordinate displacement.

The first contribution to the nonlinear polarization, P_{phonon}, is proportional to the mode coordinate Q through the effective dipolar charge Z^* that embodies the oscillator strength of the phonon. Such Born effective charge is defined as $Z^* = \partial P_{phonon} / \partial Q$ and is a constant for small values of Q,

where the polarization P_{phonon} is linear in the phonon coordinate, as shown in Fig. 2.1. In this case:

$$P_{phonon} = Z^* Q, \tag{2.1}$$

which is equivalent to eq. 1.41, where the charge Z of the Lorentz model has been re-normalized to account for the mode effective mass μ and the number of oscillators per unit volume N, leading to the Born-effective-charge $Z^* = \sqrt{(N/\mu)}\, Z$. For very high driving electric fields, P_{phonon} depends nonlinearly on the lattice displacement Q, as calculated from first principles DFT calculations and shown in Fig. 2.1a. Correspondingly, the Born effective charge becomes a function of Q as shown in Fig. 2.1b. For SiC Z^* depends quadratically on the lattice coordinate Q as

$$Z^* = \frac{\partial P}{\partial Q} = Z_0^* + \alpha Q^2. \tag{2.2}$$

Importantly, the sign of the change in Z^* does not depend on the direction of the phonon displacement Q. Hence, an oscillating lattice mode will result in a net average change of the Born effective charge.

The second contribution to the polarization, P_∞, is in linear response described by:

$$P_\infty = \epsilon_0 \chi E = \epsilon_0 \left(\varepsilon_\infty - 1 \right) E, \tag{2.3}$$

as detailed in chapter 1. Similarly to the Born effective charge Z^*, the permittivity ε_∞ is constant only for small lattice displacements Q, while it increases for large amplitudes. This effect is captured by Fig. 2.2a, in which the slope $\chi = \varepsilon_\infty - 1$ of P_∞, calculated from DFT, increases with the lattice displacement Q. Just like the Born effective charge, ϵ_∞ scales quadratically with Q:
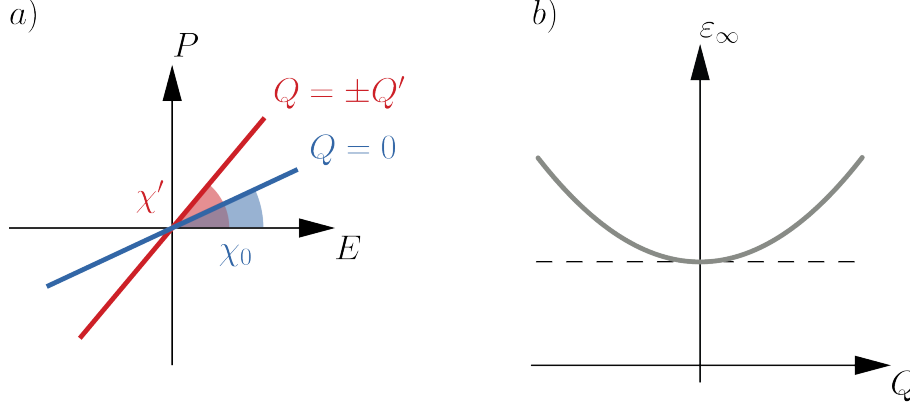
Figure 2.2: (a) Non-resonant contribution $P_\infty = \epsilon_0 \chi E$ to the polarization for different lattice displacements. The susceptibility χ increases as the displacement Q becomes larger. (b) Dependence of the non-resonant permittivity ε_∞ on the phonon coordinate Q.

$$\varepsilon_\infty = 1 + \chi = 1 + \frac{\partial P_\infty}{\partial E} = \varepsilon_{\infty,0} + 2\beta Q^2, \tag{2.4}$$

where the pre-factor 2 descends from a formal derivation of the polarization from the energy density functional that will be described in section 2.3. The correction to the permittivity for large values of the phonon coordinate is sketched in Fig. 2.2b, hence oscillations of Q result in a net average increase of ε_∞.

Summarizing, the nonlinear polarization of a strongly driven normal mode includes two corrections quadratic in Q, one to the phonon effective dipolar charge Z^* and one to the dielectric constant ε_∞. The overall nonlinear polarization can be written as:

$$P = P_{phonon} + P_\infty = \left(Z_0^* + \alpha Q^2\right) Q + \epsilon_0 \left(\varepsilon_{\infty,0} + 2\beta Q^2 - 1\right) E. \tag{2.5}$$

These two terms are typically neglected in the linear lattice response but must be included when studying the dynamics of an infrared active mode subject to a strong resonant optical field $E_0 \sin(\omega t)$.

2.2   Nonlinear equation of motion

The Q-dependent Z^* and ε_∞ do not only affect the polarization in the material, but also the phonon coordinate Q equation of motion. For small driving electric fields, the time dependent phonon coordinate $Q(t)$ follows the equation of motion of a periodically-driven damped harmonic oscillator

$$\frac{\partial^2 Q}{\partial t^2} + \Gamma \frac{\partial Q}{\partial t} + \Omega_{TO}^2 Q = Z^* E_0 \sin(\omega t), \qquad (2.6)$$

where $Z^* = Z_0^*$ and $\varepsilon_\infty = \varepsilon_{\infty,0}$. The familiar linear response solution to this equation is $Q = Q_0 \sin(\omega t) e^{-\Gamma t}$.

The modifications to the ionic motions arising from the modulations of the Born effective charge and the dielectric constant are conveniently discussed by considering the effect of the two effects independently.

The nonlinear response of P_{phonon} alone ($\alpha \neq 0, \beta = 0$), will be discussed first. In this case, the equation of motion becomes:

$$\frac{\partial^2 Q}{\partial t^2} + \Gamma \frac{\partial Q}{\partial t} + \Omega_{TO}^2 Q = \left[Z_0^* + 3\alpha Q^2 \right] E_0 \sin(\omega t), \qquad (2.7)$$

where the pre-factor 3 descends from a formal derivation of the equation of motion from the energy density functional that will be discussed in section 2.3. Qualitatively, this can be thought of as a correction to the force term in the equation of motion. For a driving electric field at frequency ω, the phonon coordinate oscillates as $Q_0 \sin(\omega t)$, and the force term is modulated as

$$3\alpha Q^2 = 3\alpha Q_0^2 \left(\frac{1}{2} - \frac{1}{2} \cos(2\omega t) \right) \qquad (2.8)$$

acquiring a positive offset and more importantly oscillating at frequency 2ω, as sketched in FIg. 2.3. The driver on the right hand side of eq. 2.7 then
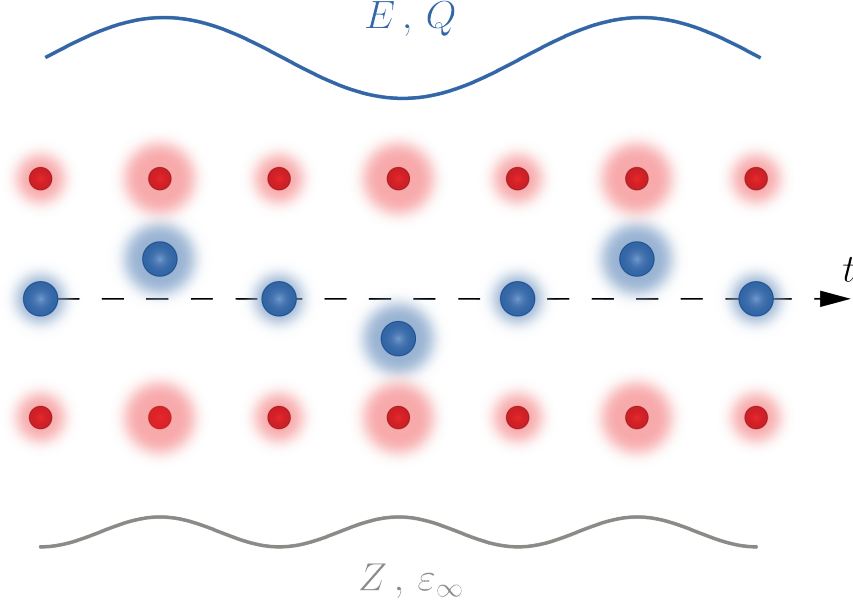
Figure 2.3: Dynamical response of a chain of Silicon (blue) and Carbon (red) atoms to a strong periodic electric field driver $E = E_0 \sin(\omega t)$. The phonon coordinate Q is also oscillating at frequency ω (blue line). The Born effective charge, sketched as a shaded area around the ions, is oscillating at frequency 2ω, as well as the non-resonant permittivity ε_∞ (grey line).

becomes

$$\left(Z_0^* + \frac{3}{2}\alpha\, Q_0^2\right) E_0 \sin(\omega t) - \frac{3}{2}\alpha\, Q_0^2 E_0 \sin(\omega t)\cos(2\omega t),\qquad(2.9)$$

which can be simplified to

$$\left(Z_0^* + \frac{3}{4}\alpha\, Q_0^2\right) E_0 \sin(\omega t) - \frac{3}{4}\alpha\, Q_0^2 E_0 \sin(3\omega t).\qquad(2.10)$$

This equation shows that to leading order the modulation of the Born effective charge adds a 3ω component to the oscillator driver. Adding higher order terms on the right hand side of the oscillator equation is a process analogous that used to describe optical nonlinearities in dispersive materials

[2]. Thus, equation 2.7 is expected to support amplification of the phonon coordinate Q based on the Born effective charge modulation.

Next, the influence of the ϵ_∞ modulation on the ionic motion is discusses. As shown in eq. 2.5, P_∞ is increased by a factor $2\epsilon_0\beta Q^2 E$, which results in a correction to the energy of the system as

$$\Delta L = -\int P\, dE \propto -\beta Q^2 E^2. \tag{2.11}$$

This energy term leads to an additional force on the oscillator

$$\Delta F_q = -\frac{\partial \Delta L}{\partial Q} \propto +2\beta Q E^2, \tag{2.12}$$

and the equation of motion 2.6 becomes

$$\frac{\partial^2 Q}{\partial t^2} + \Gamma\frac{\partial Q}{\partial t} + \Omega_{TO}^2 Q = Z^* E_0 \sin\left(\omega t\right) + 2\beta Q E^2, \tag{2.13}$$

which is conveniently rewritten as

$$\frac{\partial^2 Q}{\partial t^2} + \Gamma\frac{\partial Q}{\partial t} + \left[\Omega_{TO}^2 - 2\beta E^2\right] Q = Z^* E_0 \sin\left(\omega t\right). \tag{2.14}$$

Clearly, the modulation of the dielectric function is qualitatively reflected into a modulation of the oscillator eigenfrequency $\Omega_{TO} = \Omega_{TO,0} - 2\beta E^2$. With $E = E_0 \sin\left(\omega t\right)$, the modulation of Ω_{TO} can be written as

$$2\beta E^2 = 2\beta E_0^2 \left(\frac{1}{2} - \frac{1}{2}\cos\left(2\omega t\right)\right) \tag{2.15}$$

and the oscillator frequency renormalizes to

$$\Omega_{TO}^2(t) = \Omega_{TO,0}^2 \left(1 - \frac{\beta E_0^2}{\Omega_{TO,0}^2} + \frac{\beta E_0^2}{\Omega_{TO,0}^2}\cos\left(2\omega t\right)\right) \tag{2.16}$$

i.e. acquires a negative offset and oscillates at frequency 2ω. The equation of motion becomes

$$\frac{\partial^2 Q}{\partial t^2} + \Gamma \frac{\partial Q}{\partial t} + \Omega_{TO}^2(t) Q = Z^* E_0 \sin(\omega t), \qquad\qquad (2.17)$$

which is that of a forced parametric oscillator, expected to support parametric amplification of the phonon coordinate Q. It should also be noted that the 2ω oscillation of Ω_{TO}^2 makes this equation very similar to a Mathieu equation $\frac{\partial^2 y}{\partial x^2} + (a - 2q\cos(2x)) y = 0$ which is routinely used to describe the parametric resonance problems, reinforcing the expectation of phonon amplification.

In a situation where both the Born effective charge and the permittivity are modulated (i.e. $\alpha \neq 0$ and $\beta \neq 0$), the ionic motions are governed by

$$\frac{\partial^2 Q}{\partial t^2} + \Gamma \frac{\partial Q}{\partial t} + \left[\Omega_{TO}^2 - 2\beta E^2\right] Q = \left[Z_0^* + 3\alpha Q^2\right] E_0 \sin(\omega t). \qquad (2.18)$$

In this case, the oscillator frequency is modulated at frequency 2ω and the driver on the right hand side of the equation is simultaneously acquiring a 3ω component. The net effect on the phonon dynamics depends on the relative strengths and the interplay between the modulations of Z^* and ϵ_∞. However, net parametric amplification of the phonon coordinate Q can be expected in any case, and this prediction will be tested in the present thesis by performing experiments on the prototypical dielectric SiC.

2.3   Energy density functional description

In the following, the nonlinear optical properties of an infrared active phonon will be described with a more formal approach, starting from an expansion of the phenomenological energy density functional introduced in section 1.4. This approach allows for a consistent derivation of the nonlinear polarization and the nonlinear equation of motion.

According to eq. 1.36, the linear energy functional reads:

$$L = \frac{1}{2}\Omega_{TO}^2 Q^2 - \frac{1}{2}\epsilon_0 \left(\varepsilon_\infty - 1\right) E^2 - \Omega_{TO}\sqrt{\epsilon_0 \left(\varepsilon_0 - \varepsilon_\infty\right)}QE. \qquad (2.19)$$

For intense light fields, driving the phonon coordinate to large amplitude, this energy functional needs to be expanded to higher orders in both Q and E.

The first expansion order of eq. 2.19 includes $Q^2 E$ and QE^2 terms, which are symmetry-forbidden for the Si-C stretching mode of 4H-SiC studied here. The first relevant expansion is of the fourth order, leading to an energy functional of the form:

$$\begin{aligned} L = &\frac{1}{2}\Omega_{TO}^2 Q^2 - \frac{1}{2}\epsilon_0 \left(\varepsilon_\infty - 1\right) E^2 - \Omega_{TO}\sqrt{\epsilon_0 \left(\varepsilon_0 - \varepsilon_\infty\right)}QE \\ &- \alpha Q^3 E - \beta Q^2 E^2 - \theta QE^3 - \xi E^4 - \phi Q^4, \end{aligned} \qquad (2.20)$$

where expansion coefficients α, β, θ, ξ and ϕ. Equation 2.20 can be rearranged to express the various nonlinear expansion terms as a correction to the coefficients in Eq. 2.19, leading to:

$$\begin{aligned} L = &\left[\frac{1}{2}\Omega_{TO}^2 + \phi Q^2\right] Q^2 - \left[\frac{1}{2}\epsilon_0 \left(\varepsilon_\infty - 1\right) + \beta Q^2 + \xi E^2\right] E^2 \\ &- \left[\Omega_{TO}\sqrt{\epsilon_0 \left(\varepsilon_0 - \varepsilon_\infty\right)} + \alpha Q^2 + \theta E^2\right] QE. \end{aligned} \qquad (2.21)$$

The ϕ, β and α terms can be seen as Q^2-modulations of the linear interaction terms, namely the oscillator frequency Ω_{TO}^2, the non-resonant contribution to the permittivity ε_∞ and the Born effective charge $Z^* = \Omega_{TO}\sqrt{\epsilon_0 \left(\varepsilon_0 - \varepsilon_\infty\right)}$, respectively. The ξ and θ terms, on the other hand, can be seen as E^2-modulations of ε_∞ and Z^*, respectively.

Coefficient	Variable	Value	Energy %
Ω_{TO}	Q^2	23 THz	92.6
ε_∞	E^2	5.91	0.2
Z^*	QE	$2.61e$	6.7
α	Q^3E	$3.00 \times 10^5 \, eV/(u^{3/2}\sqrt{\mathring{A}} \, MV)$	0.4
β	Q^2E^2	$1.75 \times 10^{11} \, eV/(u \, MV^2)$	0.1
θ	QE^3	$6.24 \times 10^{14} \, eV\sqrt{(\mathring{A})}/(MV^3\sqrt{u})$	$\ll 0.1$
ξ	E^4	$3.26 \times 10^{13} \, cm \, eV/MV^4$	$\ll 0.1$
ϕ	Q^4	$1.20 \times 10^{-3} \, eV/(u^2\mathring{A})$	$\ll 0.1$

Table 2.1: Values of the coefficients used to fit with Eq. 2.20 the energy landscape resulting from DFT calculations . The relative energy contributions are shown in the last column.

The relative strengths of the various expansion terms was evaluated from first principles density functional theory (DFT) calculations of the total energy density of 4H-SiC as a function of the phonon displacement Q and applied static electric field E. The two-dimensional energy landscape obtained from DFT was then fitted with eq. 2.20, allowing to estimate the value of the expansion coefficients, shown in Tab. 2.1. The contribution to the energy density for each of the expansion terms can also be extracted from the DFT calculations, and is reported in Tab. 2.1. These relative contributions were calculated for a 10 MV/cm driving field (on the order of those used in the experiments described in this work), and show that the α and β terms dominate the expansion. The nonlinear energy density functional, considering only these two terms reads

$$L = \frac{1}{2}\Omega_{TO}^2 Q^2 - \left[\frac{1}{2}\epsilon_0\left(\varepsilon_\infty - 1\right) + \beta Q^2\right] E^2$$
$$- \left[\Omega_{TO}\sqrt{\epsilon_0\left(\varepsilon_0 - \varepsilon_\infty\right)} + \alpha Q^2\right] QE, \tag{2.22}$$

from which the nonlinear polarization

$$P = -\frac{\partial L}{\partial E} = \epsilon_0\left(\varepsilon_\infty - 1\right)E + \Omega_{TO}\sqrt{\epsilon_0\left(\varepsilon_0 - \varepsilon_\infty\right)}Q + \alpha Q^3 + 2\beta Q^2 E, \tag{2.23}$$

can be rearranged like

$$P = \epsilon_0\left(\left[\varepsilon_\infty + 2\beta Q^2\right] - 1\right)E + \left[\Omega_{TO}\sqrt{\epsilon_0\left(\varepsilon_0 - \varepsilon_\infty\right)} + \alpha Q^2\right]Q. \tag{2.24}$$

The nonlinear force acting on the phonon coordinate on the other end reads

$$F_Q = -\frac{\partial L}{\partial Q} = -\Omega_{TO}^2 Q + \Omega_{TO}\sqrt{\epsilon_0\left(\varepsilon_0 - \varepsilon_\infty\right)}E + 3\alpha Q^2 E + 2\beta Q E^2, \tag{2.25}$$

leading to the equation of motion

$$\frac{\partial^2 Q}{\partial t^2} + \Gamma\frac{\partial Q}{\partial t} + \left[\Omega_{TO}^2 - 2\beta E^2\right]Q = \left[Z_0^* + 3\alpha Q^2\right]E_0\sin\left(\omega t\right). \tag{2.26}$$

The nonlinear equations 2.23 and 2.26 formally calculated from the non-linear energy density functional are equivalent to equations 2.5 and 2.18 introduced earlier.

Chapter 3

Time resolved SiC reflectivity measurements

Driven to very large amplitudes, the infrared active mode of a dielectric material is expected to induce a parametric amplification of the phonon coordinate oscillations. This theoretical prediction based on first principles DFT calculations is experimentally validated here in silicon carbide. This material was chosen because it exhibits a single infrared active mode in the mid-infrared, and hence can be modeled with a single Lorentz oscillator. Its response to very large excitations can be evaluated in the framework of the model presented in chapter 2.

The phonon response was investigated in this thesis by measuring the time-dependent change of the amplitude and phase of weak probe pulses reflected from the sample after intense mid-infrared excitation. Because the Si-C stretching mode reflectivity features lay in the range between 22 and 33 THz, this probing technique usually employed in the few-THz portion of the electromagnetic spectrum was extended here to the mid-infrared.

3.1   Silicon Carbide

Silicon carbide (SiC) is a wide band gap indirect semiconductor, with interesting electronic properties for high-power electronic devices. It exhibits high electron mobility, high breakdown field and high thermal conductivity. For this reason SiC has been studied since the end of the 19th century. For example, the phenomenon of electroluminescence was discovered for the first time in SiC in 1907 [34], and the first commercial LEDs in the 1970s were also based on SiC. More recently, SiC became popular again as a substrate for the epitaxial grow of graphene [35]. In the present thesis, SiC was chosen because of its textbook-like optical properties in the mid infrared spectral region, making it ideal to study the phononic response of a dielectric to intense resonant light pulses.

3.1.1   Crystal structure and optical properties of SiC

Silicon carbide has a strong covalent bonding between the Si and C atoms, and the basic arrangement of atoms in the crystal is a tetrahedron with a Si (C) atom in the middle of four C (Si) atoms, with a Si-C distance of 1.89 $\mathring{A}$, and a Si-Si (C-C) distance of 3.08 $\mathring{A}$.

The crystal basis is a pair of Si and C atoms displaced along the c axis, and such bases are arranged on the ab plane forming a honeycomb structure, as shown by the red circles in Fig. 3.1a (labeled with the letter A). The tetrahedra are then formed by stacking these bilayers of Si and C along the c axis. Because of the honeycomb arrangement of the Si-C basis within each bilayer, the adjacent bilayers can be stacked in two different ways, as shown by the black squares and green triangles in Fig. 3.1a, labelled with the letters B and C, respectively. For this reason, SiC can crystallize
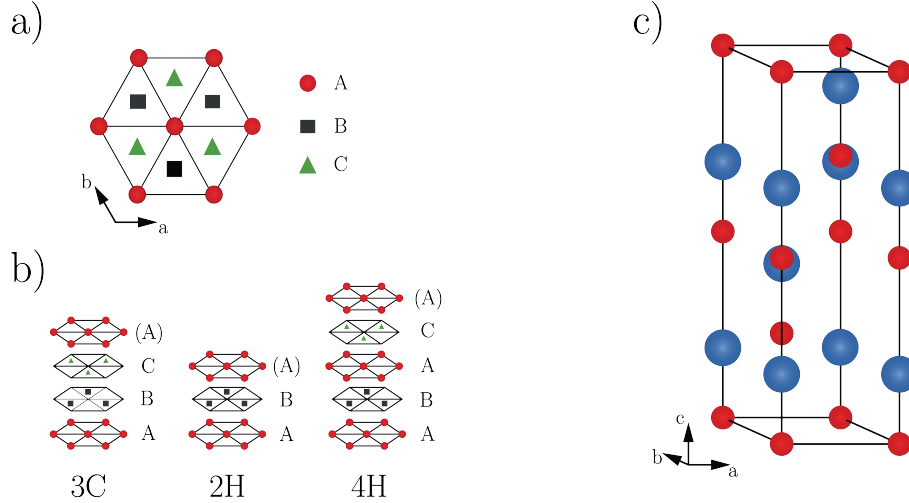
Figure 3.1: a) Red: hexagonal real space distribution of the Si-C bases in one bilayer of SiC. The Si and C atoms in the bases are stacked on the c axis, and the honeycomb distribution of such bases in on the a-b plabe. Black and green: different possibilities for the stacking of the Si-C basis in the adjacent layers. b) Unit cells of some SiC polytypes. The layers are stacked along the c axis in different orders. c) Unit cell of 4H-SiC. Carbon and silicon atoms are depicted in blue and red, respectively.

in different configurations, called polytypes [1]. The polytypes of SiC are more than 200, and exhibit cubic, hexagonal and rhombohedral structures, depending on the layers stacking scheme. An example of the different layer arrangements is shown in Fig. 3.1b, giving rise to some of the most common SiC polytypes. 3C-SiC is cubic, and results from an ABC(A) stacking of the planes. Polytype 2H, instead, is hexagonal, and results from layers ordered in AB(A) sequence. The sample studied here was 4H-SiC, also hexagonal, with layers stacked in ABAC(A) sequence, and whose unit cell is shown in

---

[1]Materials crystallizing in different forms are usually referred to as polymorphs. For SiC, because of the particular two-dimensional nature of the polymorphism, the different compounds are called polytypes.

Fig. 3.1c (space group $C_{6\nu}^4$-$P6_{3mc}$). The 4H nomenclature comes from the fact that the unit cell is made of 4 Si-C bilayers, and that the crystal is hexagonal.
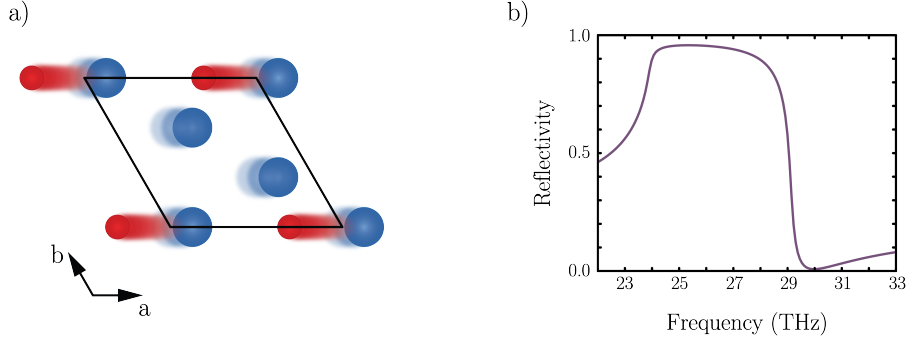
Figure 3.2: a) Displacement from their equilibrium position of the Carbon (blue) and Silicon (red) atoms in the 24 THz infrared active mode of 4H-SiC. The two species move in opposite directions along one of the in-plane crystallographic axes. b) Frequency dependent reflectivity ascribed to the mode of panel a.

The Si-C stretching vibrational mode studied in this thesis is displayed in Fig. 3.2a, with the carbon (blue) and silicon (red) atoms moving in opposite directions along one of the in-plane crystallographic axes. The fingerprint of this infrared-active mode in the optical reflectivity is shown in Fig. 3.2b, with a very wide reststrahlenband extending from Ω_{TO} = 24 THz to Ω_{LO} = 29 THz. Such reflectivity makes SiC ideal to study the response of the phonon mode when driven to very large amplitude oscillations. First of all, the absence of other infrared active phonons in the same frequency range makes it possible to model the system with a single Lorentz oscillator, and its nonlinear response can be modeled with the modulation of the Born effective charge and high frequency permittivity presented in this thesis. Additionally, the frequency range of interest, extending from 22 to 33 THz, is covered by current femtosecond mid-infrared pulses generation techniques,

allowing to investigate the phonon response using time domain spectroscopy.

3.2 Nonlinear spectroscopy in the mid-infrared

The mid-infrared (MIR) portion of the electromagnetic spectrum, extending from a few to some tens of microns wavelengths, allows to investigate the vibrational degrees of freedom of molecular and solid state materials. In particular phonons, which are tied to functionally relevant electronic and magnetic properties of condensed matter, can be investigated by optical spectroscopy in the MIR. Traditionally, this spectral region has been investigated with Fourier transform infrared (FTIR) spectroscopy, which allows to measure the materials linear optical properties in a broad frequency range. These measurements are usually performed with commercial spectrometers, employing different incoherent light sources covering different portion of the spectrum. This technique allows to measure for example the reflectivity R, and the retrieval of the complex optical properties such as the dielectric function or the refractive index is indirect, as it relies on Kramers-Kronig transformations.

The development of THz optical technologies over the last decades opened up the path to time-domain spectroscopy. This technique is based on the generation of carrier-envelope-phase (CEP) stable THz pulses which are then characterized using optical gating. This allows for the measurement of their electric field profiles in the time domain. Because these entail both amplitude and phase information, the complex optical properties are readily obtained without employing Kramers-Kronig transformations.

Time-domain spectroscopy started in the low THz portion of the electromagentic spectrum (THz-TDS, ranging from 0.1 to 2-3 THz), where CEP

stable pulses are easier to achieve. In such spectral region, photoconductive antennae are viable sources, and nonlinear optical crystals can be used both for the pulses generation as well as for free-space electro-optical sampling (EOS) detection. Because these generation processes are all based on optical rectification (OR), the THz CEP stability is granted independently on that of the generating pulses. The main requirement for the implementation of THz-TDS are laser pulses short enough to support the desired THz bandwidth and to optically gate the electric fields transients. Typically this is achieved by sub-100 fs laser pulses, which are nowadays easily obtained by commercial laser systems.

More recently, more complex techniques for the generation of CEP stable pulses arising from generation processes other than OR have been developed. For example, CEP stable pulses in the MIR can be generated exploiting optical parametric amplification (OPA) and difference frequency generation (DFG) processes. These allow to generate pulses in the 7 to 80 μm wavelength range, paving the way for an increase of the TDS frequency reach.

The advantages of TDS over traditional FTIR spectroscopy are not limited to the direct reconstruction of the complex optical properties. In the context of this thesis, a far more important aspect is the pulsed nature of the employed electric field profiles, which makes this technique suitable for the materials nonlinear optical properties investigation. Combining the THz/MIR pulses used in TDS with an additional pump pulse, it is possible to determine the induced changes to the optical properties. This powerful technique is called time-resolved TDS (TR-TDS) as it allows track the evolution of the optical properties as a function of time after photoexcitation.

In this thesis, TR-TDS was extended for the first time to the MIR

up to 33 THz, to study the time-dependent optical properties of the Si-C stretching mode in SiC.

3.2.1   CEP stable MIR pulses generation and detection

The wavelengths of mid-infrared light are more than one order of magnitude larger than that of commercially available femtosecond laser systems . Typically, two subsequent frequency conversion steps are employed to generate MIR pulses starting from Ti:Sapphire based amplifier systems that produce femtosecond pulses at 800 nm wavelength. Thanks to the properties of the nonlinear optical processes involved, CEP stability can be obtained under certain circumstances as will be described below.
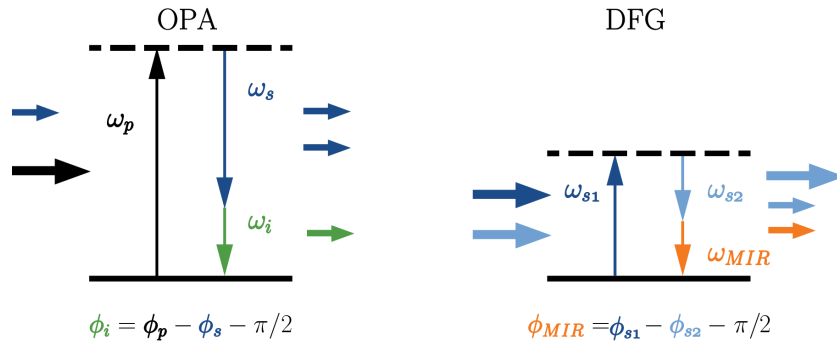

Figure 3.3: Frequency and phase summation rules for Optical Parametric Amplification and Difference Frequency Generation. Formally these two processes are identical, but they are employed in two different ways. In OPA a very week seed at frequency ω_s is amplified by an intense pulse at frequency ω_p, generating a pulse at frequency ω_i as a byproduct. In DFG the pulses at frequency ω_{s1} and ω_{s2} have comparable intensities, and they generate a pulse at frequency ω_{MIR}.

The first conversion step relies on OPA, in which a weak seed at fre-

quency ω_s is amplified by an intense pump pulse at frequency ω_p in a non-linear optical medium. In this process, high energy photons are converted in pairs of lower energy ones, leading to pulses in the 1-2.5 μm wavelength range. The energy conservation imposes that $\omega_p = \omega_s + \omega_i$, where ω_i is the frequency of a pulse generated as a byproduct (see Fig. 3.3, left panel). Furthermore, the ratio ω_s/ω_i can be adjusted by making use of momentum conservation which itself can be controlled by the birefringence of the optical medium. Such adjustable ratio is particularly important because it allows to select, within a certain range, the desired value of ω_s.

The second frequency conversion process is called Difference Frequency Generation (DFG) and takes place in another nonlinear optical crystal. In this process, MIR light is generated at the difference frequency between two input pulses (see Fig. 3.3, right panel). If the frequency of the DFG input pulses can be changed on demand, for example using the outputs of two OPAs tuned at frequencies ω_{s1} and ω_{s2}, the MIR frequency can be arbitrarily changed. This allows to generate short pulses in the 7-80 μm range. In both the OPA and DFG processes, the involved pulses spectral phases are regulated by well defined relations, reported in Fig. 3.3. Such relations can be exploited to generate CEP stable MIR pulses starting from pulses at frequency ω_p that are non-CEP stable (more information on this topic can be found on the appendix section A.1).

For their characterization, the MIR (i.e. sampled) pulses are mixed with a short (i.e. gate) laser pulse in a nonlinear crystal through the Pockels effect which induces birefringence in an electro-optic medium in the presence of an intense electric field [2]. If the sampled and gate pulses propagate in the medium at the same speed, the latter experiences a constant birefringence imparted by the field of the former. Thus the gate pulse polarization is

rotated by an angle proportional to the instantaneous electric field of the MIR. Scanning the time delay between the two pulses and measuring the polarization rotation of the gate allows then to reconstruct the electric field of the MIR pulse in the time domain (see the appendix A.4 for more details). Because the EOS requires scanning the MIR-gate delay, it is not a single-shot pulse characterization method. This is the reason why the MIR pulses employed in time-domain spectroscopy need to be CEP stable, i.e. they must have a shot-to-shot reproducible electric field profile. An example EOS trace of the MIR probe pulses used in this work is shown in Fig. 3.4 together with the corresponding ampltide spectrum.
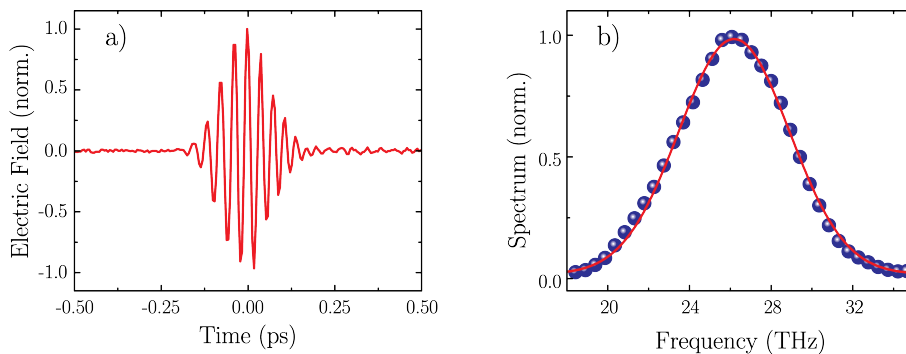

Figure 3.4: a) Time domain profile of a MIR probe pulse with a duration of roughly 100 fs (intensity FWHM) measured with EOS. b) Fourier transform of the EOS trace, showing a broad spectrum centered at 26 THz and with bandwidth ranging from 20 to 32 THz.

3.2.2 Determining the reflectivity

The peculiarity of TDS is its capability of measuring both amplitude and phase of the reflection and transmission coefficients of the investigated sample by directly measuring the electric fields. As mentioned earlier, this allows for the complete reconstruction of the complex optical properties of the

sample. Since this thesis aims at studying the optical properties of SiC close to the phonon resonance, where most of the light is reflected by the reststrahlenband, the following will discuss the measurement of the frequency-resolved reflection coefficient, defined as the ratio between the reflected and incident electric fields E_{ref} and E_{inc}. Assuming the measurement of the electric field profiles in the time domain, the frequency dependent reflection coefficient is calculated from:

$$r(\omega) = \frac{\int_{-\infty}^{+\infty} E_{ref}(t)e^{i\omega t}\, dt}{\int_{-\infty}^{+\infty} E_{inc}(t)e^{i\omega t}\, dt}. \tag{3.1}$$

In a real experiment, the incident electric field is generally not known. The electric field profile of the incident pulse can be measured, for example by freely propagating it towards an EOS setup, but doing this does not preserve the phase difference between the incident and reflected field, therefore defeating the main purpose of TDS. Instead, it is possible to retrieve $r_{sample}(\omega)$ by comparing the electric field reflected from the sample with that reflected from a reference material with a known reflection coefficient $r_0(\omega)$. Because the incident field impinging on the two materials is the same, it can be simplified in the ratio between the two reflection coefficients, leading to:

$$r_{sample}(\omega) = \frac{\int_{-\infty}^{+\infty} E_{ref}(t)e^{i\omega t}\, dt}{\int_{-\infty}^{+\infty} E_0(t)e^{i\omega t}\, dt}\, r_0(\omega), \tag{3.2}$$

where $E_0(t)$ is the electric field reflected by the reference. This technique has been successfully applied in the past to investigate the low-THz optical properties of semiconductors [36, 37, 38, 39]. However, the phases of the reflected pulses can shift when changing from the sample to the reference [38, 39], for example due to misalignment or to shifts in position. An optical path difference Δz between the sample and reference reflections leads to a phase

shift of $2\omega\Delta z/c$. In some cases Δz is known, and the shift can be corrected for in the analysis process [37, 40], in some other cases it can be iteratively adjusted using as benchmark some known optical properties of the sample. If the phase shifts cannot be corrected using one of these methods, they are indistinguishable from real shifts due to the sample optical properties, and therefore affect the reliability of the results. It should also be noted that the phase shift is proportional to the frequency ω, therefore the same optical path change is more detrimental for the MIR frequencies used here than for the low-THz examples in the references.

However, the precise measurement of the static optical properties of the sample is not the aim of this thesis. Instead, the focus here is on the pump-induced time-dependent changes to the static optical properties. These can be obtained from the measurement of the electric field $E_{off}(t)$ reflected from the sample at equilibrium and the changes induced by the pump excitation $\Delta E(t)$. Such measurements can be alternated without moving the sample or changing the alignment, hence they are not affected by the phase problems mentioned above. The pump induced change in the reflection coefficient r is directly related to the change in the reflected electric field by the relation:

$$\frac{\Delta r(\omega)}{r_{off}(\omega)} = \frac{\Delta E(\omega)}{E_{off}(\omega)}, \qquad (3.3)$$

where $r_{off}(\omega)$ is the equilibrium reflection coefficient and $\Delta r(\omega)$ the change induced by the pump pulse. Because the equilibrium property $r_{off}(\omega)$ is known from literature data measured with FTIR techniques, Eq. 3.3 can be used to calculate the non-equilibrium reflection coefficient $r_{on}(\omega)$ as:

$$r_{on}(\omega) = r_{off}(\omega) \left(1 + \frac{\int_{-\infty}^{+\infty} \Delta E(t)e^{i\omega t}\,dt}{\int_{-\infty}^{+\infty} E_{off}(t)e^{i\omega t}\,dt} \right). \qquad (3.4)$$

Once the complex non-equilibrium reflection coefficient is known, all the

other optical properties can be calculated using the relation reported in chapter 1. In particular, the pump induced reflectivity can be calculated recalling that $R_{on}(\omega) = |r_{on}(\omega)|^2$.

3.2.3 Time-resolved measurements on SiC

The combination of the MIR generation and detection schemes presented in section 3.2.1 with an additional pump pulse allows for the reconstruction of the frequency-dependent optical properties as a function of time after excitation of the investigated material.
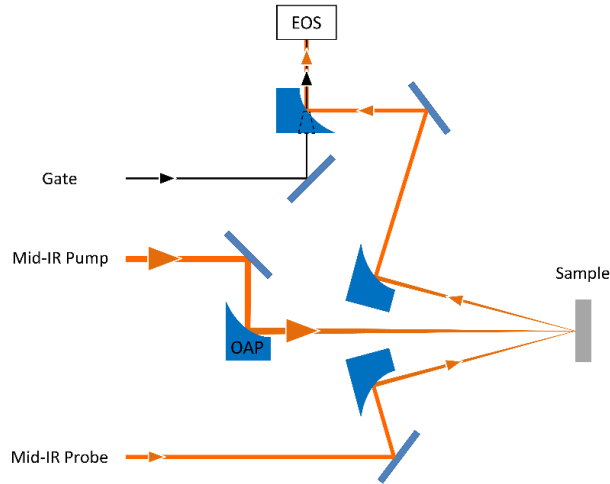

Figure 3.5: Schematic representation of a time-resolved MIR time domain spectrometer (TR-MIR-TDS). OAP - off axis parabolic mirror.

The schematic representation of the time-resolved MIR time-domain spectrometer (TR-MIR-TDS) developed in this work, involving 3 pulses, is reported in Fig. 3.5. The pump is an intense MIR pulse impinging at normal incidence on the sample to drive the SiC infrared active mode to large amplitudes. A weak MIR pulse is used to measure the optical properties in the frequency region of interest. Finally, a third pulse acts as a gate

in the EOS setup which allows for the measurement of the probe electric field profile.

The reconstruction of the time-delay-dependent and frequency-dependent optical properties of the sample requires the two dimensional mapping of the probe electric field as a function of two time coordinates: the pump-probe delay t and the internal EOS time τ [41]. This technique is borrowed from the experiments performed in the low THz frequency range[41, 42], and requires two of the three pulses to be appropriately delayed by mechanical delay stages. Because the path of the probe pulses was fixed, the stage on the pump beam allowed to determine the pump-probe delay t, which is the the *real* time coordinate of the sample optical properties evolution. Once t was set at the beginning of each scan, both stages were moved together to scan the EOS time coordinate τ. This second time coordinate can be thought of as an inverse of the frequency. For each pump-probe delay t, the probe pulse can be characterized by Fourier transforming along the time coordinate τ, to extract the frequency-dependent optical properties. Repeating different τ-scans for each of the desired pump-probe delays t allowed to reconstruct the frequency dependent optical properties at all time delays.

The pump pulses used to drive the SiC stretching mode to large amplitudes were generated by a pair of OPAs seeded by the same whitle light continuum and a DFG setup (see the appendix section A.2 for a detailed description of the setup). This allowed to generate CEP stable MIR pulses of 130 fs duration, 29 THz center frequency, and up to 10 μJ energy, capable of applying peak electric fields up to roughly 9 MV/cm at the sample surface. The center frequency of 29 THz was chosen to maximize the driving of the phonon mode, as discussed in the following.
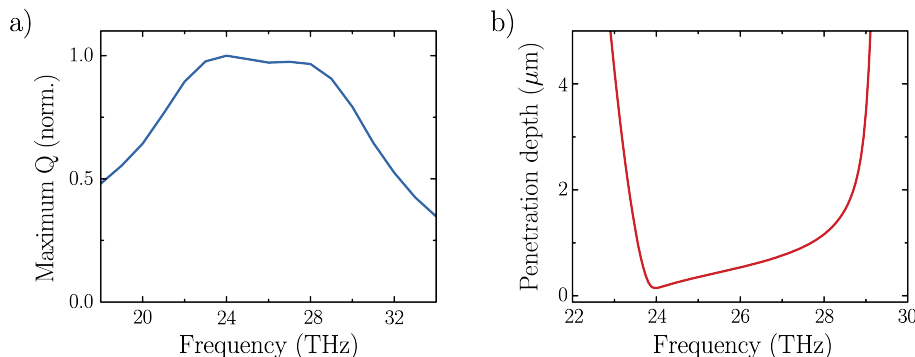
a)

b)

Figure 3.6: a) Maximum value reached by the phonon coordinate Q just below the sample surface as a function of the pumping frequency. These data were calculated with the simulations described in chapter 4, using pump pulses with the same bandwidth as those used in the experiments. b) Frequency dependent penetration depth of 4H-SiC, extracted from a Lorentz fit to literature reflectivity data [30].

Figure 3.6a shows the pump frequency dependent maximum phonon amplitude Q at the sample surface, calculated with the numerical code described in chapter 4. The plot shows that Q has a flat top response in correspondence with the reststrahlenband of the phonon mode. Two relative maxima are evident within such broad peak, one at 24 THz, corresponding to Ω_{TO}, and one at 29 THz, corresponding to Ω_{LO}. The first maximum is due to the *mechanical* response of the phonon oscillator, which at Ω_{TO} is driven exactly at resonance. The second maximum, on the other hand, is due to a divergence of the electric field in the sample given by the zero crossing of ϵ_r happening at Ω_{LO}. In this case, even if the mechanical oscillator is driven farther from resonance, the very large E driver is responsible for the high amplitude reached by Q, which is 90 % of that at Ω_{TO}. The large bandwidth of the pump pulses is then responsible for the merging of these two effects in the flat top profile of Fig. 3.6a. To determine the frequency at which

the effect of the pump pulses is maximized, the value of Q discussed so far has to be combined with the light penetration depth inside the sample, shown in Fig. 3.6b. At Ω_{TO} (24 THz) the phonon can very efficiently screen the incoming radiation, and the penetration depth is only of order 100 nm. At Ω_{LO} instead, the large amplitude driving of Q is combined with a penetration depth of around 4 μm. Thus, even in if the phonon amplitude is comparable, in the latter case the pumped volume is higher, resulting in an higher measured effect.

The probe pulses, used to measure the time-dependent optical response, were also generated by a double OPA and DFG setup (more information on the setup can be found in the appendix section A.3). The 100 fs long pulses had a center frequency of 26 THz, an broad bandwidth extending from 20 to 32 THz covering the entire reststrahlenband. To achieve a non-perturbative probing of the sample properties, the peak electric field was kept two orders of magnitude smaller than that of the pump pulses. A typical probe pulse was shown in Fig. 3.4.

The calculation of the sample time-delay and frequency dependent reflectivity requires the measurement of both the probe electric field reflected at equilibrium as well as the pump induced changes without changing the setup alignment. The straightforward way of doing this, often employed in THz-TDS, is by measuring the equilibrium field $E_{off}(\tau)$ at the beginning of the measurement, and afterwards measuring $\Delta E(t, \tau)$ for the desired pump-probe delays t. It is possible to switch between these measurements by alternatively chopping the probe or the pump beam with a mechanical wheel, and by blocking or opening the pump beam, respectively. This measurement approach is correct under the assumption that the probe electric field is reproducible (i.e. the pulse is CEP stable) on a time scale long enough to

perform the whole measurement. Additionally, the position of the sample should remain constant within a small fraction of the probe wavelength, to avoid phase shifts problems that would make the measurements unreliable.

In general, these assumptions are realistic in the low-THz regime of TDS, where the CEP stability is relying on OR and the wavelengths are of order 100 μm, but become unrealistic when dealing with MIR pulses. First of all, the MIR generation process and CEP stability rely on several cascaded nonlinear optical processes, rather than just OR. Therefore, even small thermal drifts leading to path-length changes of a few microns can lead to seizable phase shifts. The pulses employed in the experiments reported here are usually CEP stable on a few minutes time scale, while drifts should be expected on the few-hours time scale which is necessary to perform a complete pump-probe measurement. The slow CEP drifts can be detected and compensated for by a feedback loop [43], but this requires a significant experimental effort. Furthermore, the shorter wavelengths typical of MIR-TDS require the position of the sample to be stable on the sub-micron scale, a condition significantly more demanding than that of THz-TDS. For these reasons, the experiments reported here were performed chopping both the pump and probe beams at different frequencies with the same mechanical wheel, and simultaneously measuring $E_{off}(\tau)$ and $\Delta E(t, \tau)$ with two lock-in amplifiers in parallel [44].

Figure 3.7a shows an example of raw data for the measured probe pulses, after reflection from the sample, as a function of the EOS time coordinate τ. As mentioned above, both the equilibrium (dashed black) reflected pulse and the pump induced changes (solid red) are recorded simultaneously, and the ratio $\Delta E(\tau)/E_{off}(\tau)$ can be calculated for each EOS measurement. This is then used to calculate the non-equilibrium reflection coefficient $r_{on}(\omega)$ as
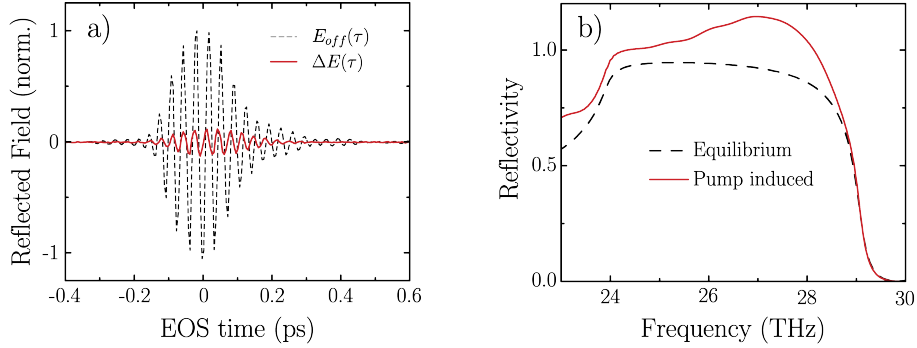
Figure 3.7: a) Example of raw data measured with the TR-MIR-TDS. The dashed line represents the probe electric field $E_{off}(\tau)$ reflected by the sample ad equilibrium as a function of the EOS internal time coordinate τ. The red line is the simultaneously measured change $\Delta E(\tau)$ induced by the pump pulse at some pump probe delay t. b) Equilibrium (dashed line) and pump-induced (solid red line) reflectivity calculated from the data in panel a.

shown in section 3.2.2. Figure 3.7b shows the non-equilibrium reflectivity $R_{on}(\omega)$ (solid red) calculated from the data of Fig. 3.7a, together with the equilibrium one (dashed black).

To sample the electric field transients in EOS, the gate pulses must be shorter than the optical cycle of the sampled pulse. For the frequencies up to 32 THz used in this thesis, the optical period is of order 30 fs. Thus, the gate pulses were generated with a non-collinear OPA and compressed to about 20 fs by a set of chirp mirrors.

3.3   Time-resolved reflectivity of 4H-SiC and phonon amplification

Time-resolved MIR-TDS was employed in this thesis to investigate the response of the Si-C stretching mode of 4H-SiC to an intense resonant excitation and to validate the hypothesis of phonon amplification.
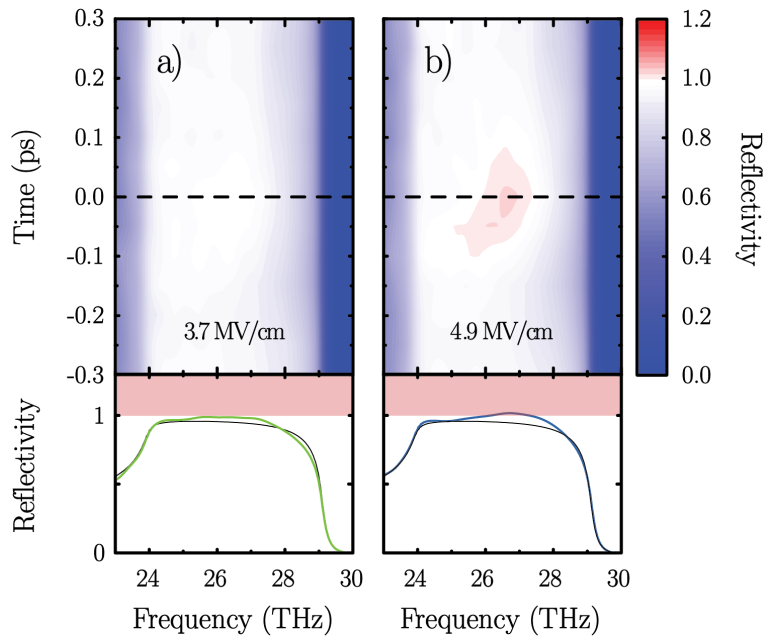

Figure 3.8: Measured pump-probe time-delay dependent and frequency-dependent reflectivity $R(t, \omega)$ for driving peak electric fields of (a) 3.7, (b) 4.9 MV/cm. The color scale is chosen to emphasize in red the areas in which the reflectivity is larger than one. The lower panels represent cuts in the color plots corresponding to the dashed lines in the upper panels. The red shaded area highlights the region of the plots where the reflectivity is larger than one.

Figure 3.8a shows the results time-dependent reflectivity for a pump peak electric field of 3.7 MV/cm. In the color plot the vertical axis represents the pump-probe time delay, and the horizontal axis the frequency. For the cho-

sen pump intensity the reflectivity did not change significantly, especially at times different from zero pump-probe delay. The reststrahlenband, in which the reflectivity is close to one, appears in this plot as the bright area, extending from 24 THz (Ω_{TO}) to 29 THz (Ω_{LO}). A slightly enhanced reflectivity, characterized by a bright white area in the center of the reststahlenband can be seen at zero pump-probe delay (highlighted by the horizontal dashed line). This feature is more evident in the lower panel, showing the frequency-resolved reflectivity at the maximum of the pump-probe response (green) compared to the equilibrium one (black).

Strikingly, for a peak pump field of 4.9 MV/cm the reflectivity exceeded one, as reported in Fig. 3.8b. The area with $R > 1$, emphasized in red in the color plot, developed in the center of the reststrahlenband, around 27 THz, and was persisting for approximately 0.2 ps around the pump pulse arrival time. This feature is further apparent in the lower panel, where the pump-induced reflectivity (blue) reaches the red shaded area, equivalent to $R > 1$. The reflectivity larger than one evidences the amplification of the electric field of the probe pulse. Because the reflectivity in the reststrahlenband is mainly due to the electric field being screened by the phonon, the probe amplification strongly suggests the onset of phonon amplification, as discussed later in more detail.

For the even higher pump peak electric fields of 5.9 MV/cm and 8.7 MV/cm , the area with $R > 1$ broadened in frequency and persisted for longer times, as shown in Figs. 3.9a and 3.9b, reaching values as high as $R \approx 1.15$.

The frequency-dependent non-equilibrium reflectivities at the maximum of the pump-probe responses, corresponding to the lower panels in Fig. 3.8 and 3.9 are reported together in Fig. 3.10a. It is important to note that
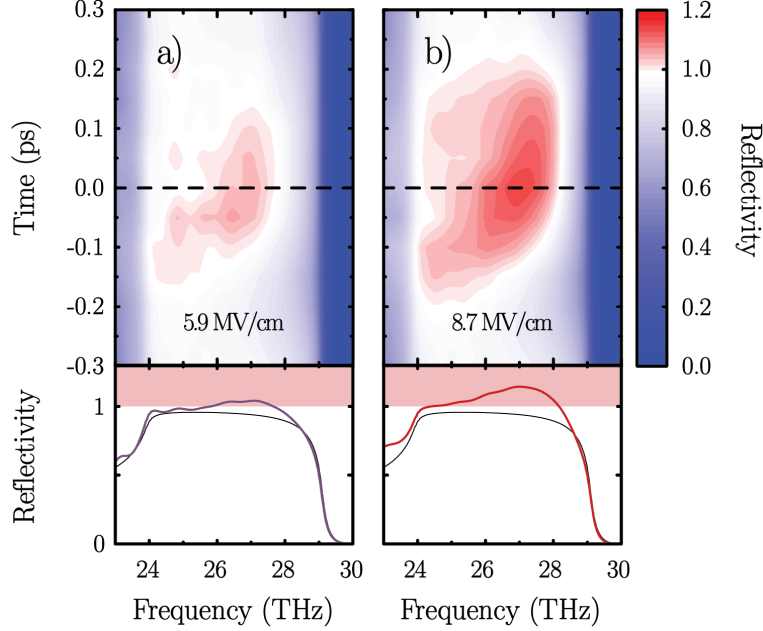
Figure 3.9: Measured pump-probe time-delay dependent and frequency-dependent reflectivity $R(t, \omega)$ for driving peak electric fields of (a) 5.9 and (b) 8.7 MV/cm. The color scale is chosen to emphasize in red the areas in which the reflectivity is larger than one. The lower panels represent cuts in the color plots corresponding to the dashed lines in the upper panels. The red shaded area highlights the region of the plots where the reflectivity is larger than one.

the reflectivity, compared to the equilibrium one, was increased throughout the reststrahlenband, with the position of the maximum slightly increasing in frequency as the pump field was increased. Additionally, the maximum value of the measured reflectivity scaled quadratically with the pump peak electric field, as shown in Fig. 3.10b, where two additional data points corresponding to pump peak fields of 2.0 MV/cm and 2.6 MV/cm are reported. This plot shows that the amplification mechanism scales quadratically with the pump field, highlighting its nonlinear nature. Furthermore, it is possible to identify a threshold of around 4 MV/cm above which the reflectivity

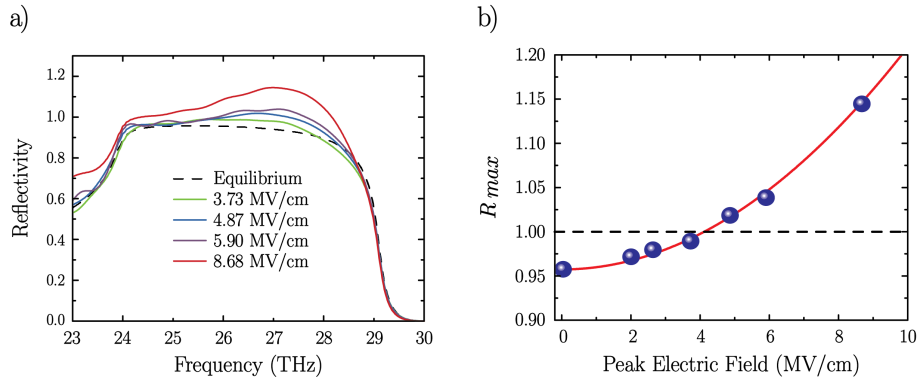a)   b)

Figure 3.10: a) Frequency-dependent measured reflectivity at the maximum of the pump-probe response. These line-outs correspond to the lower panels in Fig. 3.8 and 3.9. The black dashed line represents the equilibrium reflectivity. b) Pump peak field dependence of the maximum measured reflectivity value. In this plot, two additional data points with respect panel a) are shown, corresponding to 2.0 MV/cm and 2.6 MV/cm.

became larger than one.

The amplification of the probe field evidenced here is connected to that of the Si-C stretching mode, as discussed in detail in the next chapter.

Chapter 4

Nonlinear reflectivity and phonon amplification simulations

The most striking experimental result reported in this thesis is the increase above one of the SiC reflectivity in the Si-C stretching mode reststrahlen band. There, the reflectivity is mainly due to the electric field being screened by the phonon, suggesting that the phonon itself is being amplified together with the probe pulses. However, the amplification of the probe and that of the phonon are difficult to compare one-to-one, in particular when the latter is driven to large amplitude and expected to reveal a nonlinear response.

Therefore, the model for the phonon amplification presented in this thesis was implemented in finite difference time domain (FDTD) simulations aimed at reproducing the experimental results. These could provide a deeper insight on the role of the Born effective charge and high frequency permittivity modulations on the lattice dynamics.

4.1   The FDTD method

The FDTD method is a technique commonly used to numerically solve Maxwell's equations in order to describe phenomena in electrodynamics. The name FDTD derives from the fact that Maxwell's equations are solved in the time domain, and that the time and space derivatives present in the equations (in particular Faraday's and Ampere's laws) are approximated with finite differences. The finite differences method considers the Taylor expansion of a function $f(x)$ around $x = x_0$ by a small quantity $\pm \delta/2$

$$f\left(x_0 + \frac{\delta}{2}\right) = f(x_0) + \frac{\delta}{2}f'(x_0) + \frac{1}{2!}\left(\frac{\delta}{2}\right)^2 f''(x_0) + ... \qquad (4.1)$$

$$f\left(x_0 - \frac{\delta}{2}\right) = f(x_0) - \frac{\delta}{2}f'(x_0) + \frac{1}{2!}\left(\frac{\delta}{2}\right)^2 f''(x_0) + ... \qquad (4.2)$$

Subtracting the equations and dividing by δ leads to

$$\left.\frac{df(x)}{dx}\right|_{x=0} \approx \frac{f\left(x_0 + \frac{\delta}{2}\right) - f\left(x_0 - \frac{\delta}{2}\right)}{\delta} \qquad (4.3)$$

where the higher orders in the Taylor expansion have been ignored. It should be noted that the derivative is evaluated at $x = x_0$, while the function is being sampled at $x = x_0 - \delta/2$ and $x = x_0 + \delta/2$. This plays an important role in the discretization of time and space for the solution of Maxwell's equations, as will be discussed later. The approximation of eq. 4.3 becomes exact in the limit of δ going to zero, and is accurate if δ is sufficiently small compared to the scale at which $f(x)$ is changing. When dealing with electromagnetic waves, this means that time and space must be discretized in steps which are small compared to the full periods and wavelengths involved. Furthermore, the Courant-Friedrichs-Lewy stability

condition must be satisfied, which implies that the time step used in the discretization must be smaller than the actual time a wavepacket takes to propagate from one spatial point in the grid to the next:

$$\Delta t \leq \frac{n\Delta z}{c} \qquad (4.4)$$

where Δt and Δz are the time and space grid steps, respectively, c is the speed of light in vacuum and n is the refractive index of the medium in which the material propagates. The Courant stability condition leads to one of the major drawbacks of FDTD, which gets computationally expensive and requires large memory when the space computed is very large compared to the light wavelength, or if very small spatial structures as compared to the wavelength need to be taken into account. In particular, according to eq. 4.4, Δt has to be very small when dispersive or resonant materials are simulated, because in such cases the refractive index can become smaller than one, as discussed in section 1.2.2.

FDTD, on the other hand, is particularly convenient for problems involving few-cycle light pulses because their spatial extent is only a few tenths of the wavelength (i.e. their time extent is only a few tents of the inverse carrier frequency), and when dealing with propagation in bulk materials, for which no small spatial structure is present. In addition, the time domain nature of this framework allows for its natural application to the simulation of time-resolved experiments.

4.1.1   The Yee algorithm

The FDTD simulations used in this thesis are based on the implementation of the algorithm first proposed by Kane Yee in 1966 [45]. In this algorithm,
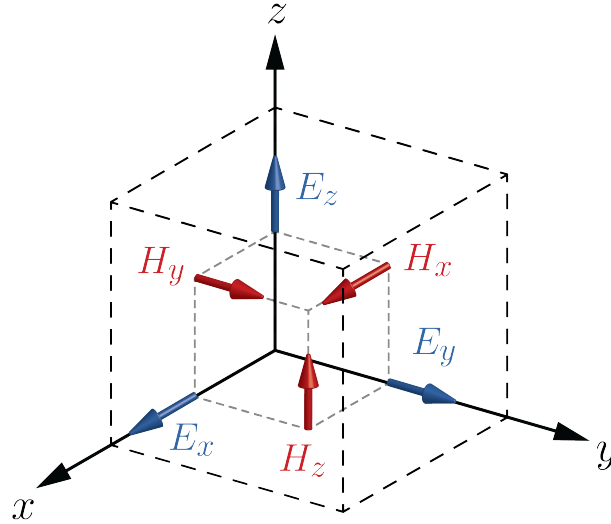
Figure 4.1: Positions at which the electric and magnetic fields are calculated in the Yee cell. The electric field $\vec{E}_x$, $\vec{E}_y$ and $\vec{E}_z$ components are calculated in the middle of the edges, while the magnetic field components $\vec{H}_x$, $\vec{H}_y$ and $\vec{H}_z$ are calculated in the center of the faces.

Maxwell's curl equations (Faraday's and Ampere's laws) are replaced by a set of finite difference equations, with a very practical choice of the grid used to discretize time and space.

The minimum unit of the numerical mesh used to discretize the space is called Yee cell, and is shown in Fig. 4.1. The electric and magnetic fields are defined at staggered positions within the cell, whose boundaries are along the directions of the electric field. In this way, each electric field point is surrounded by four magnetic field points, creating a contour along which the Ampere's law must be satisfied. Analogously, Faraday's law must be satisfied in the contours created by the four electric field points surrounding each magnetic point. It can be shown that the points at which the electric and magnetic fields are calculated are such that the finite difference approach of eq. 4.3 naturally satisfies the Gauss' laws for both the electric
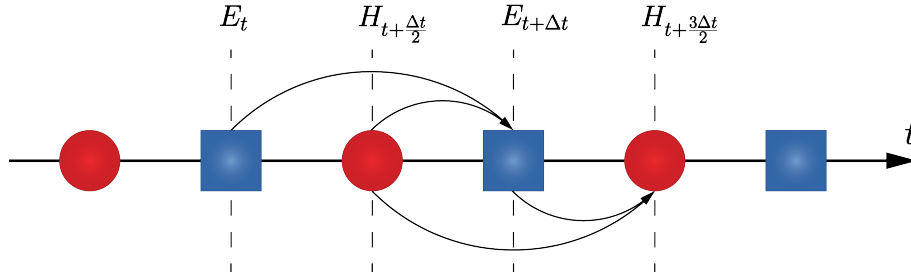
Figure 4.2: *Leap-frog* updating scheme for the electric and magnetic fields in the FDTD algorithm. The fields at two subsequent half-integer time steps are used to calculate the field at the subsequent time step, and the process is repeated for the desired amount of steps.

and magnetic field in the absence of free charges, i.e. if the divergences of both $\vec{E}$ and $\vec{B}$ are zero [46, 47] like in a non-magnetic, dielectric material. This is a consequence of the fact that with finite differences, as pointed out while describing eq. 4.3, if a quantity is evaluated at two given positions, its derivative is evaluated in the middle point. When discretizing space with the Yee grid, the electric field is calculated at integer grid steps, in the middle point of two magnetic fields (which are at half-integer grid steps) and vice versa.

The time derivatives are handled in a similar manner, i.e. with center difference approximations, with the electric and magnetic fields also staggered in time. This means that while the electric field is calculated at integer time steps, the magnetic field is calculated at half-integer time steps.

Once electric and magnetic fields have been staggered in both space and time, and the derivatives have been replaced by finite differences, Maxwell's curl equations can be solved to obtain some *update equations* which express the fields at a certain time step in terms of the fields at the previous time step.

The electric field at time t and the magnetic field at time $t + \frac{\Delta t}{2}$ are used

to calculate the electric field at time $t + \Delta t$. Afterwards, the magnetic field at time $t + \frac{\Delta t}{2}$ and the electric field at time $t + \Delta t$ are used to calculate the magnetic field at time $t + \frac{3\Delta t}{2}$. This update scheme sketched in Fig. 4.2 is called *leap-frog*, and can be repeated in a loop as many times as necessary to let the fields propagate for the desired amount of time.

In the Yee algorithm, the electric rather than the magnetic field is chosen to be along the cell boundaries, as shown in Fig. 4.1. This is a somehow arbitrary choice which is convenient when treating non-magnetic materials, since boundary conditions for the electric field are more common to encounter. For example, one of the advantages of the Yee grid is that if there is an interface between two different dielectric materials, as long as such interface is perpendicular to one of the grid axes, no ad-hoc boundary conditions are required: it is sufficient to define two different values of the electrical permittivity ϵ_r for two subsequent grid positions, and the interface is properly simulated.

4.1.2 Discretization of Maxwell's equations in 1D

The FDTD method is a *full wave* technique, meaning that it solves the full set of Maxwell's equations, which in absence of free charges and currents read:

$$\nabla \cdot \vec{E} = 0 \tag{4.5}$$

$$\nabla \cdot \vec{H} = 0 \tag{4.6}$$

$$\nabla \times \vec{E} = -\mu \frac{\partial \vec{H}}{\partial t} \tag{4.7}$$

$$\nabla \times \vec{H} = \epsilon \frac{\partial \vec{E}}{\partial t} \tag{4.8}$$

where ϵ and μ are the permittivity and the permeability of the medium in which the fields are propagating. Equations 4.5 and 4.6 are intrinsically satisfied by the Yee grid, while eq. 4.7 and 4.8 must be discretized using finite differences. The curl equations can be simplified by considering a one-dimensional space, with the electromagnetic waves propagating along the z direction. This means that along the x and y directions the materials and the fields are uniform, and therefore the partial derivatives $\partial/\partial x$ and $\partial/\partial y$ in the curl operators vanish. Maxwell's equations then reduce to two independent set of equations describing two different propagating modes, one with $\vec{E}$ directed along y and $\vec{H}$ directed along x, and a second vice versa. These two modes propagate independently and are numerically equivalent, thus it is convenient to solve only one of them. This is equivalent to considering linearly polarized light, with the electric field either along x or along y. Considering the electric field along the y direction, eq. 4.7 and 4.8 are reduced to:

$$\frac{\partial \vec{E}_y}{\partial z} = \mu \frac{\partial \vec{H}_x}{\partial t} \tag{4.9}$$

$$\frac{\partial \vec{H}_x}{\partial z} = \epsilon \frac{\partial \vec{E}_y}{\partial t}. \tag{4.10}$$

The partial derivatives of eq. 4.9 and 4.10 can be replaced with finite differences, keeping into account that the electric field in the Yee grid is defined at integer time and space coordinates, while the magnetic field is defined at half integer coordinates, leading to:

$$\frac{E_y|_t^{z+\Delta z} - E_y|_t^z}{\Delta z} = \mu \frac{H_x|_{t+\frac{\Delta t}{2}}^{z+\frac{\Delta z}{2}} - H_x|_{t-\frac{\Delta t}{2}}^{z+\frac{\Delta z}{2}}}{\Delta t} \tag{4.11}$$

$$\frac{H_x|_{t+\frac{\Delta t}{2}}^{z+\frac{\Delta z}{2}} - H_x|_{t+\frac{\Delta t}{2}}^{z-\frac{\Delta z}{2}}}{\Delta z} = \epsilon \frac{E_y|_{t+\Delta t}^z - E_y|_t^z}{\Delta t}. \tag{4.12}$$

The spatial position z can be labeled in the numerical grid with the index k. With the fields staggered in the grid, the same numerical k grid position corresponds to the real position z for the electric field and $z + \frac{\Delta z}{2}$ for the magnetic field. Similarly, $z - \frac{\Delta z}{2}$ is labeled $k-1$ (together with $z - \Delta z$ that does not appear in the equations), and $z + \Delta z$ is labeled $k+1$ (together with $z + 3\Delta z/2$ that does not appear in the equations). Equations 4.11 and 4.12 can therefore be implemented in the spatial grid in the form:

$$\frac{E_y|_t^{k+1} - E_y|_t^{k}}{\Delta z} = \mu \, \frac{H_x|_{t+\frac{\Delta t}{2}}^{k} - H_x|_{t-\frac{\Delta t}{2}}^{k}}{\Delta t} \tag{4.13}$$

$$\frac{H_x|_{t+\frac{\Delta t}{2}}^{k} - H_x|_{t+\frac{\Delta t}{2}}^{k-1}}{\Delta z} = \epsilon \, \frac{E_y|_{t+\Delta t}^{k} - E_y|_t^{k}}{\Delta t}. \tag{4.14}$$

These equations can be solved for the future values of the fields, leading to:

$$H_x|_{t+\frac{\Delta t}{2}}^{k} = H_x|_{t-\frac{\Delta t}{2}}^{k} + \frac{\Delta t}{\mu \Delta z} \left(E_y|_t^{k+1} - E_y|_t^{k} \right) \tag{4.15}$$

$$E_y|_{t+\Delta t}^{k} = E_y|_t^{k} + \frac{\Delta t}{\epsilon \Delta z} \left(H_x|_{t+\frac{\Delta t}{2}}^{k} - H_x|_{t+\frac{\Delta t}{2}}^{k-1} \right). \tag{4.16}$$

Equations 4.15 and 4.16, called *update equations*, depict the fields at position k in the grid at times $t + \frac{\Delta t}{2}$ and $t + \Delta t$ as a function of the fields in the same or adjacent position at previous times. If the fields are known in all the grid at a certain time, it is possible to calculate the fields in all the grid one step in the future. This is achieved with a loop that scans all the k positions and updates the fields. The whole procedure is then repeated in an external loop that cycles through time (labeled with an index T) for as many steps as desired. This is the basic procedure used to propagate electromagnetic fields in the grid solving Maxwell's equations in linear dielectric media without resonances. When practically implementing these equations into an FDTD

simulation, several other aspects must be taken into account, as discussed in the appendix section B.1.

4.1.3 Introduction of a phonon resonance

The FDTD simulations described so far are considering linear, non-resonant materials. In order to simulate the optical properties of a material in the vicinity of a lattice vibrational mode, it is convenient to introduce the auxiliary field $\vec{D}$ which is defined as

$$\vec{D} = \epsilon\, \vec{E} \tag{4.17}$$

and accordingly rewrite Maxwell's curl equations as

$$\nabla \times \vec{E} = -\mu \frac{\partial \vec{H}}{\partial t} \tag{4.18}$$

$$\nabla \times \vec{H} = \frac{\partial \vec{D}}{\partial t} \tag{4.19}$$

together with the constitutive relation

$$\vec{D} = \epsilon_0 \vec{E} + \vec{P} \tag{4.20}$$

where $\vec{P}$ is the polarization due to bound charges.

The introduction of the phonon resonance in the FDTD algorithm requires the equation of motion for the phonon oscillator (eq. 1.13), which considering eq. 1.37 can be written as:

$$\frac{\partial^2 Q}{\partial t^2} + \Gamma \frac{\partial Q}{\partial t} + \Omega_{TO}^2 Q = \Omega_{TO} \sqrt{\epsilon_0\,(\varepsilon_0 - \varepsilon_\infty)}E. \tag{4.21}$$

The feedback of the oscillator coordinate Q on the electric field is given by eq. 4.20, which combined with eq. 1.40 reads

$$D = \epsilon_0 \varepsilon_\infty E + \Omega_{TO} \sqrt{\epsilon_0 \left(\varepsilon_0 - \varepsilon_\infty\right)} Q. \tag{4.22}$$

These two equations must be introduced in the FDTD loop, upon being expressed in terms of finite differences. Equation 4.21 contains a second order time derivative, which is implemented by splitting it in two subsequent steps, defining a displacement current J and rewriting eq. 4.21 as a system of two equations:

$$J = \frac{\partial Q}{\partial t} \tag{4.23}$$

$$\frac{\partial J}{\partial t} + \Gamma J + \Omega_{TO}^2 Q = \Omega_{TO} \sqrt{\epsilon_0 \left(\varepsilon_0 - \varepsilon_\infty\right)} E. \tag{4.24}$$

It is convenient to define J and Q at the spatial grid positions where E is defined, while in time they must be staggered to be updated in a *leap-frog* fashion. Since Q and E will be combined in equation 4.22, they must be defined at the same grid positions. Thus, the former is defined at integer time steps, while J is defined at half integer time steps. The discretization of eq. 4.23 with finite differences leads to:

$$J|_{t+\frac{\Delta t}{2}}^{k} = \frac{Q|_{t+\Delta t}^{k} - Q|_{t}^{k}}{\Delta t} \tag{4.25}$$

which can be solved to obtain the update equation for Q:

$$Q|_{t+\Delta t}^{k} = Q|_{t}^{k} + \Delta t \; J|_{t+\frac{\Delta t}{2}}^{k} . \tag{4.26}$$

The finite difference approximation of eq. 4.24 reads:

$$\frac{J|_{t+\frac{\Delta t}{2}}^{k} - J|_{t-\frac{\Delta t}{2}}^{k}}{\Delta t} + \Gamma \frac{J|_{t+\frac{\Delta t}{2}}^{k} + J|_{t-\frac{\Delta t}{2}}^{k}}{2} + \Omega_{TO}^2 \, Q|_{t}^{k} = \Omega_{TO} \sqrt{\epsilon_0 \left(\varepsilon_0 - \varepsilon_\infty\right)} \, E_y|_{t}^{k} ,$$
$$\tag{4.27}$$

where the value of J at time t has been approximated by the average between its values at $t - \frac{\Delta t}{2}$ and $t + \frac{\Delta t}{2}$. This equation can be solved for the future value of J to obtain the update equation:

$$
\begin{aligned}
J|^k_{t+\frac{\Delta t}{2}} = \left[\frac{2 - \Gamma\Delta t}{2 + \Gamma\Delta t}\right] J|^k_{t-\frac{\Delta t}{2}} &- \left[\frac{2\Omega_{TO}^2 \Delta t}{2 + \Gamma\Delta t}\right] Q|^k_t + \\
&+ \left[\frac{2\Omega_{TO}\sqrt{\epsilon_0\left(\varepsilon_0 - \varepsilon_\infty\right)}\Delta t}{2 + \Gamma\Delta t}\right] E_y|^k_t .
\end{aligned}
\tag{4.28}
$$

The last equation to discretize for the implementation of the phonon resonance is eq. 4.22, which does not contain any derivative and can therefore directly be solved to obtain an update equation for E:

$$
E_y|^k_t = \frac{1}{\epsilon_0\varepsilon_\infty} D_y|^k_t - \frac{\Omega_{TO}\sqrt{\epsilon_0\left(\varepsilon_0 - \varepsilon_\infty\right)}}{\epsilon_0\varepsilon_\infty} Q|^k_t .
\tag{4.29}
$$

Equations 4.26, 4.28 and 4.29 are solved together with Maxwell's curl equations in the FDTD loop to account for the propagation of light in resonant materials. The detailed equations implemented in the FDTD loop are reported in the appendix section B.2.

4.1.4   Calculation of the optical properties from FDTD simulations

The FDTD framework allows to simulate the propagation a light pulse travelling from vacuum through a slab of material. Since interfaces are properly handled, part of the field is going to be reflected, and part of it is going to enter the material. When reaching the end of the slab, this process is repeated, with some of the light exiting the material and propagating again in vacuum towards the end of the grid. Knowing the simulated reflected and transmitted fields as well as the incident one, the material reflection and transmission coefficients can be calculated. This allows then to calculate all

the other optical properties.

The reflected and transmitted fields are extracted from the simulations at the edges of the grid, where the detector cells are defined. Because the reflection and transmission coefficients r and t are in general complex quantities, they depend on the relative phase between the incident and reflected or transmitted fields. To properly calculate r, for example, the reflected field must be divided by the incoming one after the time axis have been properly shifted with respect to each other. This is equivalent to dividing the reflected field by the field $E_{inc,r}$ that would have been reflected by a perfect electric conductor placed in the same position as the studied material. If the electric field inserted at the source is $g(\tau)$ and the field measured at the detector positioned at $k = 1$ is $f(\tau)$, the reflection coefficient is given by:

$$r(\tau) = \frac{E_{ref}}{E_{inc,r}} = \frac{f(\tau)}{-g\left(\tau + \left[\frac{2s}{\Delta z} + 1\right]\frac{\Delta z}{c}\right)}, \tag{4.30}$$

where s is the empty space between the source and the material. The delay in the time axis of $E_{inc,r}$ can be easily understood considering the structure of the grid used in the simulations, depicted in Fig. 4.3. The source is injected at the second grid position, and needs to travel two times the distance s before reaching again the source cell, therefore travelling $\frac{2s}{\Delta z}$ cells, plus one cell to reach the detector at $k = 1$. Since all the cells in which light is travelling are in vacuum, multiplying the number of cells by $\frac{\Delta z}{c}$ gives the time shift required to properly calculate r. The minus at the denominator of eq. 4.30 accounts for the fact that a field reflected by a perfect conductor is flipped. Similarly, the transmission coefficient is
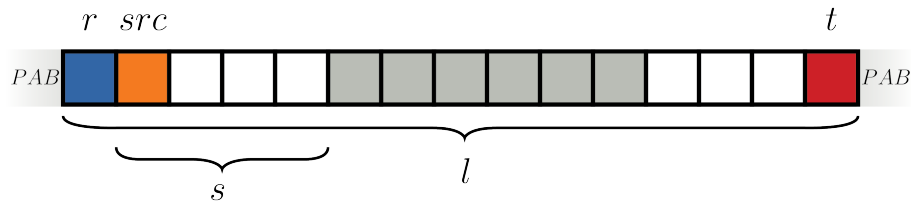
Figure 4.3: Structure of the grid used for the simulations. The source is injected in the second cell, marked with src (orange). The reflected and transmitted light is measured in the first (blue) and last (red) grid cells, marked with r and t, respectively. The total length of the gird is l, and the distance from the source to the surface of the material is s. The white cells are those in which the light propagates in vaccum, while the grey ones are those where the material is present. Outside the grid there are perfectly absorbing boundary conditions (PAB), with light propagating outwards without being reflected (more details can be found in the appendix section B.1).

calculated from

$$t(\tau) = \frac{E_{tr}}{E_{inc,t}} = \frac{h\left(\tau\right)}{g\left(\tau + \left[\frac{l}{\Delta z} - 3\right]\frac{\Delta z}{c}\right)} \tag{4.31}$$

where $h(\tau)$ is the field measured at the transmission detector and l is the total grid size.

4.2   Simulation of the linear reflectivity of SiC

The 1D-FDTD framework was used to simulate the optical properties of SiC in the spectral region around the Si-C stretching mode, extending from approximately 20 to 32 THz. This is done simulating the reflection of a light pulse with central frequency in the middle of the reststrahlenband and a bandwidth broad enough to cover the desired spectral range.
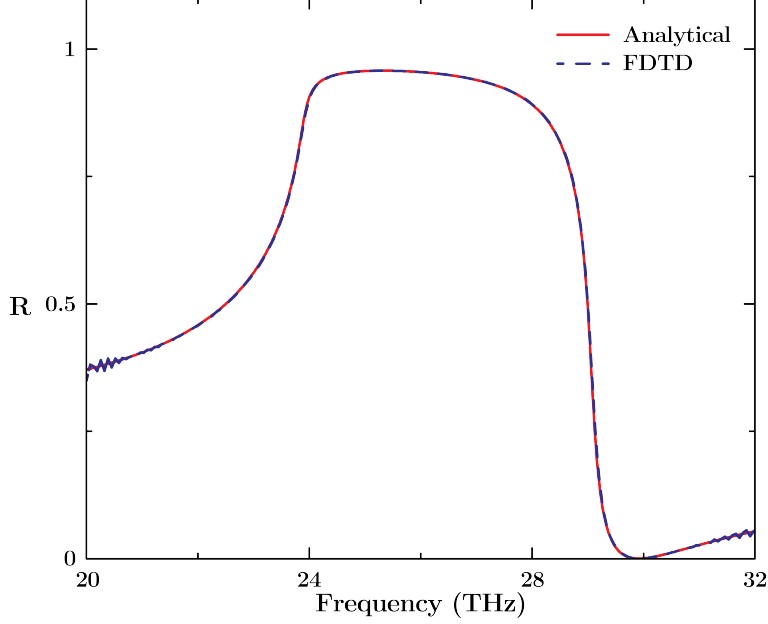
Figure 4.4: Frequency dependent reflectivity calculated from the results of the FDTD simulation (dashed blue) compared to that calculated analytically from the Lorentz model (red). The material parameters used for both the curves are those of hexagonal silicon carbide, with $\varepsilon_0 = 9.66$, $\varepsilon_\infty = 6.52$, $\Omega_{TO} = 24.9$ THz and $\Gamma = 0.2$ THz.

The frequency dependent reflectivity of SiC is then calculated from the Fourier transform of the reflection coefficient $r(\tau)$. Here, it is convenient to Fourier transform the incident and reflected fields before calculating their ratio:

$$r(\omega) = \frac{E_{ref}(\omega)}{E_{inc,r}(\omega)} = \frac{FT\left[f\left(\tau\right)\right]}{FT\left[-g\left(\tau + \left[\frac{2s}{\Delta z} + 1\right]\frac{\Delta z}{c}\right)\right]} \tag{4.32}$$

where FT indicates the Fourier transform. The result of this calculation is shown in Fig. 4.4, where $R(\omega) = |r(\omega)|^2$ is compared to the analytical curve obtained from the Lorentz model described in section 1.2: the agreement between the two curves is very good. The dielectric function $\epsilon_r(\omega)$ or the

complex refractive index $\tilde{n}(\omega)$ can also be calculated from the simulations, as shown in the appendix section B.3.

4.3 Introduction of nonlinearities in FDTD

The linear phonon resonance was introduced in the FDTD framework in section 4.1.3 using the equation of motion for the phonon coordinate Q (see Eq. 4.21) together with the constitutive equation (see Eq. 4.22), which is incorporating the polarization P.

When the electric field is strong enough to drive the system in the nonlinear regime, both these equations have to be expanded to take into account the quadratic dependence on Q of the Born effective charge $Z^* = Z_0^* + \alpha Q^2$ and of the high frequency dielectric constant $\epsilon_\infty = \epsilon_{\infty,0} + 2\beta Q^2$. The following sections will discuss the implementation of the nonlinear equations for P and Q in the FDTD framework.

4.3.1 Nonlinear Polarization

The expansion for the nonlinear polarization of SiC reads, according to eq. 2.23:

$$P = \epsilon_0 \left(\varepsilon_\infty - 1 \right) E + \Omega_{TO} \sqrt{\epsilon_0 \left(\varepsilon_0 - \varepsilon_\infty \right)} Q + \alpha Q^3 + 2\beta Q^2 E \qquad (4.33)$$

and the constitutive equation $D = \epsilon_0 E + P$ therefore becomes:

$$D = \epsilon_0 \varepsilon_\infty E + \Omega_{TO} \sqrt{\epsilon_0 \left(\varepsilon_0 - \varepsilon_\infty \right)} Q + \alpha Q^3 + 2\beta Q^2 E. \qquad (4.34)$$

This equation does not contain time or space derivatives, and can therefore be directly solved for the electric field E before its implementation in the FDTD loop. The discretization gives:

$$
\begin{aligned}
E_y|_t^k = {} & \frac{1}{\epsilon_0 \varepsilon_\infty + 2\beta \left(Q|_t^k \right)^2} \, D_y|_t^k - \frac{\Omega_{TO} \sqrt{\epsilon_0 \left(\varepsilon_0 - \varepsilon_\infty \right)}}{\epsilon_0 \varepsilon_\infty + 2\beta \left(Q|_t^k \right)^2} \, Q|_t^k \\
& - \frac{\alpha}{\epsilon_0 \varepsilon_\infty + 2\beta \left(Q|_t^k \right)^2} \left(Q|_t^k \right)^3,
\end{aligned}
\tag{4.35}
$$

which replaces eq. 4.29 in the FDTD loop.

4.3.2 Nonlinear equation of motion

The nonlinear equation of motion for the phonon oscillator reads, according to eq. 2.25 and 2.26

$$
\frac{\partial^2 Q}{\partial t^2} + \Gamma \frac{\partial Q}{\partial t} + \Omega_{TO}^2 Q = \Omega_{TO} \sqrt{\epsilon_0 \left(\varepsilon_0 - \varepsilon_\infty \right)} E + 3\alpha Q^2 E + 2\beta Q E^2. \tag{4.36}
$$

This equation, containing time derivatives, needs to be discretized in order to calculate an update equation for the future values of Q, with a process similar to that described in section 4.1.3. First of all, the second order time derivative is handled with two subsequent differentiations solving the two equations:

$$
J = \frac{\partial Q}{\partial t} \tag{4.37}
$$

$$
\frac{\partial J}{\partial t} + \Gamma J + \Omega_{TO}^2 Q = \Omega_{TO} \sqrt{\epsilon_0 \left(\varepsilon_0 - \varepsilon_\infty \right)} E + 3\alpha Q^2 E + 2\beta Q E^2. \tag{4.38}
$$

Equation 4.37 can be easily discretized and solved for future values of Q, as shown in section 4.1.3, leading to the update equation:

$$
Q|_{t+\Delta t}^k = Q|_t^k + \Delta t \ J|_{t+\frac{\Delta t}{2}}^k . \tag{4.39}
$$

The finite difference approximation of eq. 4.38 reads

$$
\frac{J|^k_{t+\frac{\Delta t}{2}} - J|^k_{t-\frac{\Delta t}{2}}}{\Delta t} + \Gamma \frac{J|^k_{t+\frac{\Delta t}{2}} + J|^k_{t-\frac{\Delta t}{2}}}{2} + \Omega^2_{TO}\, Q|^k_t \\
= \Omega_{TO}\sqrt{\epsilon_0\left(\varepsilon_0 - \varepsilon_\infty\right)}\, E_y|^k_t + 3\alpha\left(Q|^k_t\right)^2 E_y|^k_t + 2\beta\, Q|^k_t \left(E_y|^k_t\right)^2,
\tag{4.40}
$$

and can be solved for future values of J to obtain the update equation:

$$
J|^k_{t+\frac{\Delta t}{2}} = \left[\frac{2 - \Gamma\Delta t}{2 + \Gamma\Delta t}\right] J|^k_{t-\frac{\Delta t}{2}} - \left[\frac{2\Omega^2_{TO}\Delta t}{2 + \Gamma\Delta t}\right] Q|^k_t + \\
+ \left[\frac{2\Omega_{TO}\sqrt{\epsilon_0\left(\varepsilon_0 - \varepsilon_\infty\right)}\Delta t}{2 + \Gamma\Delta t}\right] E_y|^k_t + \\
+ \left[\frac{6\alpha\Delta t}{2 + \Gamma\Delta t}\right]\left(Q|^k_t\right)^2 E_y|^k_t + \left[\frac{4\beta\Delta t}{2 + \Gamma\Delta t}\right] Q|^k_t \left(E_y|^k_t\right)^2,
\tag{4.41}
$$

which is inserted in the FDTD loop instead of eq. 4.28 to take into account the nonlinear terms. The FDTD loop updated with the nonlinear equations is described in detail in the appendix section B.4.

4.4 Pump-probe measurements simulations

The implementation of the nonlinear phonon response in the FDTD framework allows to simulate the results of pump-probe measurements, in which the strong pump pulse drives the system into the nonlinear regime that is probed by a weak probe pulse in linear response. The simulation of the pump-probe response, and its comparison with the experimental results shown in chapter 3 allows then to test the physical model based on first principle calculations presented in chapter 2.

The simulation of the time-dependent and frequency-dependent optical properties of SiC is performed conceptually in the same way as in the experiment. For each time delay t between the pump and probe pulses, the

reflected probe pulse at equilibrium (i.e. without the sample being excited by the pump) must be compared to that reflected out of equilibrium (i.e. after the sample has been excited by the pump). Experimentally this is achieved by mechanically chopping at different frequencies both the pump and probe beams. Numerically the same information is obtained by performing sets of three simulations for each pump-probe delay.

In the first simulation, an electric field profile entailing both the pump and the probe pulses separated by a time t is injected in the grid, as depicted in Fig. 4.5a. This electric field E_{ppp} impinges on the sample, gets partially reflected, reaches the detector cell placed at the position $k = 1$ of the grid (see Fig. 4.3) and gets recorded as $E_{r,ppp}$. In the second simulation, only the pump pulse E_{pum} is injected in the grid, as shown in Fig. 4.5b, and the reflected field $E_{r,pum}$ is recorded by the detector. Finally, a third simulation in which only the probe pulse E_{pro} impinges on the sample (Fig. 4.5c) is performed, and the reflection $E_{r,pro}$ is recorded. The three reflected quantities $E_{r,ppp}$, $E_{r,pum}$ and $E_{r,pro}$ can be used to retrieve the nonlinear optical properties of the sample. At first, the probe electric field E_{on} reflected from the excited sample is calculated from

$$E_{on} = E_{r,ppp} - E_{r,pum}. \tag{4.42}$$

This equation 4.42 allows to isolate the probe reflected field from that of the pump, under the assumption that the probe field is weak enough to only *interrogate* the state of the sample without further perturbing it. This is a general assumption at the basis of the pump-probe technique, which was tested for the simulation scheme presented here (see the appendix section B.5). With $E_{off} = E_{r,pro}$, the change in the sample reflection coefficient r due to the pump pulse can be calculated as
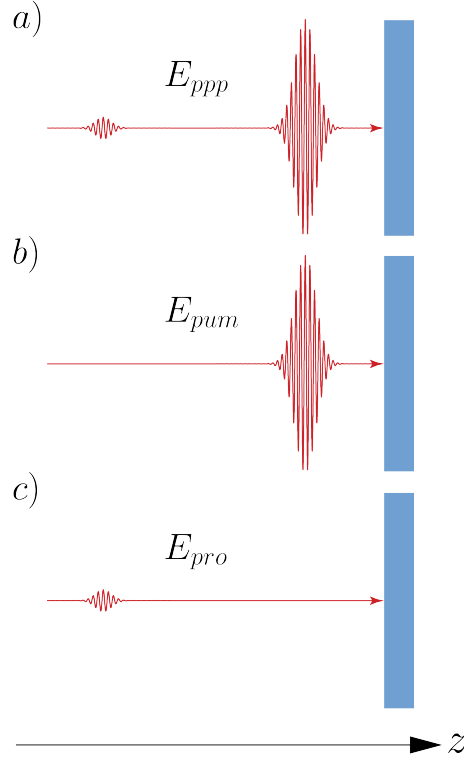
Figure 4.5: Schematic representation of the three simulations performed to calculate the nonlinear optical properties for each pump-probe delay t. The first simulation (a) entails both the pump and the probe pulses propagating in the z direction and impinging on the sample surface. The electric field injected in the grid is E_{ppp}. The second simulation (b) entails only the pump pulse E_{pum}, and the third simulation (c) involves only the probe pulse E_{pro}. The intensity of the probe pulse, usually two orders of magnitude smaller than the pump, has been increased for illustrative purposes.

$$\frac{\Delta r}{r} = \frac{\Delta E}{E} = \frac{E_{on} - E_{off}}{E_{off}}. \tag{4.43}$$

It is important to note that the probe electric field is recorded in the FDTD algorithm as a function of the *simulation time*. This corresponds to the experimental EOS delay τ, and must not be confused with the pump-probe

delay time t. The frequency dependent change in the reflection coefficient is calculated by Fourier transforming $E_{on}(\tau)$ and $E_{off}(\tau)$ to obtain $E_{on}(\omega)$ and $E_{off}(\omega)$. The Fourier transform is performed before the calculation of $\Delta r/r$ to avoid dividing two quantities oscillating around zero. The non-equilibrium value of the reflection coefficient $r_{on}(\omega)$ can then be calculated as

$$r_{on}(\omega) = r_{off}(\omega) \left(1 + \frac{\Delta r(\omega)}{r_{off}(\omega)} \right) \tag{4.44}$$

where $r_{off}(\omega)$ is the equilibrium reflection coefficient of eq. 4.30. Once the complex reflection coefficient is known, all the other optical properties can be analytically computed, as described in chapter **??**.
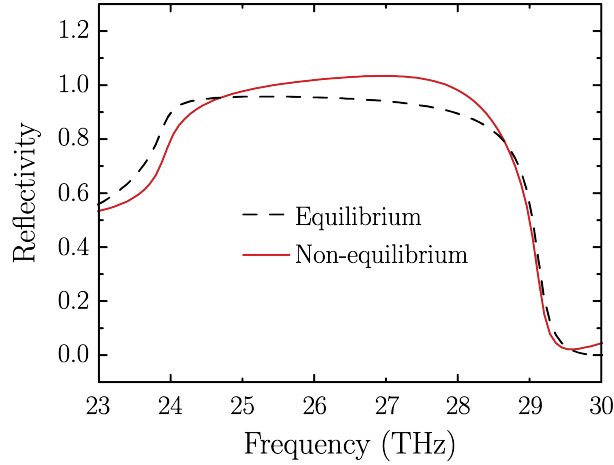

Figure 4.6:   Example of frequency-dependent non-linear reflectivity $R_{on}(\omega) = |r_{on}(\omega)|^2$ calculated from eq. 4.44 for one specific pump-probe delay t (red line) compared to the equilibrium reflectivity $R_{off}(\omega) = |r_{off}(\omega)|^2$ (dashed black).

An example of simulated non-equilibrium reflectivity $R_{on}(\omega) = |r_{on}(\omega)|^2$ is shown in Fig. 4.6, together with the equilibrium one $R_{off}(\omega) = |r_{off}(\omega)|^2$. The pump-probe measurements can therefore be simulated by repeating a

set of three simulations, as discussed above, for each of the desired pump-probe time delays t.

4.5 Simulation of phonon amplification in SiC

The pump-probe FDTD simulations were used to simulate the amplification of the Si-C stretching mode in silicon carbide. To replicate the experimental conditions, the pump pulses were tuned at 29 THz, with a time duration of 130 fs, and their peak electric field was adjusted from 2 to roughly 9 MV/cm. The probe pulses, on the other hand, were 100 fs long and centered at 26.5 THz, with spectral content covering the whole Reststrahlenband. The peak field of the probe pulses was kept at a constant value of 86.8 kV/cm for all simulations. This is two orders of magnitude smaller than the highest simulated pump field, and small enough to be in the regime of linear probing, as shown in the appendix section B.5. The investigated pump-probe delay ranged from -0.3 ps to 0.3 ps in steps of 50 femtoseconds, defining time-zero as the peak of the pump-probe response.

4.5.1 Time and frequency dependent reflectivity

The key experimental result of this thesis is the amplification of the Si-C stretching mode in silicon carbide induced by a strong-field resonant excitation. This striking phenomenon is manifesting in the measurements as an increase of the reflectivity above one, evidencing an amplification of the probe pulse. The simulations presented here show that the probe amplification is an indication of that of the phonon, and provide a deeper insight on the role played by the lattice anharmonicities.

When describing the model for the phonon amplification in chapter 2,

the two nonlinear contributions resulting from the Q^2-modulations of the Born effective charge Z^* and dielectric constant ε_∞ were introduced separately. While these two effects cannot be experimentally isolated, in the simulations it is possible to switch the nonlinearities on and off independently, to elucidate their effect on the time and frequency dependent reflectivity and on the phonon coordinate oscillations amplitude.
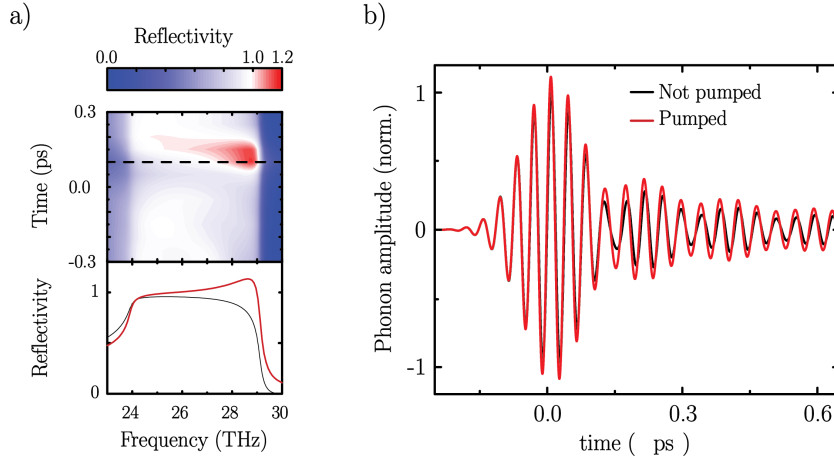

Figure 4.7: Results of the simulations where only the Born effective charge Z^* is modulated, with $\alpha = 7.1 \cdot 10^{27} \frac{A \cdot s}{\sqrt{m \cdot Kg^3}}$ and a driving peak electric field of 8.7 MV/cm. The value of nonlinear coefficient was adjusted to reach a maximum reflectivity of approximately 1.15, analogous to that measured experimentally. (a) Color plot: pump-probe time-delay dependent and frequency-dependent reflectivity $R(t, \omega)$. The color scale is chosen to emphasize in red the areas in which the reflectivity is larger than one. Lower panel: frequency cut corresponding to the dashed line in the color plot. (b) Oscillations of Q at the sample surface induced by the probe pulse with (red) and without (black) the pump at the delay indicated by the dashed line in the color plot.

The results of a simulation accounting for the sole modulation of the

Born effective charge are shown in Fig. 4.7. In particular, the color plot of Fig. 4.7a displays the time and frequency dependent reflectivity, showing areas in which $R > 1$ and proving that a change in Z^* proportional to Q^2 can lead to the amplification of the probe pulses. However, as depicted in the lower panel of Fig. 4.7a, the simulated increase in R has a prominent peak at $\Omega_{LO} = 29$ THz, and is therefore different from that measured experimentally, which shows a maximum in the center of the reststrahlenband. This implies that the modulation of Z^* alone cannot explain the experimental results. Nonetheless, this simulation corroborates the fact that an amplification of the probe pulse in the reststrahlenband is related to an amplification of the phonon coordinate. This is shown in Fig. 4.7b, displaying the oscillations of the phonon coordinate at the sample surface induced by the probe pulse both at equilibrium and in the pumped state, where the amplitude is clearly amplified.

Figure 4.8 shows the results of another simulation, taking into account only the modulation of the high frequency dielectric constant ϵ_∞. Also in this case, the color plot reporting the time and frequency dependent reflectivity (Fig. 4.8a, upper panel) shows areas in which the reflectivity exceeds one. In this case though, the frequency cut of the lower panel displays a rather featureless increase of the reflectivity, with the maximum at $\Omega_{TO} = 24$ THz, and a smaller feature at $\Omega_{LO} = 29$ THz. This reflectivity is also different from that measured experimentally, implying that also the modulation of ϵ_∞ alone cannot properly explain the experimental results. However, also in this case the amplification of the probe pulse is accompanied by that of the phonon, as shown in Fig. 4.8b.

The different effects of the Z^* and ϵ_∞ modulations on the time and frequency dependent reflectivity can be understood with the model for the
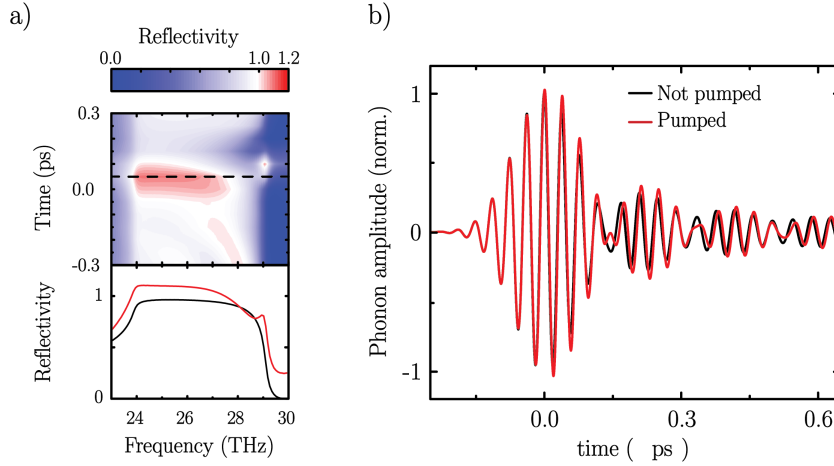
Modulation of ε_∞ only

Figure 4.8: Results of the simulations where only the high frequency dielectric constant ϵ_∞ is modulated, with $\beta = 8.6 \cdot 10^8 \, \frac{A^2 \cdot s^4}{m^2 \cdot Kg^2}$ and a driving peak electric field of 8.7 MV/cm. The value of nonlinear coefficient was adjusted to reach a maximum reflectivity of approximately 1.15, analogous to that measured experimentally. (a) Cclor plot: pump-probe time-delay dependent and frequency-dependent reflectivity $R(t, \omega)$. The color scale is chosen to emphasize in red the areas in which the reflectivity is larger than one. Lower panel: frequency cut corresponding to the dashed line in the color plot. (b) Oscillations of Q at the sample surface induced by the probe pulse with (red) and without (black) the pump at the delay indicated by the dashed line in the color plot.

phonon amplification described in chapter 2. According to such model, the modulation of Z^* leads to an additional driving term in the lattice equation of motion at three times the frequency of the pump. On the other hand, the modulation of ϵ_∞ causes a modulation of the oscillator eigenfrequency at twice the frequency of the pump. Thus, these two effects are affecting the dynamics of Q in rather different ways, and a different outcome is therefore unsurprising. However, both these effects are expected to entail phonon

amplification, as confirmed by the simulations shown here. It should be noted that the effects on the pump-probe of the two modulations are somehow complementary: the change of Z^* increases the reflectivity in the areas where that of ϵ_∞ decreases it, and vice-versa. An interplay between these two effects is therefore likely to reproduce the experimental results, with both modulations active at the same time.
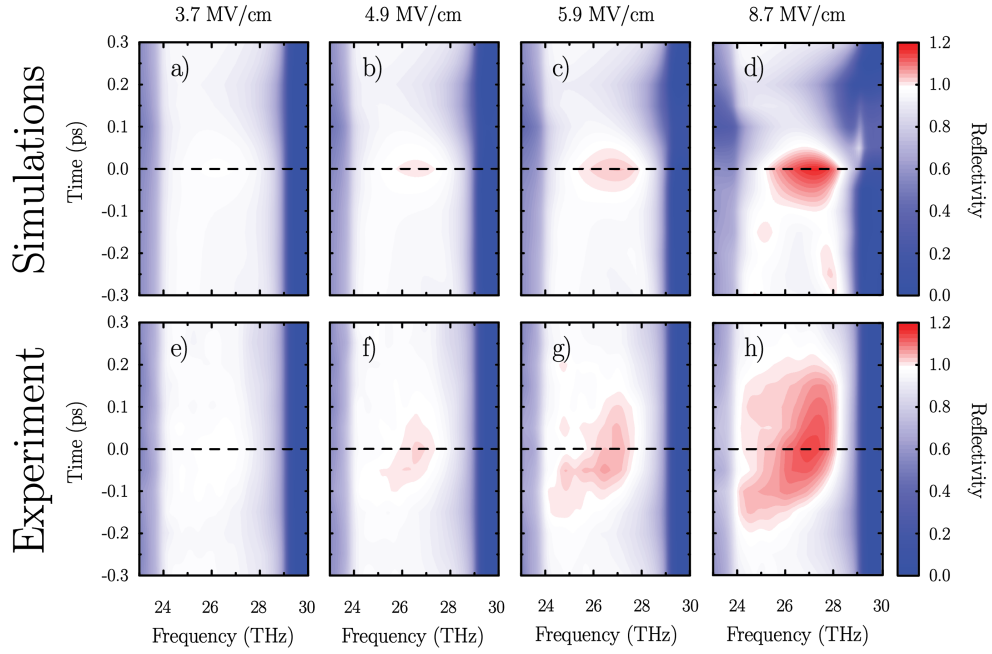

Figure 4.9: Simulated (a-d) and experimental (e-h) pump-probe time-delay dependent and frequency-dependent reflectivity $R(t,\omega)$ for the different driving peak electric fields written above. The values of the nonlinear coefficients in the simulations are $\alpha = 2.48 \cdot 10^{28} \frac{A \cdot s}{\sqrt{m \cdot Kg^3}}$ and $\beta = 3.04 \cdot 10^9 \frac{A^2 \cdot s^4}{m^2 \cdot Kg^2}$. The color scale is chosen to emphasize in red the areas in which the reflectivity is larger than one.

The simultaneous modulation of Z^* and ϵ_∞ allows to reproduce the experimental results, confirming the amplification of the Si-C stretching mode. The agreement between the simulations and experiments is evidenced in

Figure 4.9a-d that shows the time and frequency dependent reflectivity resulting from simulations in which the modulation coefficients were adjusted to fit the experimental results. These simulations reproduce well the main features of the experimental pump-probe traces of panels (e) to (h), with the reflectivity increasing and exceeding one for pump peak electric fields above 4 MV/cm. The area in which $R > 1$ emerges from the center of the reststrahlenband, and expands in both frequency and time as the pump field is increased.
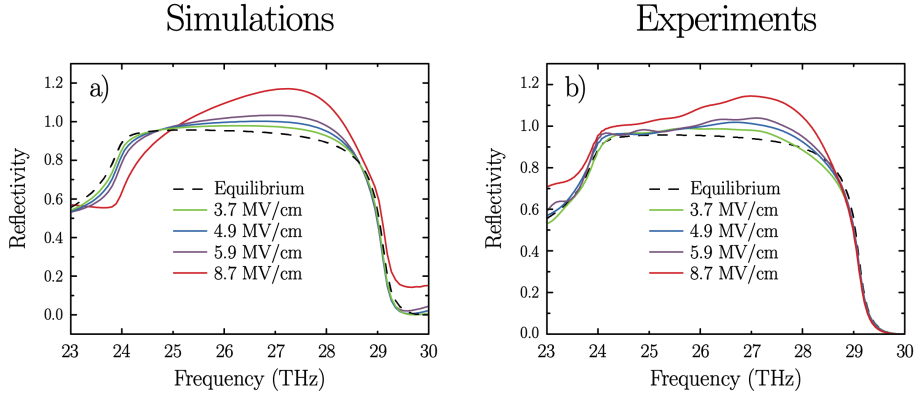

Figure 4.10: Frequency-dependent simulated (a) and experimental (b) reflectivity at the maximum of the pump-probe response. These line-outs correspond to the dashed lines in the 2D plots in Fig.4.9. The black dashed lines represent the equilibrium reflectivity.

The simulated frequency-dependent reflectivity at the maximum of the pump-probe response is shown in Fig. 4.10a, with the reflectivity maximum between 27 and 28 Thz, also replicating the experimental results of Fig. 4.10b. Additionally, the maximum simulated reflectivity R_{max}, defined as the maximum of the curves in Fig. 4.10 scales quadratically with the pump peak electric field, as shown in Fig. 4.11 where the red lines represents parabolic fits to the data.
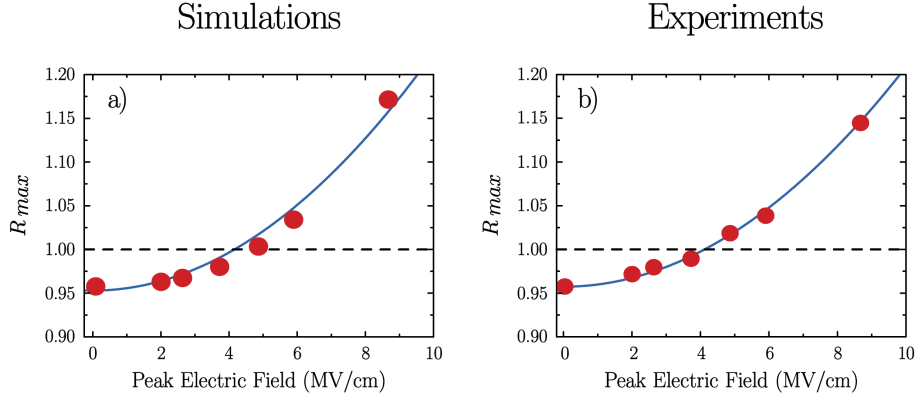
Figure 4.11: Peak field dependence of the maximum calculated (a) and experimental (b) reflectivity value. In this plot, two additional data points with respect to Fig. 4.9 and 4.10 are shown, corresponding to 2.0 and 2.6 MV/cm.
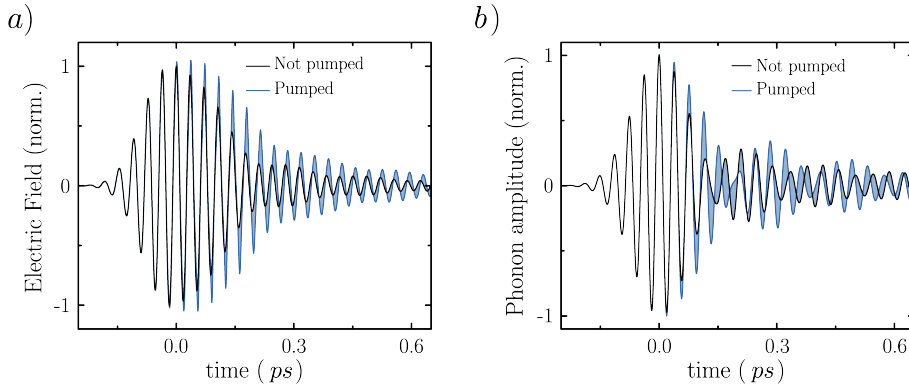

Figure 4.12: Simulated electric field $E_{surf}(\tau)$ (panel a) and phonon coordinate $Q_{surf}(\tau)$ (panel b), driven by a weak probe pulse, with (colored solid lines) and without (black lines) pump excitation. The blue shaded areas represent the difference between the to curves, highlighting amplification of both the electric field and the phonon coordinate .

The amplification of the phonon coordinate Q oscillations together with that of the electric field of the probe is confirmed also when both Z^* and ϵ_∞ are modulated, as shown in Fig. 4.12. In particular, Fig. 4.12a shows the electric field just below the sample surface as a function of time, due

to the impinging probe pulse. When the sample is pumped (blue line) the electric field in the sample is higher than at equilibrium (black line). The same holds for the oscillations of the phonon coordinate Q shown in Fig. 4.12b.

In general, the results of these simulations match quite well the main features of the experiment, as discussed above. Nonetheless, for the highest pump peak field of 8.7 MV/cm the simulated curves show some discrepancies with the measurement. In Fig. 4.9d, for example, some red areas (i.e. with $R > 1$) appear at negative time delays, as well as a pronounced depletion of the reflectivity around Ω_{LO} at 0.2 ps pump-probe delay, all features not present in panel (g). Figure 4.10a (purple line) is also affected, with the reflectivity showing some depletion around Ω_{LO} which is not present in panel (b). These discrepancies might be ascribed to both limitations of the simulation scheme or the relatively simple physical model presented here.

From a physical point of view, the quadratic modulation of the Born effective charge Z^* and dielectric constant ε_∞ might not be accurate enough for completely reproducing the experimental nonlinear optical properties of SiC. These two expansion terms of the phenomenological energy density functional were chosen among the five symmetry allowed ones because they were entailing the highest energy contributions in the DFT calculations. A more complex model, including the effects of the remaining expansion coefficients might help improve the simulations results. Furthermore, the oscillator damping was considered constant throughout all the simulations presented here. However, Γ is a phenomenological term introduced in the Lorentz model to embody the lattice nonlinearities leading to energy flow among phonon modes, which is reasonable to imagine changing when the phonon is driven to large amplitude. The introduction of an oscillator damp-

ing that depends on the pump might for example smooth the features of the simulated reflectivity, increasing the time extent of the amplification in Fig. 4.9a-d, which is always shorter than the corresponding experimental one.

In addition, the discrepancies between the simulations and the experiment could partly be assigned to the one-dimensional nature of the simulations performed here. The angle between the pump and probe beams, present in the experiment but not in the simulations, could indeed play a role in the shape of the pump-probe traces. This can be thought of as a phase-matching problem, in which the non-trivial interaction between the pump and the probe in the strongly driven regime might be re-shaped in different ways along different propagation directions. In this case the same physical model presented here, together with a 2D simulation environment, could better reproduce the experimental results.

The implementation of other nonlinear terms, as well as the extension of the FDTD algorithm to a 2D space, could be introduced in future implementations of the simulations presented here.

Summary and outlook

Summary

This thesis reports the first experimental demonstration of the parametric amplification of an optical phonon. The amplification of phonons was so far limited to the case of acoustic modes, either driven by electrical currents [11] or microwaves [13], and to optical phonons driven by drifting electrons [14]. The results of this thesis extend the phononic amplification to resonantly driven optical modes, which are connected to many interesting phase transitions and whose amplification may be conducive to new physics and applications.

In detail, the response of an infrared active mode driven to very large amplitudes by a strong resonant excitation was studied in the dielectric silicon carbide. The Si-C stretching mode was driven with very intense laser pulses at mid-infrared frequencies, and its optical response was investigated by measuring the time-resolved and frequency-resolved reflectivity across the reststrahlenband with a weak probe pulse. The reflectivity was found to increase above one, evidencing the probe pulse amplification, and strongly suggesting that of the optical phonon.

The nonlinear phononic response was modeled with an anharmonic expansion of the lattice potential in the Lorentz model. This approach was

supported by first principle calculations showing that the dielectric properties of the material are modulated under intense applied electric fields and consequently large ionic displacements. In particular, the Born effective charge Z^* and the high frequency dielectric constant ϵ_∞ increase proportional to the square of the lattice displacement Q. When the phonon mode is driven to large amplitude by a strong resonant excitation, these are modulated at twice the frequency of the driver, and act themselves as a parametric drive for the lattice oscillations.

The amplification of the optical phonon together with that of the probe pulse were validated by numerical simulations in which the interaction of both the pump and probe pulses with the sample were taken into account. If the quadratic dependence on the phonon coordinate Q of both Z^* and ϵ_∞ were introduced, the simulations reproduced well the main features of the experimental results and showed the amplification of the phonon coordinate.

Outlook

The optical phonon amplification presented in this thesis is in fact a parametric gain resulting from *phononic four wave mixing*, a generic mechanism that could be extended to all polar modes in solids and may be conducive to new interesting physical phenomena and applications.

The physics presented here can be steered towards the amplification or attenuation of phonons on demand, allowing for the manipulation of the lattice response, with natural application to the control of structural phase transitions and of many body states that rely on electron-phonon or spin lattice interactions. For example a recent theory has emerged [48, 49] suggesting that amplification of pairs of squeezed phonons may play a key

role in the context of light enhanced superconductivity in cuprates [17, 18, 19] and in the doped fullerites [20]. Such amplification process may be the result of a four wave vibrational mixing analogous to that described here.

Moreover, the extension of the nonlinear phononics to higher orders presented here may reveal a broader set of *phononic analogies* of the well known nonlinear optical properties, paving the way for the realization phononic devices. These physics could be extended to the control of phonon-polariton waves, interesting in the context of information transport [50]. For example, the lattice anharmonicities may lead to the formation of mechanical solitons propagating without damping in the materials.

The fast growing field of lattice dynamics control with light calls for the development of new techniques aimed at the manipulation of intense mid-infrared pulses. The main goal of the experiments presented in this thesis was to drive the lattice vibrations to the largest possible amplitude, therefore requiring very short pulses leading to the highest peak fields. Nevertheless, in the more general context of lattice dynamics manipulation, appropriately tailored pulses are expected to be a powerful tool. Their temporal shaping, for example, would allow to investigate the effects on the lattice of pulses with the same energy but different peak fields. In addition, complex pulse shapes entailing different time delayed sub-pulses could allow for the reversible control of phase transitions on ultrafast time scales. Moreover, the control on the pulses bandwidth would allow for a more selective photoexcitation, targeting single vibrationals mode among closely frequency-spaced ones.

However, because of the long wavelengths, the manipulation of mid-infrared pulses is a challenge from the technological point of view. Two optical developments aimed at the control of the spectral phase and band-

width of pulses at wavelengths longer than 10 μm are reported in the appendices C and D, respectively. These sources, albeit not directly employed in the experiments described in the main body of this thesis, are likely to help advancing the filed of condensed matter control with light.

Appendix A

Experimental methods

This appendix reports additional details on the generation and characterization of the carrier envelope phase stable mid-infrared pulses employed in the experiments discussed in chapter 3, as well as a schematic overview of the complete experimental setup.

A.1   Passive CEP stability

The carrier envelope phase (CEP) of a laser pulse is the relative phase that the electric field profile has with respect to its envelope. Figure A.1 shows two examples of pulses with the same envelope but different CEPs.

A laser source is called CEP stable if all the generated pulses have the same CEP. The CEP stability is a fundamental requirement for the pulses characterization through gating techniques like EOS, that require the electric field profile to be reproducible among several pulses. However, most commercially available laser sources are not CEP stable.

CEP stable pulses can be generated starting from non-CEP stable sources by exploiting the existing phase relations between the pulses involved in
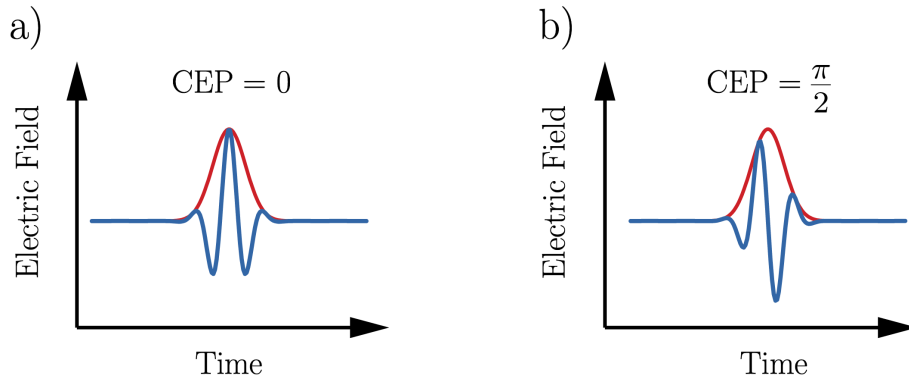
a) b)

Figure A.1: Esample of pulses with the same intensity envelope (red lines) but different electric field profiles (blue lines) because of the different CEP.

nonlinear optical processes [1].

The nonlinear optical properties of interest for the generation of MIR pulses are four wave mixing (FWM), which is the process leading to the generation of the white light continuum (WLC), and OPA/DFG.

FWM involves pulses at four different frequencies, which are related by energy conservation so that $\omega_4 = \omega_1 - \omega_2 + \omega_3$. The relation between the pulses CEPs, on the other hand is, $\phi_4 = \phi_1 - \phi_2 + \phi_3 - \pi/2$. The spectral broadening that leads to WLC generation is due to self phase modulation, which is a FWM process among different spectral component of the same pulse, that have the same spectral phase. Thus, if the CEP of the pulse before the spectral broadening is ϕ_0, the white light continuum will have phase $\phi_{WLC} = \phi_0 - \phi_0 + \phi_0 - \pi/2 = \phi_0 - \pi/2$. This means that the phase of the WLC is locked to that of the starting pulse.

The WLC is then used as a seed and amplified in the OPA process,

---

[1]These CEP stabilization mechanisms are referred to as *passive*, because they rely only on fundamental properties of nonlinear optics and not on feedback loops acting back on the source [51].

becoming the singnal output. In OPA, the spectral phases also have a well defined relation: $\phi_i = \phi_p - \phi_s - \pi/2$, where i, p and s stand for idler, pump and signal, respectively, and the signal mantains the spectral phase of the seed. If two OPAs are seeded by the same WLC, the signal outputs will therefore have both phase $\phi_{s1,s2} = \phi_0 - \pi/2$.

The DFG process also has a fixed phase relation between the interacting pulses: $\phi_{DFG} = \phi_1 - \phi_2 - \pi/2$ where ϕ_1 and ϕ_2 are the phases of the input pulses. If these are the OPA signal outputs $s1$ and $s2$, the DFG pulses will have phase $\phi_{DFG} = -\pi/2 = const.$, i.e. they will be CEP stable.

A.2   MIR pump generation setup

The MIR pump pulses used in the experiments reported in this thesis were generated by a pair of two-stages OPAs seeded by the same white light continuum. The system was pumped with 4.5 mJ pulses at 800 nm wavelength and 100 fs pulse duration from a commercially available Ti:sapphire amplified laser system. A small portion of the input pulses energy (on the order of a few μJ) was tightly focused with a lens on a 2 mm thick sapphire plate, where self-phase modulation (SPM) lead to a broadening of the spectrum and to the generation of a white light continuum (WLC). The WLC was then collimated by a second lens and divided in two equal portions by a 50% beam splitter, to feed the two OPAs first stages.

The first stages of parametric amplification took place in 2 mm thick type-II BBO crystals. The 800 nm pump pulses had 120 μJ energy and were focused on the BBO crystals to reach tens of GW/cm^2 peak intensities. The WLC was also focused, to match the pump spot sizes, and was combined with the pump by means of dichroic mirrors. Amplification of

selected wavelengths witnhin the WLC spectrum was achieved by fulfilling the non-collinear phase matching condition by rotating the BBO crystals. The signals output energies were in the 9 to 11 μJ in each of the first stage OPAs, depending on the desired wavelength, and were spatially separated from the residual pump and idler pulses.

The second stages of amplification took place in 3 mm thick type-II BBO crystals. In this case, both the seeds (i.e. the signal outputs from the first stages) and the pump pulses were collinear and collimated on the BBOs. The pump energies for the second stages was 1.8 mJ, allowing to amplify the signals up to hundreds of microjoules. Because of the collinear geometry, the signals were separated from the residual pumps and idlers with dichroic mirrors. The experiments reported in this thesis were performed tuning the two OPAs at 1.28 μm and 1.46 μm, as shown in Fig. A.2. At these wavelengths the output pulses had 280 μJ and 300 μJ energy, respectively, and the pulse duration was approximately 70 fs for both.
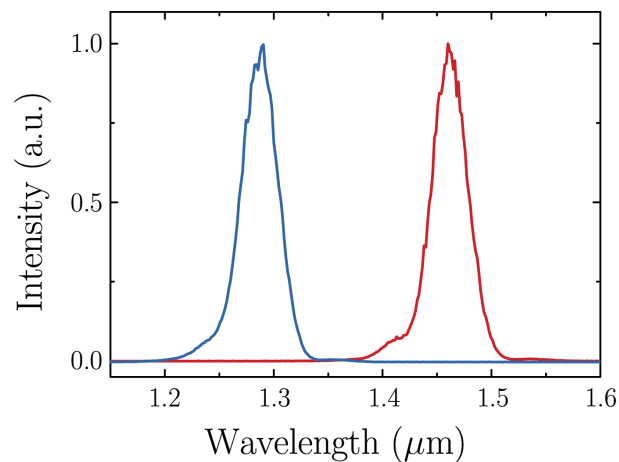

Figure A.2: Spectra of the output pulses of the OPAs used to generate the MIR pump pulses, tuned at 1.28 μm and 1.46 μm.

The collinear and collimated difference frequency generation (DFG) be-

tween the OPA outputs was performed in a 600 μm thick z-cut GaSe crystal. This delivered MIR pulses of 130 fs duration, 29 THz center frequency, and up to 10 mJ energy. These pulses were transmitted through a pair of KRS-5 broadband wire grid polarizers (used to vary their intensity) and focused at normal incidence onto the sample with a 150 mm effective focal length off-axis parabolic mirror. The beam diameter at the sample position, measured by its transmission through a calibrated pin-hole, was about 240 μm, yielding to a maximum fluence of 13 mJ/cm^2, corresponding to 8.7 MV/cm peak electric field.

A.3   MIR probe generation setup

The MIR probe pulses were generated by a setup conceptually similar to that employed for the pump ones, but pumped with 750 μJ energy. Because of the lower energy involved, the BBO crystals employed in the first OPAs stages were 1.5 mm thick, and those used for the second stages were 2.5 mm thick.

In the experiments reported on this thesis, these OPAs were tuned at 1.45 μm and 1.29 μm, generating 60 fs pulses with 31 μJ and 40 μJ energy, respectively. The DFG between the signal outputs produced MIR probe transients at 26.5 THz, with 100 fs duration and energy of 0.6 μJ. A typical MIR pulse generated by this setup is shown in Fig. 3.4 in the main body of this thesis. These pulses were then transmitted through a pair of free-standing gold wire grid polarizers (to reduce their intensity) and focused on the sample with an angle of 15 deg from normal incidence. The probe spot size on the sample, measured by its transmission through a calibrated pin-hole, was 170 μm.

A.4   Electro Optical Sampling

The characterization of the MIR pulses employed in this thesis was per-
formed by means of electro optical sampling, a technique that allows for
the direct measurement of their electric field profile in the time domain.
Because of the Pockels effect, the MIR electric field causes a rotation of the
polarization of a gate pulse which is propagating at the same speed inside a
nonlinear optical medium (in the experiments reported in this thesis GaSe
was used). Scanning the delay between the MIR and gate pulses and mea-
suring the gate polarization rotation therefore allows for the reconstruction
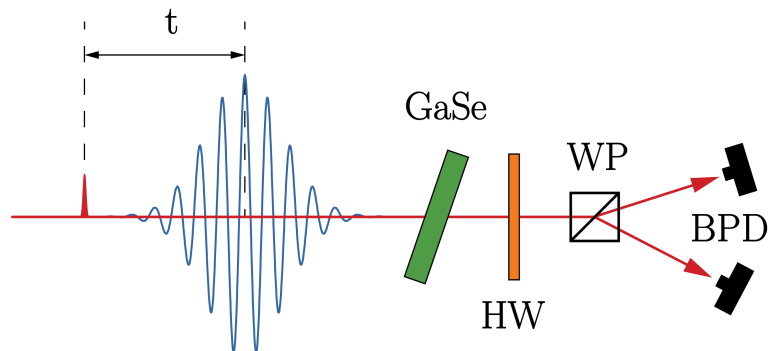of the MIR electric field.

Figure A.3: Schematic representation of the EOS pulse characterization
apparatus. GaSe: nonlinear optical medium; HW: half waveplate; WP:
Wollaston prism; BPD: Balanced photodiodes.

This is achieved by propagating the gate pulses through a $\lambda/2$ waveplate
and a Wollaston prism that spatially separates the two orthogonal polar-
ization components of the incoming radiation, as sketched in Fig. A.3. The
waveplate is aligned in such a way that in the absence of MIR radiation the
gate pulses are split in two equally intense parts hitting a pair of balanced
photodiodes. When the MIR is present, the gate pulses acquire a rotated

polarization and are split in different intensity parts, resulting in a photodiodes signal linearly proportional to the intensity of the MIR field. Because the EOS requires scanning the MIR-gate delay, it is not a single-shot pulse characterization method. This is the reason why the MIR pulses employed in time-domain spectroscopy need to be CEP stable, i.e. they must have a reproducible electric field profile.
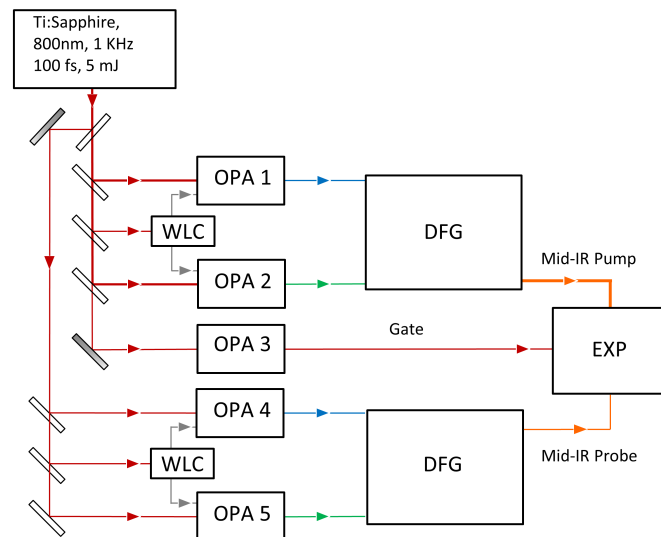
A.5 Setup overview

Figure A.4: Schematic overview of the complete setup used to generate the pump, probe and gate pulses and to perform the time-resolved nonlinear reflectivity measurements on silicon carbide. Optical parametric amplifiers (OPA), white light continuum generation (WLC), difference frequency generation (DFG), experiment (EXP).

Appendix B

Detailed implementation of FDTD

B.1   Implementation of 1D-FDTD

The basic update equations 4.15 and 4.16 for the electric and magnetic fields shown in section 4.1.2 allow for the propagation of electromagnetic waves in the simulation grid, and are the direct result of Maxwell's equations discretization. This means that if the fields are defined in all the grid positions at a given time, these equations propagate the fields at subsequent time steps. However, when the fields are inserted in the grid ath the beginning of the simulations, or when they reach the boundaries of the grid, things must be handled in a slightly different way. Furthermore, the properties of the materials in the grid can be analyzed by looking for example at their transmission or reflection coefficients, for which some detectors must be simulated in the grid. In this section these aspects of the FDTD method implementation [52, 53] will be briefly discussed.

B.1.1   Perfectly absorbing boundary conditions

When the fields propagate to the end of the grid, equations 4.15 and 4.16 fail. For example, at the first grid position $k = 1$, eq. 4.16 would generate an error, because the position $k - 1 = 0$ is not defined. Similarly, eq. 4.15 cannot handle the last position of the grid. For this reason, some additional boundary conditions must be introduced to deal with the grid edges. This is a general problem of FDTD (in particular in 2D and 3D), and can be tackled in different ways. In this thesis, perfectly absorbing boundary conditions, meaning that a field reaching the end of the grid is completely absorbed, were used. This is practically equivalent to having the field propagate further "outside the grid" without being reflected back. To achieve this, the values of the fields at the grid edges for the past two time loop iterations are stored in the memory. This allows the algorithm to know what the fields would be in two hypothetical cells outside the grid, therefore giving the proper input to the update equations. For this to be feasible, the grid boundaries must be linear, isotropic and non-dispersive materials, with the same refractive index. Furthermore, the time step must be chosen so that physical waves travel one cell in two time steps [46, 47] and this translates to

$$\Delta t = \frac{n_b \Delta z}{2c} \qquad\qquad (B.1)$$

where n_b is the refractive index at the grid edges. Note that this equation is compatible with the Courant-Friedrichs-Lewy stability condition of eq. 4.4. It is worth mentioning that due to some numerical truncation error, a very small amount of light is reflected by the grid boundaries. In the code presented here, the reflected light at the boundaries is 10^{-6} times smaller than the incident one, and for all practical purposes can be ignored.

B.1.2 Vacuum impedance

The absolute values of the electric and magnetic fields at any point in the grid are related by the *impedance* of the medium, which in vacuum is

$$\eta_0 = \frac{E}{H} = \sqrt{\frac{\mu_0}{\epsilon_0}} \approx 380\,\Omega. \tag{B.2}$$

Having more than two orders of magnitude difference between the fields is not advisable, since it can give rise to numerical truncation errors. This problem can be overcome by re-normalizing the magnetic field so that the magnitudes of E and H are the same. In the FDTD implementation used int his thesis the magnetic field has been replaced with

$$\vec{H}^* = \eta_0\,\vec{H}. \tag{B.3}$$

This re-normalization affects Maxwell's curl equations, which become

$$\nabla \times \vec{E} = -\frac{\mu_0}{\mathbf{c}}\,\frac{\partial \vec{H}^*}{\partial t} \tag{B.4}$$

$$\nabla \times \vec{H}^* = \frac{\epsilon_0}{\mathbf{c}}\,\frac{\partial \vec{E}}{\partial t} \tag{B.5}$$

leading to re-normalized coefficients in the update equations

$$H_x^*|_{t+\frac{\Delta t}{2}}^k = H_x^*|_{t-\frac{\Delta t}{2}}^k + \frac{\mathbf{c}\Delta t}{\mu_0 \Delta z}\left(E_y|_t^{k+1} - E_y|_t^k\right) \tag{B.6}$$

$$E_y|_{t+\Delta t}^k = E_y|_t^k + \frac{\mathbf{c}\Delta t}{\epsilon_0 \Delta z}\left(H_x^*|_{t+\frac{\Delta t}{2}}^k - H_x^*|_{t+\frac{\Delta t}{2}}^{k-1}\right). \tag{B.7}$$

This normalization has a purely numerical purpose, and does not affect in any way the physics of the problem since non-magnetic materials are considered, and all the resonances and nonlinearities are introduced in the electric field. For this reason in the rest of the thesis we referred to H^* as H.

B.1.3   Introduction of a unidirectional source

The electromagnetic waves are usually not present in the grid at the first time step of the simulations. Instead, they injected into the grid at later times, while the simulation is running. This is done by choosing one point in the grid to act as a source, in which the values of the fields are arbitrarily assigned as a function of time. Here, the fields are injected in the second grid position $k_{src} = 2$. The fields E_{src} and H_{src} are defined as a function of time t to be pulses with the desired frequencies and durations, and are then calculated as a function of the time loop index T through the relation $t = T \Delta t$. When defining E_{src} and H_{src}, particular care has to be taken because the source terms which are defined at staggered positions in space and time must be consistent with each other, i.e. they must describe the electric and magnetic field components of the same electromagnetic pulse. For example, if the electric field source is defined as

$$E_y^{src}\big|_t^{k_{src}} = g(t) \tag{B.8}$$

the magnetic fields source has to be defined as

$$H_x^{src}\big|_{t+\frac{\Delta t}{2}}^{k_{src}-1} = -\sqrt{\frac{\epsilon_r^{src}}{\mu_r^{src}}}\, g\left(t + \frac{n_{src}\Delta z}{2c} + \frac{\Delta t}{2}\right). \tag{B.9}$$

where n_{src} is the refractive index at k_{src}. In the E_y/H_x mode, the electric and magnetic fields have opposite signs, and their ratio depends on the permittivity ϵ_r^{src} and permeability μ_r^{src} of the medium at the source position. Furthermore, in order for the fields to be defined at proper relative times and grid positions, two terms must be added in the parenthesis of eq. B.9. The first term *shifts* the magnetic field in time by the amount light takes to travel from one grid position to the next, and the second *shifts* it to take into account that they are defined at different times in the Yee grid.

When the source is injected in the simulation, oscillating electric and magnetic fields are externally imposed at k_{src}. According to Maxwell's equations such fields start propagating both in the positive and negative z directions. To make the source directional and reproduce a real light source, the update equation for the cells k_{src} and $k_{src} - 1$ must be modified to subtract at each time step the back propagating light from the previous step [46].

B.1.4 Reflected and transmitted fields detection

The optical properties of the materials simulated in the grid can be evaluated starting from the reflection and transmission coefficients, which are calculated as the ratio between the reflected or transmitted and incident light field. While the incident light field is known as it is arbitrarily defined and injected in the grid by the user, the unknown reflected and transmitted fields are results of the simulations. For these fields to be recorded, some detectors must be introduced in the grid. In the code presented here, the detector for the reflected field is positioned at the first grid position $k = 1$, while the detector for the transmitted field is positioned at the last grid position. The values of the electric field at these positions is saved in the memory as the simulation loops through the time steps T, and is then expressed as a function of $t = T\Delta t$. Since the source introduced in our simulations is unidirectional as discussed in section B.1.3, the light reaching the detector at $k = 1$ is only due to the reflection form the materials present in the grid, and not to the source. This is the reason why the source is positioned at the second grid cell and not at the first.

B.2   Complete FDTD loop for resonant materials

The update equations described in section 4.1.3 must be solved together with Maxwell's curl equations in the time loop to simulate the propagation of electromagnetic waves in materials with resonances.

The coefficients multiplying the physical quantities in the update equations have constant values throughout the time loop iterations, and are therefore calculated only once to reduce the computation time. Such coefficients are defined as

$$
mE_{y\_}H_x|^k = \frac{c\Delta t}{\mu|^k \Delta z} \qquad \text{see footnote}[1]
$$

$$
mJ\_J|^k = \frac{2 - \Gamma|^k \Delta t}{2 + \Gamma|^k \Delta t}
$$

$$
mQ\_J|^k = \frac{2\,\Omega_{TO}^2|^k \Delta t}{2 + \Gamma|^k \Delta t}
$$

$$
mE_{y\_}J|^k = \frac{2\,\Omega_{TO}|^k \sqrt{\epsilon_0 \left(\varepsilon_0|^k - \varepsilon_\infty|^k\right)}\,\Delta t}{2 + \Gamma|^k \Delta t} \tag{B.10}
$$

$$
mH_{x\_}D_y|^k = \sqrt{\frac{\epsilon_0}{\mu_0}}\,\frac{\Delta t}{\Delta z}
$$

$$
mD_{y\_}E_y|^k = \frac{1}{\epsilon_0\,\varepsilon_\infty|^k}
$$

$$
mQ\_E_y|^k = \frac{\Omega_{TO}|^k \sqrt{\epsilon_0 \left(\varepsilon_0|^k - \varepsilon_\infty|^k\right)}}{\epsilon_0\,\varepsilon_\infty|^k}.
$$

The coefficients labeled with the spatial index k because while being constant in time, they have different values depending on the properties of the

---

[1]According to eq. 4.18, c should not be in this coefficient. It is present here because of the magnetic field re-normalization due to the vacuum impedance mentioned in section B.1.2. The same applies for the square root in $mH_{x\_}D_y|^k$.

materials simulated at various positions in the grid. The complete set of equations for the FDTD loop therefore becomes

$$\mathbf{H_x}|^{\mathbf{k}} = \mathbf{H_x}|^{\mathbf{k}} + mE_y\_H_x|^k \cdot \left(\mathbf{E_y}|^{\mathbf{k+1}} - \mathbf{E_y}|^{\mathbf{k}} \right)$$

$$\mathbf{J}|^{\mathbf{k}} = mJ\_J|^k \cdot \mathbf{J}|^{\mathbf{k}} - mQ\_J|^k \cdot \mathbf{Q}|^{\mathbf{k}} + mE_y\_J|^k \cdot \mathbf{E_y}|^{\mathbf{k}}$$

$$\mathbf{Q}|^{\mathbf{k}} = \mathbf{Q}|^{\mathbf{k}} + \Delta t \cdot \mathbf{J}|^{\mathbf{k}} \qquad \text{(B.11)}$$

$$\mathbf{D_y}|^{\mathbf{k}} = \mathbf{D_y}|^{\mathbf{k}} + mH_x\_D_y|^k \cdot \left(\mathbf{H_x}|^{\mathbf{k}} - \mathbf{H_x}|^{\mathbf{k-1}} \right)$$

$$\mathbf{E_y}|^{\mathbf{k}} = mD_y\_E_y|^k \cdot \mathbf{D_y}|^{\mathbf{k}} - mQ\_E_y|^k \cdot \mathbf{Q}|^{\mathbf{k}}$$

where the physical quantities have been highlighted in bold to separate them from the update coefficients. It should be noted that the time index disappeared from the update equations B.11, and this is due to the fact that the time index T is the one on which the loop is cycling. In equation 4.28, the left hand side is time indexed with $t + \frac{\Delta t}{2}$ which corresponds for example to time step T, and the terms on the right hand side are indexed with t and $t - \frac{\Delta t}{2}$ which both correspond to the time step $T - 1$ thanks to the time grid staggering. This applies to all the update equations (except for the last one which does not include any time derivative), and when they are looped all the physical quantities are advanced one step in time leading to the proper light propagation.

In the grid positions where there is vacuum, $\Omega_{TO} = \Gamma = 0$ and $\varepsilon_0 = \varepsilon_\infty = 1$, reducing the update equations B.11 to those for the propagation in linear materials. To introduce a dielectric with a phonon in the grid, it is sufficient to define the values of Ω_{TO}, Γ, ε_0 and ε_∞ for the cells in which such material is placed. As mentioned in section 4.1.1, no further boundary conditions are required for the interfaces between materials.

B.3   Complex linear optical properties of SiC

The linear reflectivity R of SiC simulated with the code presented in this thesis is described in section 4.2 of the thesis main body. In this appendix section the simulated complex optical properties of SiC are shown, and compared to those calculated analytically using the same oscillator parameters input in the simulations.

B.3.1   Refractive index

The refractive index as a function of frequency can be calculated from the reflection coefficient $r(\omega)$ through the relation

$$\tilde{n}(\omega) = \frac{1 - r(\omega)}{1 + r(\omega)} \tag{B.12}$$

and the real and imaginary parts n and k resulting from the FDTD simulation can be compared to the analytical ones, as shown in Fig. B.1.

The agreement between the simulated and analytical quantities is fairly good, and the behaviors are properly reproduced throughout the interesting spectral region. Some quantitative discrepancy appears in both n and k around Ω_{TO}, and this is probably due to numerical approximation becoming detrimental when the quantities tend to diverge. The fact that the reflectivity, which depends only on the square modulus of $r(\omega)$ is properly simulated in the entire frequency region, suggests that the mismatch should be ascribed to some phase effect. In fact, when shifting the time axis of $E_{inc,r}$ to calculate $r(\omega)$, the numerical grid is assumed to be dispersionless, which is just an approximation. Some numerical dispersion is actually present in the FDTD algorithm, and this is probably causing a small additional phase-shift in E_{ref}, which is not taken into account in $E_{inc,r}$. Some
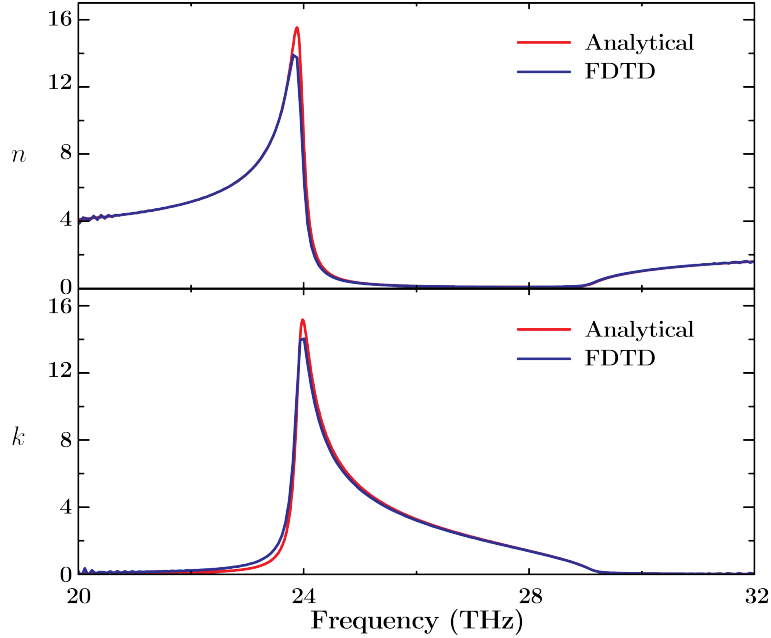
Figure B.1: Frequency dependent real (n) and imaginary (k) parts of the complex refractive index calculated from the results of the FDTD simulation (blue) compared to those calculated analytically from the Lorentz model (red). The material parameters used for the plots are those of hexagonal silicon carbide, with $\varepsilon_0 = 9.66$, $\varepsilon_\infty = 6.52$, $\Omega_{TO} = 24.9$ THz and $\Gamma = 0.2$ THz.

modifications to the FDTD algorithm allowing for the grid dispersion compensation have been developed. These corrections are only working for one specific frequency, and therefore not ideal for very broad pulses. However, a grid dispersion compensation designed for Ω_{TO} might still improve the reconstruction of the complex optical properties, and could be implemented in future iterations of these simulations. Another possibility to overcome these problems would be to run pairs of simulations, replacing the dielectric with a perfect electric conductor in the second ones, and then compare the two reflected fields. In this case the grid dispersion should affect both fields in the same way, therefore allowing for a better reconstruction of n and k.

The drawback of this solution is that the computational time required to calculate the optical properties would basically double.

B.3.2   Relative permittivity

The real and imaginary parts of the relative permittivity ϵ_r can also be calculated from the FDTD simulation through the relations of eq. 1.28 and 1.29, and are compared to the analytical curves in Fig. B.2.
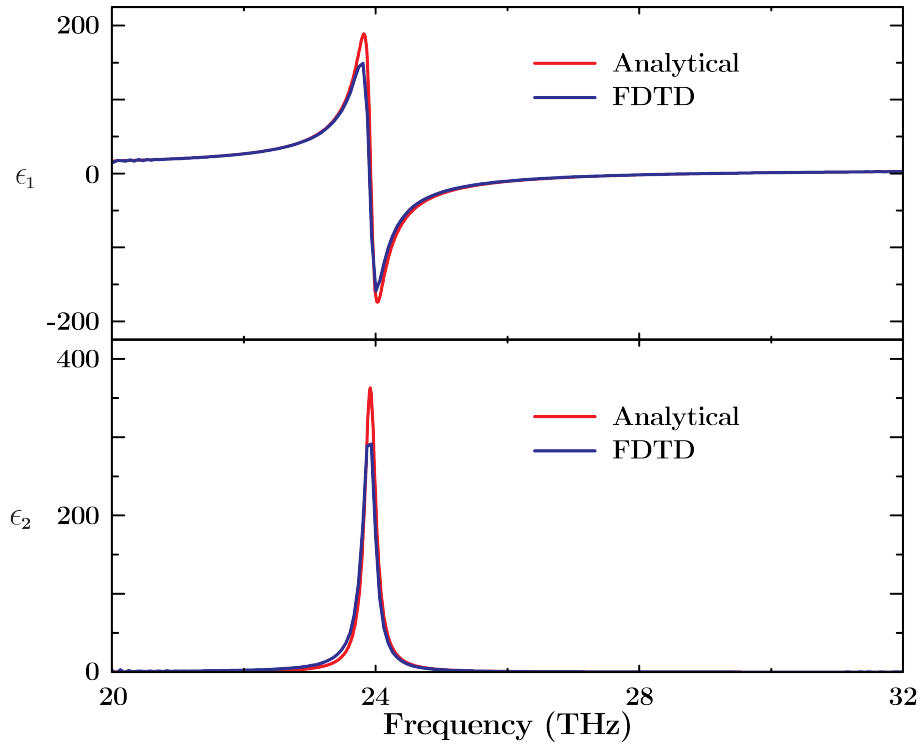

Figure B.2: Frequency dependent real (ϵ_1) and imaginary (ϵ_2) parts of the relative permittivity calculated from the results of the FDTD simulation (blue) compared to those calculated analytically from the Lorentz model (red). The material parameters used for the plots are those of hexagonal silicon carbide, with $\varepsilon_0 = 9.66$, $\varepsilon_\infty = 6.52$, $\Omega_{TO} = 24.9$ THz and $\Gamma = 0.2$ THz.

Similarly to n and k, ϵ_1 and ϵ_2 calculated from FDTD are affected by the

grid dispersion, and show a small quantitative mismatch with the analytical ones in the proximity of Ω_{TO}.

B.4   Complete nonlinear FDTD loop

This section describes the updated version the FDTD loop of section B.2, including the nonlinear expansions described in section 4.3. It is important to notice that eq. 4.35 contains the $+2\beta Q^2$ term in all the denominators. For this reason, the fractions on the right hand side of the equation are not coefficients remaining constant throughout all the FDTD loop iterations, and cannot be calculated only once in the simulations like in eq. 4.29. Instead, eq. 4.35 has to be inserted in the FDTD loop as it is, so that the value of $+2\beta Q^2$ can be updated for every grid position k at every time t.

In equation 4.41 instead, the α and β terms in the square brackets are constant throughout the simulation, and can be calculate only once to save computation time, as shown in section B.2 for the linear update coefficients. The new update coefficients are defined as:

$$
\begin{aligned}
mQ2E\_J|^k &= \frac{6\,\alpha|^k\,\Delta t}{2+\Gamma|^k\,\Delta t} \\
mQE2\_J|^k &= \frac{4\,\beta|^k\,\Delta t}{2+\Gamma|^k\,\Delta t}
\end{aligned}
\tag{B.13}
$$

and are equal to zero outside the sample, i.e. for values of k where $\alpha|^k$ and $\beta|^k$ are zero.

The complete set of equations for the nonlinear FDTD loop, including eq. 4.35 and eq. 4.41, and with the explicit dependence of all the parameters on the k grid position becomes:

$$\mathbf{H_x}|^{\mathbf{k}} = \mathbf{H_x}|^{\mathbf{k}} + mE_{y\_}H_x|^k \cdot \left(\mathbf{E_y}|^{\mathbf{k+1}} - \mathbf{E_y}|^{\mathbf{k}} \right)$$

$$\mathbf{J}|^{\mathbf{k}} = mJ\_J|^k \cdot \mathbf{J}|^{\mathbf{k}} - mQ\_J|^k \cdot \mathbf{Q}|^{\mathbf{k}} + mE_{y\_}J|^k \cdot \mathbf{E_y}|^{\mathbf{k}} +$$

$$+ mQ2E\_J|^k \cdot \left(\mathbf{Q}|^{\mathbf{k}} \right)^2 \cdot \mathbf{E_y}|^{\mathbf{k}} +$$

$$+ mQE2\_J|^k \cdot \mathbf{Q}|^{\mathbf{k}} \cdot \left(\mathbf{E_y}|^{\mathbf{k}} \right)^2$$

$$\mathbf{Q}|^{\mathbf{k}} = \mathbf{Q}|^{\mathbf{k}} + \Delta t \cdot \mathbf{J}|^{\mathbf{k}}$$

$$\mathbf{D_y}|^{\mathbf{k}} = \mathbf{D_y}|^{\mathbf{k}} + mH_{x\_}D_y|^k \cdot \left(\mathbf{H_x}|^{\mathbf{k}} - \mathbf{H_x}|^{\mathbf{k-1}} \right) \qquad (B.14)$$

$$\mathbf{E_y}|^{\mathbf{k}} = \frac{1}{\epsilon_0\ \varepsilon_\infty|^k + 2\ \beta|^k \cdot \left(\mathbf{Q}|^{\mathbf{k}} \right)^2} \cdot \mathbf{D_y}|^{\mathbf{k}} -$$

$$- \frac{\Omega_{TO}|^k \sqrt{\epsilon_0 \left(\varepsilon_0|^k - \varepsilon_\infty|^k \right)}}{\epsilon_0\ \varepsilon_\infty|^k + 2\ \beta|^k \cdot \left(\mathbf{Q}|^{\mathbf{k}} \right)^2} \cdot \mathbf{Q}|^{\mathbf{k}} -$$

$$- \frac{\alpha|^k}{\epsilon_0\ \varepsilon_\infty|^k + 2\ \beta|^k \cdot \left(\mathbf{Q}|^{\mathbf{k}} \right)^2} \cdot \left(\mathbf{Q}|^{\mathbf{k}} \right)^3$$

where the physical quantities have been highlighted in bold to separate them from the constant coefficients. If the material has a linear response, i.e. if $\alpha = 0$ and $\beta = 0$, the coefficients $mQ2E\_J|^k$ and $mQE2\_J|^k$ are equal to zero, and the update equation for $\mathbf{J}|^{\mathbf{k}}$ simplifies to that reported in eq. B.11. The same applies to the update equation for $\mathbf{E_y}|^{\mathbf{k}}$, since the last term vanishes and the β-correction terms in the denominators also vanish. This updated version of the FDTD loop can therefore be used for both linear and nonlinear phonon-light interactions, depending on the values of the input parameters. The extensive use of this loop for linear materials is anyway not advisable, since it requires more memory and more computing time. The higher memory consumption is allocated to the *empty* $\alpha|^k$, $\beta|^k$, $mQ2E\_J|^k$ and $mQE2\_J|^k$ vectors, while higher computation time is required because

of the update equation for $\mathbf{E_y}|^{\mathbf{k}}$ in which the values of the update coefficients are calculated at each time iteration of the loop, albeit being constant.

B.5   Linearity of the probe

One of the general assumption at the basis of the pump-probe technique is that the probe pulse is weak enough not to drive the system in a nonlinear regime, being instead just a way to investigate the status of the sample. This needs to be tested for the simulation scheme presented here.
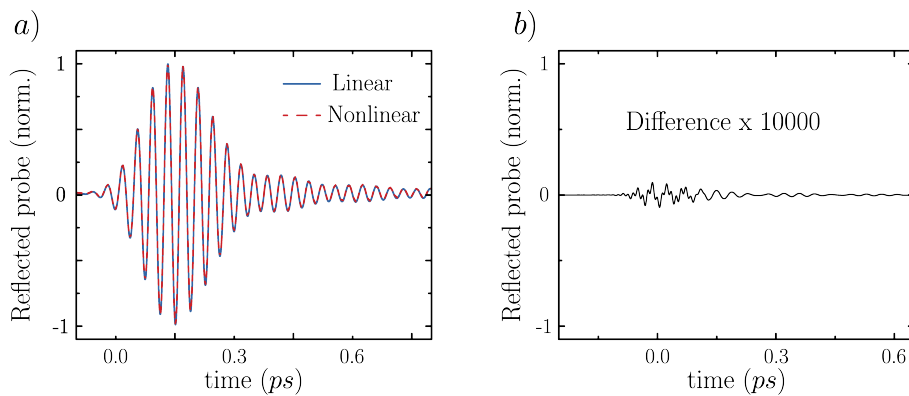

Figure B.3: (a) Light pulse with 86.8 kV/cm peak electric field reflected from a sample with the linear (solid blue) and non-linear (dashed red) light-phonon interaction models. (b) Difference between the two curves of panel a, multiplied by four orders of magnitude. .

Such important test can be carried out comparing the probe electric field reflected by the sample considering both a linear and a nonlinear light-phonon interaction model. If the two results are the same, for the given values of the sample nonlinearities, the probe field is proven weak enough not to drive the phonon coordinate Q or the polarization P in the nonlinear regime, and the assumption behind equation 4.42 is correct. Figure B.3a shows the simulated probe electric fields reflected from the sample considering both a linear

(solid blue) as well as non-linear (dashed red) light-phonon interaction. The impinging peak electric field for both the curves was 86.8 kV/cm, but in the linear case the α and β coefficients described in section 4.3 were set to zero, while in the nonlinear case the values required to reproduce the SiC nonlinear optical properties were used. The difference between the curves in Fig. B.3a is reported in Fig. B.3b (please note that it is multiplied by 10^4). Such difference is of order 10^{-5}, and can be ignored for all practical purposes.

Appendix C

Mid-infrared pulse shaper

In this thesis, coherent femtosecond MIR pulses were used to drive the Si-C stretching mode of SiC to large amplitudes and unveil its nonlinear response. To do this, the employed pump pulses had peak electric fields of up to 9 MV/cm, achieved by generating pulses of order 10 mJ energy and a duration of about 130 fs. These pulses were close to the transform limit, i.e. their temporal duration was close to the shortest obtainable given their bandwidth, granting the highest possible peak fields.

However, in the more general context of the phonon dynamics manipulation with light, pulses with a controllable temporal electric field profiles rather than high peak fields might prove as a powerful tool. Moreover, these pulses could be employed in different contexts like small molecule photochemistry and vibrational ladder climbing [54, 55].

This appendix reports on the realization of a pulse shaper capable of manipulating the temporal shape of MIR pulses in the 10 to 20 μm wavelength range by means of a deformable mirror[1].

---

[1]This appendix is based on the results of the published paper "Pulse shaping in the mid-infrared by a deformable mirror" by A. Cartella *et al* [56]. The author contributed

The manipulation of the temporal shape of an ultrashort pulse is achieved by controlling the amplitude and phase of its electric field in the frequency domain. This is usually done manipulating the individual frequency components in the Fourier plane of a $4f$ zero-dispersion pulse shaper. Successful control of the pulse shape in the visible and near-infrared spectral regions [57] was achieved in the past by means of acousto-optic modulators (AOMs) or Liquid Crystal Spatial Light Modulators (LC-SLMs).

Phase and amplitude manipulation is not straightforward in the MIR because LC-SLMs do not transmit wavelengths longer than 1.6 μm. Complex pulse shaping is instead possible with Germanium(Ge)-based AOMs, although Ge begins to absorb at 12 μm [58].

Because MIR pulses are usually generated by difference frequency generation (DFG) between two near-infrared (NIR) beams, the absorption problem can be overcome by shaping the NIR pulses and then transferring the phase modulation to the MIR through the DFG process [59, 60, 61, 62]. However, this technique is rather indirect, and the efficiency of the DFG is strongly influenced by the desired pulse shape.

The direct manipulation of the MIR pulse is generally advisable, albeit more challenging, and calls for the development of modulators capable of handling long wavelengths. A first attempt in this direction was shown by placing patterned masks at the Fourier plane of a $4f$ pulse shaper [63], allowing for the control of the spectral amplitude alone.

On the other hand, phase-only modulations can be introduced by deformable mirrors (DMs) placed in the Fourier plane of a reflection-based $4f$ setup [64, 65, 66]. DMs show high throughput and are substantially achro-

_____

matic, allowing to extend the spectral coverage to the MIR, limited only by the reflectivity of the metallic coating. However, phase shifts ϕ as high as 5-10 optical cycles are typically required for successfully shaping ultrashort laser pulses. In the 10 to 20 μm wavelength region, this corresponds to a very large mirror deformation, because a phase shift at a component λ requires a mirror deformation $\Delta z = \lambda \cdot \phi/4\pi$.

The pulse shaper presented here is based on a DM designed to handle the high deformations required by the MIR wavelengths. The DM consists of a rectangular (10mm $\times$ 90mm) gold coated silicon substrate which can be bent by a series of 32 piezo-electric actuators. Both concave and convex curvatures are achieved, depending on the polarity of the voltage applied to the actuators that locally distort the mirror surface. This DM introduces continuous and smooth phase modulation, which are software controlled and applied in less than one second. The simultaneous actuation of all the piezoelectric elements with the maximum allowed voltage induces a movement of the mirror center of 220 μm ($+/-$ 110 μm from the flat position). Because the actuators are controlled in 256 steps, the minimum applicable deformation is about one micrometer, limiting the employment of this device to wavelengths larger than 10 μm.

The scheme of the pulse shaper is sketched in Fig.C.1. A diffraction grating (40 lines/mm, blazed at 15 μm) disperses the different spectral components, which are then collected by a spherical mirror with 50 cm focal length. Each wavelength is then mapped on one precise spatial coordinate of the deformable mirror and reflected back to the spherical mirror at a slightly lower position. All the spectral components are then combined together by a second bounce on the grating and are picked up by a flat mirror. The design with the DM on top of the grating and the focal length
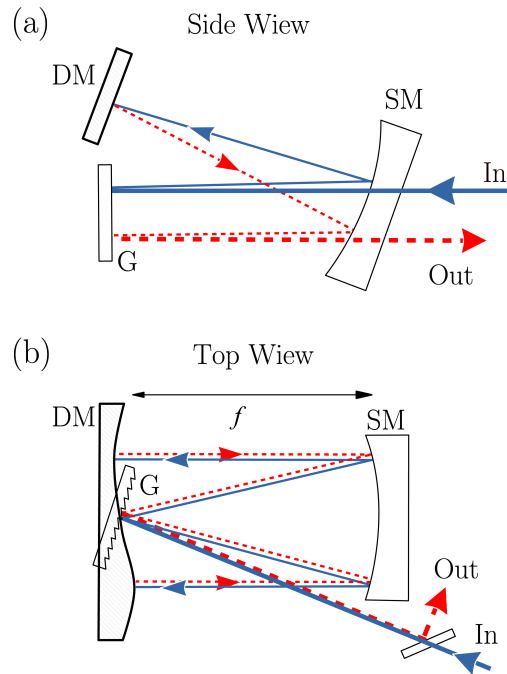
Figure C.1: Side (a) and top (b) view of the pulse shaper: DM, deformable mirror; SM, spherical mirror; G, grating.

of the spherical mirror were carefully chosen to minimize aberrations. The overall throughput of the shaper, including the DM, the other mirrors and the grating, is close to 50%.

The capabilities of this pulse shaper were demonstrated with CEP stable MIR pulses [51, 43] generated by DFG between two NIR pulses from optical parametric amplifiers (OPAs) at 1kHz repetition rate seeded by the same white light continuum. This configuration is similar to that used for the experiments on SiC presented in this thesis. However, the MIR could be gated in the EOS directly employing the pulses from the Ti:sapphire laser amplifier, that in this case had a 30 fs duration. The system could generate MIR pulses tunable up to 20 μm (*i.e.* down to 15 THz) [67].

Figure C.2(a) displays a Wigner distribution map [68] of a typical 19-

Mid-infrared pulse shaper
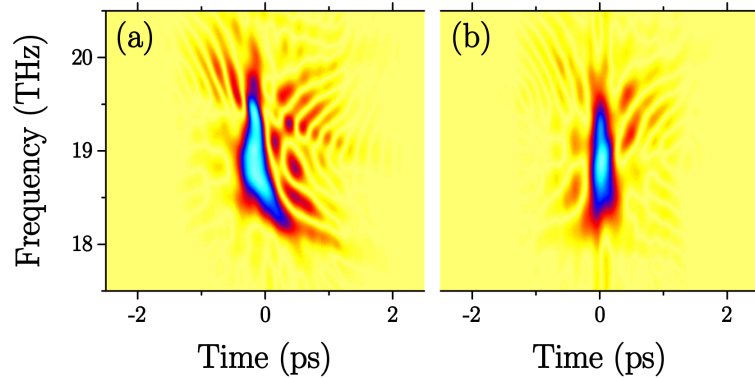Mid-infrared pulse shaper
119

Figure C.2: Wigner maps of (a) a typical MIR pulse measured with the deformable mirror set to flat, i.e. unaffected by the shaper and (b) after a single iteration of phase compensation.

THz MIR pulse transmitted through the shaper. With the deformable mirror set to flat, this pulse was nominally unaffected by the shaper. The pulse duration was 417 fs, and the bandwidth 2 THz (FWHM). From this measurement, the spectral phase of the pulse was retrieved, and the mirror deformation required to compensate for it was calculated. This deformation then defined the required electrode voltages that were imparted to the electrodes. The result of a single iteration of this procedure is shown in Fig. C.2(b), where the pulse duration was reduced to 389 fs.

The capabilities of the shaper to impart a desired spectral phase to the MIR pulses was tested next. A parabolic phase corresponding to a group delay dispersion (GDD) of $+0.2 ps^2$ and therefore to a linear group delay was introduced first. The Wigner map deduced from the EOS of the shaped pulse is shown in Fig. C.3(a). The solid line represents the target group delay, in very good agreement with the measurement. The shaper capability of applying both positive and negative GDDs is demonstrated in C.3(b), where the measured spectral phases (open symbols) are shown to be in good agreement with the corresponding target dispersions (solid lines).
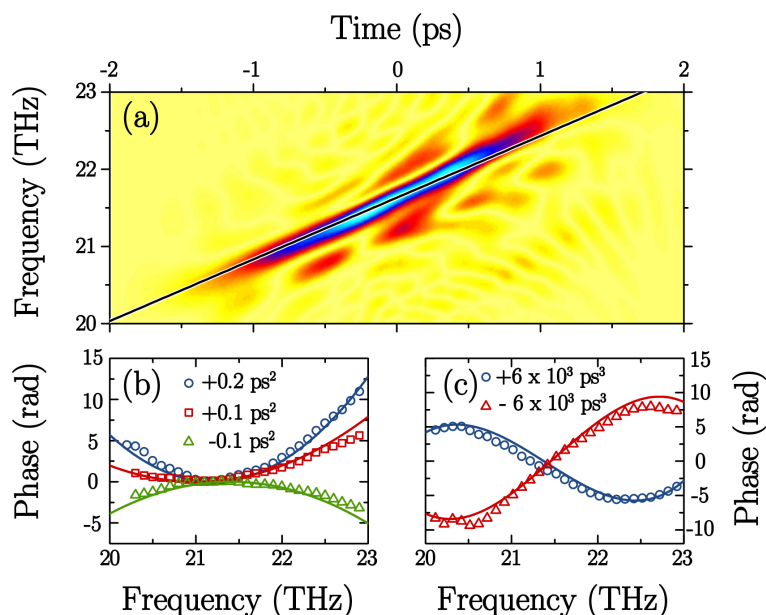
Figure C.3: (a) Wigner map of a measured pulse where a quadratic spectral phase with $GDD = +0.2ps^2$ was applied. (b) Measured spectral phases of pulses with +0.2 ps^2 (blue circles), +0.1 ps^2 (red squares) and -0.1 ps^2 (green triangles) GDDs. (c) Characterization of +6 × 10^{-3} ps^3 (blu circles) and -6 × 10^{-3} ps^3 (red triangles) TODs. The solid lines represent the target spectral phases.

Third order dispersion (TOD) were also properly imparted, as shown in Fig. C.3(c). Again, the solid lines represent the target spectral phases, demonstrating the excellent capability of this shaper to introduce specified spectral phases in a single iteration.

Finally, sub-pulses with different spectral content were generated with the shaper, splitting the starting pulses. This was obtained applying a V-shaped spectral phase, i.e. different linear phases to two portions of the staring pulse spectrum. This resulted in two different group delays imparted to the two wings of the spectrum, and therefore in the generation of two sub-pulses. The time delay between the sub-pulses could be tuned by varying
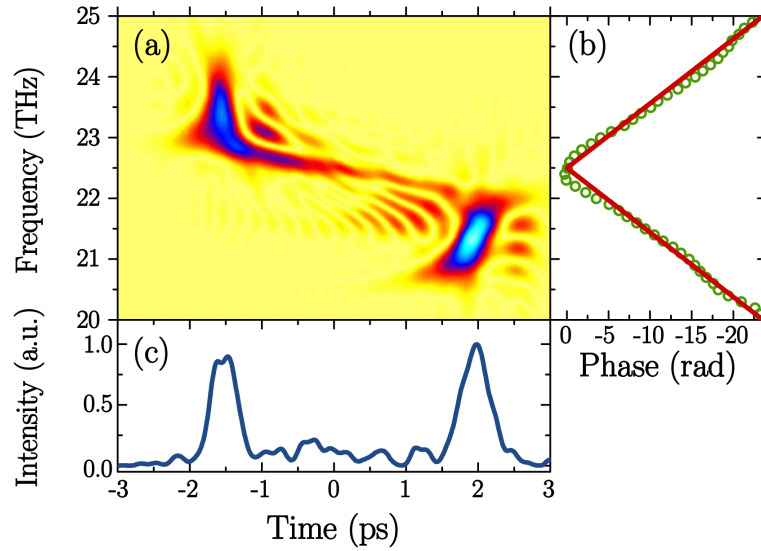
Figure C.4: (a) Wigner map of a double pulse. (b) Target (solid red) compared with measured (green circles) spectral phase. (c) Double pulse intensity profile in the time domain.

the slope of the two arms. The Wigner map of a double pulse obtained in this way is shown in Fig. C.4(a). The measured spectral phase is shown in panel (b), matching very well the target. The temporal spacing between the two pulses associated with the given slope is expected to be 3.5 ps. The measured delay, reported in panel (c), where the intensity profile of the two pulses is displayed, shows a very good agreement with the target value.

Appendix D

Narrowband mid-IR generation

Optical pulses in the 6 to 20 μm wavelength range are a powerful tool to control solids and molecular systems functionalities [69, 27], for example by driving lattice vibrations to large amplitudes [24, 23] like in the experiments reported in the main part of this thesis.

Tunable MIR pulses at these frequencies are usually obtained by difference frequency generation (DFG) between two femtosecond near-infrared (NIR) pulses [67, 63], and have bandwidths of 10 to 30 % $\Delta\omega/\omega_0$. These bandwidths are much larger than the linewidths of vibrational modes in condensed matter, which are often of the order of a few percent only. The pulses broad bandwidths are therefore a limiting factor for the spectral selectivity of the photoexcitation.

This appendix reports on the generation of narrowband (down to less than 2% $\Delta\omega/\omega_0$) MIR carrier envelope phase (CEP) stable pulses in the 10 to 15 μm wavelength range[1].

---

[1]This appendix is based on the results of the published paper "Narrowband carrier-envelope phase stable mid-infrared pulses at wavelengths beyond 10 μm by chirped-pulse difference frequency generation" by A. Cartella *et al* [70]. The author contributed to

The most straightforward method to reduce the bandwidth either of the interacting NIR pulses or of the resulting MIR light consists in linear spectral filtering by bandpass filters or by slits placed in the Fourier plane of a zero-dispersion pulse shaper [71]. This approach is however intrinsically inefficient because the pulse energy lost is proportional to the achieved spectral narrowing.

A more efficient approach for the generation of narrowband pulses is based on the nonlinear interaction between suitably chirped broadband pulses. This has been successfully applied in the visible, where narrowband pulses have been obtained via sum frequency generation of broadband NIR pulses with opposite chirp [72]. Analogously, the DFG between NIR pulses having chirp with the same sign was used to generate narrowband MIR pulses with wavelengths shorter than 10 μm [73, 74, 75].

The principle of narrowband MIR generation through DFG between chirped pulses is shown in Fig. D.1. The time-frequency Wigner maps [68] of the interacting NIR pulses are shown in panels (a) to (c), with the MIR light generated at the difference frequency (DF) between frequency components interacting at the same time in the nonlinear medium. To leading order, the difference between the closest/farthest interacting frequency components $\Omega_{1/2}$ allow to estimate the bandwidth of the MIR pulses as $\Delta\Omega = \Omega_2 - \Omega_1$. If the two NIR pulses are transform limited (TL), like in Fig. D.1a, all their spectral components interact simultaneously resulting in the broadest MIR pulse (red line in Fig. D.1d). If the two NIR pulses are linearly chirped with different group delay dispersion (GDD), as depicted in Fig. D.1b, only a subset of their frequency components can interact, leading to

---

the publication by performing the measurements, analyzing the data and writing the manuscript, with help from all co-authors
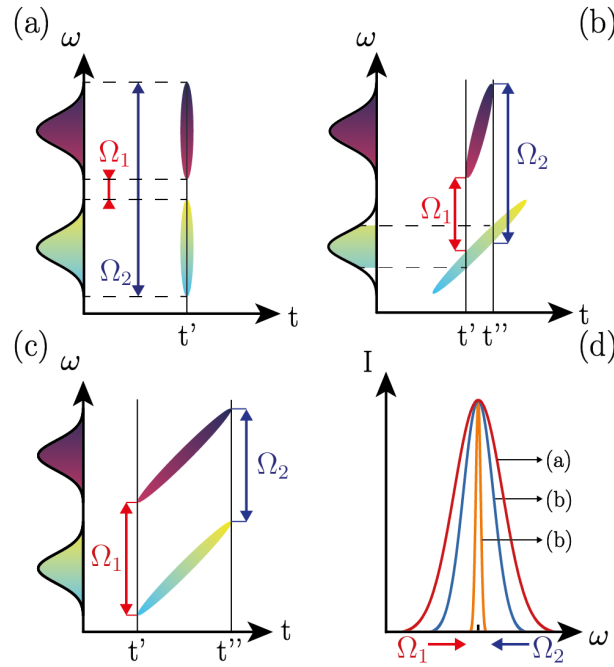
Figure D.1: Principle of the narrowband MIR pulse generation: (a)-(c) Time-frequency maps of the interacting NIR pulses, for various chirp configurations: MIR components are generated at the DF between NIR spectral frequencies at the same time delay. Ω_1 and Ω_2 are the lowest and highest MIR frequencies, respectively. (d) Corresponding MIR spectra. When going from the configuration (a) to (c), Ω_1 and Ω_2 get closer to each other, resulting in a narrower MIR spectrum.

a decrease in the MIR bandwidth (blue line in Fig. D.1d). Finally, if the two NIR pulses are chirped with exactly the same amount of GDD like in Fig. D.1c, the spectral components involved in the DFG process are all at the same distance, and $\Delta\Omega = \Omega_2 - \Omega_1 \approx 0$ is minimized, with the generated MIR pulses ideally quasi-monochromatic. However, because a cut at any time t' of the NIR pulses time-frequency maps has a finite bandwidth, the MIR spectrum is inevitably broadened. An estimation of the of the MIR bandwidth is obtained recalling that the its time duration cannot be bigger

	$\lambda_I = 1.31\mu m$		$\lambda_{II} = 1.46\mu m$		
Material	$\mathrm{GDD}_I/\mathrm{L}$ $\mathrm{fs}^2/\mathrm{cm}$	$\mathrm{TOD}_I/\mathrm{L}$ $\mathrm{fs}^3/\mathrm{cm}$	$\mathrm{GDD}_{II}/\mathrm{L}$ $\mathrm{fs}^2/\mathrm{cm}$	$\mathrm{TOD}_{II}/\mathrm{L}$ $\mathrm{fs}^3/\mathrm{cm}$	$\mathrm{TOD}_I/$ TOD_{II}
ZnSe	4741	4277	4131	3992	0.93
CdTe	10530	11500	8938	10080	0.96
Si	16865	60530	12330	17320	2.55

Table D.1: Dispersion at the pump λ_I and signal λ_{II} wavelengths introduced by propagation in 1 cm of highly dispersive materials. The last column is the ratio between TOD_I and TOD_{II} at plates thicknesses where $\mathrm{GDD}_I = \mathrm{GDD}_{II}$. The dispersion was calculated with Sellmeier coefficients from [76, 77, 78].

than those of the generating pulses. Thus, fixing a desired $\Delta\omega$ corresponds to choosing the MIR pulse duration, and therefore the NIR stretching.

Here, the extension of this approach to wavelengths larger than 10 μm is reported. The narrowband MIR pulses were generated with the same experimental setup used in the main part of this thesis to generate the pump pulses for the SiC experiment. The OPAs were tuned at $\lambda_I = 1.31$ μm ($\simeq$ 229 THz) and $\lambda_{II} = 1.46$ ($\simeq$ 205 THz) μm, targeting a MIR wavelength of 12.5 μm (24 THz).

The NIR pulses were stretched by propagating them in highly dispersive materials, that could be easily inserted or removed in the optical path to switch between broadband and narrowband MIR generation.

The material taken under consideration as NIR stretchers were zinc selenide (ZnSe), cadmium telluride (CdTe) and silicon (Si). The required optical properties were transparency and high dispersion in the NIR, and high bandgap to reduce two-photon absorption processes.
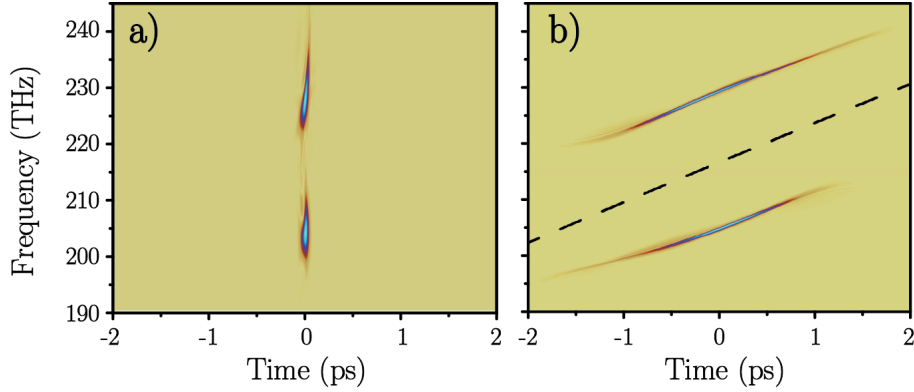
Figure D.2: Experimental time-frequency Wigner maps of the NIR OPA pulses, retrieved from the measured SHG-FROG. (a) Pulses as generated (close to the TL). (b) Pulses chirped by one ZnSe plate in each optical path. Dashed line: the target spectral chirp with GDD = 22500 fs^2 and TOD = 20000 fs^3.

The dispersion properties of the aforementioned materials are reported in Tab. D.1. The minimum possible MIR bandwidth is achieved by introducing the same dispersion in the two NIR beams. For any of these materials, rods of different thicknesses L_I and L_{II} are required to obtain the same GDD at λ_I and λ_{II} . Once L_I and L_{II} are set, the material with the optimum dispersion properties is the one for which TOD_I and TOD_{II} are closest to each other, making TOD_I/TOD_{II} a good figure of merit. Table D.1 then shows that Si is by far the worst of the listed materials, while CdTe and ZnSe have very similar performances. However, ZnSe was chosen because of its bandgap of 2.8 eV, much bigger than that of CdTe (1.5 eV) that would be detrimental due to two-photon absorption. ZnSe rods of L_I = 4.7 cm and L_{II} = 5.2cm thickness were used to obtain GDD of about 22500 fs^2, which chirps the 60 fs NIR pulses to approximately 1 ps. The amount of dispersion could be easily doubled to GDD = 45000 fs^2 by introducing two ZnSe rods into each NIR beam.
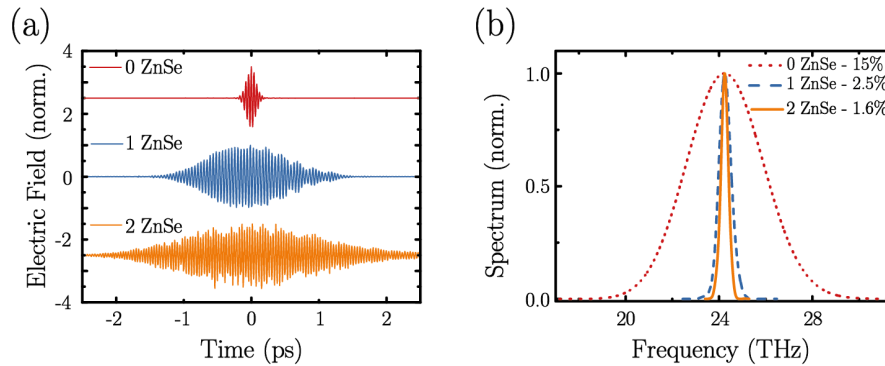
(a)

(b)

Figure D.3: Normalized EOS traces (a) and spectra (b) of the MIR pulses for different amounts of NIR chirp. The data in panel (a) are offset for clarity. The percentage in the legend of panel (b) indicates the relative bandwidth $\Delta\omega/\omega_0$.

The time-frequency Wigner maps of the NIR pulses before (a) and after (b) stretching with one ZnSe rod, retrieved from frequency-resolved optical gating (FROG) measurements [79] are shown in Fig. D.2. After inserting ZnSe rods of thickness L_I and L_{II}, as expected, the time-frequency traces of both the NIR pulses became parallel to each other and to the dashed line, which represents the frequency chirp with GDD = 22500 fs^2 and TOD = 20000 fs^3.

Figure D.3a shows the MIR pulses obtained by DFG of the NIR pulses in the different stretching configurations. Stretching the NIR pulses by one or two pairs of ZnSe rods results in an increase in MIR pulse duration from 0.12 to 0.92 and 1.65 ps, concomitant with a bandwidth reduction from 15% $\Delta\omega/\omega_0$ to 2.5% and 1.6%, respectively, as shown in Fig. D.3b.

The two stretching steps reduced the bandwidth to 16% and 10% of the starting value, respectively. For spectral filtering techniques, this corresponds to the maximum theoretical energy efficiency, without keeping into account further losses introduced by the optical elements. Here, the energy

efficiency was 35% and 15% , respectively. This efficiency, already much higher compared to spectral filtering, could in principle be increased by employing thicker MIR generation crystals. This would however be detrimental for the generation of the broadband pulses, and would therefore limit the possibility of switching between the broadband and narrowband MIR generation configurations.
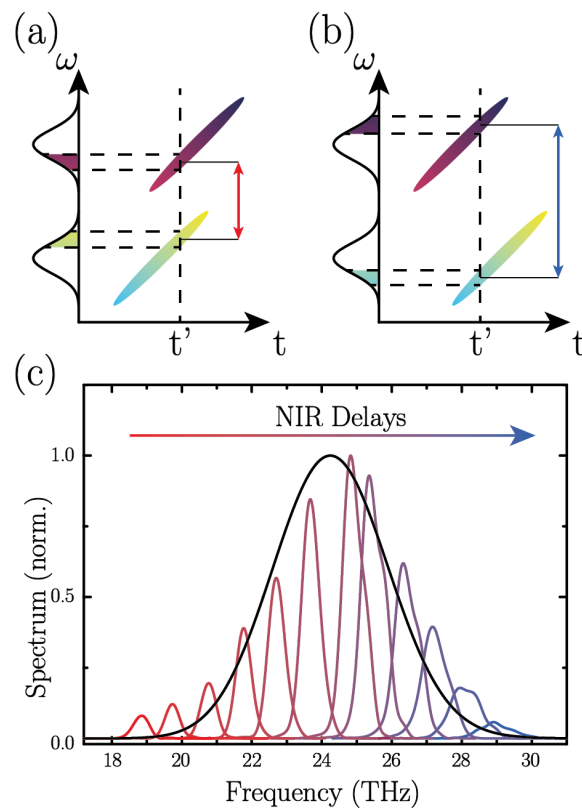
Figure D.4: Delay-dependent frequency tuning. NIR pulses delays that allow for the interaction of the closest (a) and farthest (b) frequency components. (c) Black line: spectrum of the broadband MIR pulse generated from TL NIR light (taken from Fig. D.3). Color lines: spectra of the MIR pulses obtained for different NIR pulses delays, normalized to their relative intensity.

Delay-dependent frequency tuning of the MIR output is reported in Fig.

D.4c, where the colored lines depict the narrow spectra obtained for different NIR pulse delays (with one ZnSe rod pair), rescaled according to the relative measured energy. If the delay between the incoming pulses is changed, the DFG frequency changes [75], because the subset of frequencies that can interact at any time t' in the DFG is shifted. An illustrative example is shown in Fig. D.4a where the delay between the NIR pulses is such that only the frequencies close to each other (red arrow) interact. Similarly, Fig. D.4b shows the situation where the pulse delay only allows for the interaction of the NIR frequency components farther from each other (blue arrow), resulting in a MIR central wavelength on the high-frequency wing of the corresponding broadband pulse.

Role of the author

This thesis is the results of the author's work as a graduate student at the Max Planck Institute for the Structure and Dynamics of Matter, within the Quantum Condensed Matter Dynamics division and at the University of Hamburg.

The project at the core of this thesis was conceived by Andrea Cavalleri.

The model for the nonlinear response of an infrared active mode in a dielectric presented in chapter 2 was developed by the author together with Michael Fechner, with help from Tobia Nova and under the guidance of Andrea Cavalleri and Roberto Merlin. The static DFT calculations were performed by Michael Fechner.

The experiments reported in chapter 3 were performed by the author together with Tobia Nova. The sources used for the generation of the pump and probe pulses were built by the author, with help from Tobia Nova. The source for the short pulses required to characterize the mid-infrared ones was built by Alice Cantaluppi together with the author. The data analysis was performed by the author.

The simulations reported in chapter 4 were performed exclusively by the author. The basic FDTD algorithm and the inclusion of the phonon resonance are based on the books and resources referenced in the chapter and relative appendix. The nonlinear equations of the model presented in chapter 2 were implemented in the FDTD loop by the author, who also developed the Matlab code for the simulation of the pump-probe response.

List of publications

The results presented on the main body of this thesis are based on the following publication:

- **A . Cartella**, T. F. Nova, M. Fechner, R. Merlin and A. Cavalleri, *Parametric amplification of optical phonons*, arXiv:1708.09231 (2017).

The optical developments presented in appendices C and D are based on the papers:

- **A . Cartella**, S. Bonora, M. Först, G. Cerullo, A. Cavalleri, and C. Manzoni, *Pulse shaping in the mid-infrared by a deformable mirror*, Optics Letters 39, 1485 (2014).

- **A . Cartella**, T. F. Nova, A. Oriana, G. Cerullo, M. Först, C. Manzoni and A. Cavalleri, *Narrowband carrier-envelope phase stable mid-infrared pulses at wavelengths beyond 10 μm by chirped-pulse difference frequency generation*, Optics Letters 42, 663 (2017).

Additional publications:

- T. F. Nova, **A. Cartella**, A. Cantaluppi, M. Först, D. Bossini, R. V. Mikhaylovskiy, A. V. Kimel, R. Merlin, A. Cavalleri, *An effective magnetic field from optically driven phonons*, Nature Physics 13, 132 (2017).

- B. Liu, H. Bromberger, **A. Cartella**, T. Gebert, M. Först, A. Cavalleri, *Generation of narrowband, high-intensity, carrier-envelope phase stable pulses tunable between 4 and 18 THz*, Optics Letters 42, 129 (2017).

- R. Singla, G. Cotugno, S. Kaiser, M. Först, M. Mitrano, H. Y. Liu, **A. Cartella**, C. Manzoni, H. Okamoto, T. Hasegawa, S. R. Clark, D. Jaksch, and A. Cavalleri, *THz-Frequency Modulation of the Hubbard U in an Organic Mott Insulator*, Physical Review Letters 115, 187401 (2015).

Acknowledgements

First of all I would like to thank my supervisor Prof. Andrea Cavalleri for giving me the opportunity of working in his group. Thank you for the patience, for the many advices, and for pushing me often out of my comfort zone, making me do things I didn't think I was capable of.

My great gratitude goes also to Dr. Michael Först for teaching me a lot about both physics and optics. Thanks for the tricks you thought me in the lab, for the countless times you made intelligible something I wrote and for the continuous help throughout the years.

I also want to thank the many people that shared part of my journey at the MPSD, some even before it became an institute, and helped me go through the good days as well as through the bad ones. Thanks in random order to Alberto, Yannis, Andrea Caviglia, Michael Fechner, Hubertus, Sven, Regina, Daniele, Alex, Srivats, Mariana, Ankit, Gregor, Ivanka, Thomas, Luca, Rashmi, Stefan, Razvan.

The PhD has also been the first long period of my life spent away from my family. I want to thank Alice, Francesca, Maria, Eliza, Matthias, Michele, Matteo, Jasone and Hauke for giving me another one. Some of you I can count among the friends, and some also among the colleagues. The truth is, to me you are all much more than that. Thank you for the dinners, the serious discussions, the "not so serious" discussions, the drinking, the partying, the Fischmarkts.

I emphatically thank my parents for supporting me during the last 32 years of my life. The last ones have been particularly tough for you, and me being abroad surely did not make things easier. Thank you for having constantly believed in me and helped me improve.

A special thank you goes to Tobia, for being the closest thing to a brother I ever had. Thank you also for the help in the lab, but that is just a small thing compared to the rest.

"Thanks to Elena, who has changed my life in a completely natural and at the same time radical way; I hope she will continue to do so for a long time to come" were the last words of my master thesis. Since then, a long time has passed and many things changed in our lives, but my hope is still the same.

Bibliography

[1] O. Svelto, *Principles of Lasers.* Boston, MA: Springer US, 2010.

[2] R. W. Boyd, *Nonlinear Optics Third Edition.* 2001.

[3] S. O. Demokritov, V. E. Demidov, O. Dzyapko, G. A. Melkov, A. A. Serga, B. Hillebrands, and A. N. Slavin, "Bose-Einstein condensation of quasi-equilibrium magnons at room temperature under pumping," *Nature*, vol. 443, pp. 430–433, sep 2006.

[4] T. Brächer, P. Pirro, and B. Hillebrands, "Parallel pumping for magnon spintronics: Amplification and manipulation of magnon spin currents on the micron-scale," *Physics Reports*, vol. 699, pp. 1–34, 2017.

[5] G. A. Garrett, A. G. Rojo, A. K. Sood, J. F. Whitaker, and R. Merlin, "Vacuum Squeezing of Solids: Macroscopic Quantum States Driven by Light Pulses," *Science*, vol. 275, pp. 1638–1640, mar 1997.

[6] F. Benatti, M. Esposito, D. Fausti, R. Floreanini, K. Titimbo, and K. Zimmermann, "Generation and detection of squeezed phonons in lattice dynamics by ultrafast optical excitations," *New Journal of Physics*, vol. 19, no. 2, 2017.

[7] G. Venkataraman, "Soft modes and strucutral phase transitions," *Bulletin of Materials Science*, vol. 1, no. December, p. 1979, 1979.

[8] L. C. M. Miranda, "Phonon damping in the simultaneous presence of intense radiation and magnetic fields," *Journal of Physics C: Solid State Physics*, vol. 9, pp. 2971–2976, aug 1976.

[9] O. A. C. Nunes, "Amplification of acoustic lattice vibrations by electrons in semiconductors under intense laser radiation," *Journal of Applied Physics*, vol. 56, pp. 2694–2696, nov 1984.

[10] O. A. C. Nunes, "Carrier-assisted laser pumping of optical phonons in semiconductors under strong magnetic fields," *Physical Review B*, vol. 29, pp. 5679–5682, may 1984.

[11] K. Shinokita, K. Reimann, M. Woerner, T. Elsaesser, R. Hey, and C. Flytzanis, "Strong Amplification of Coherent Acoustic Phonons by Intraminiband Currents in a Semiconductor Superlattice," *Physical Review Letters*, vol. 116, p. 075504, feb 2016.

[12] R. P. Beardsley, A. V. Akimov, M. Henini, and A. J. Kent, "Coherent terahertz sound amplification and spectral line narrowing in a stark ladder superlattice," *Physical Review Letters*, vol. 104, no. 8, pp. 1–4, 2010.

[13] L. G. Tilstra, A. F. Arts, and H. W. De Wijn, "Optically excited ruby as a saser: Experiment and theory," *Physical Review B - Condensed Matter and Materials Physics*, vol. 76, no. 2, pp. 1–13, 2007.

[14] W. Liang, K. T. Tsen, O. F. Sankey, S. M. Komirenko, K. W. Kim, V. A. Kochelap, M. C. Wu, C. L. Ho, W. J. Ho, and H. Morkoç, "Observation of optical phonon instability induced by drifting electrons in semiconductor nanostructures," *Applied Physics Letters*, vol. 82, no. 12, pp. 1968–1970, 2003.

[15] M. Först, R. I. Tobey, S. Wall, H. Bromberger, V. Khanna, a. L. Cavalieri, Y.-D. Chuang, W. S. Lee, R. Moore, W. F. Schlotter, J. J. Turner, O. Krupin, M. Trigo, H. Zheng, J. F. Mitchell, S. S. Dhesi, J. P. Hill, and A. Cavalleri, "Driving magnetic order in a manganite by ultrafast lattice excitation," *Physical Review B*, vol. 84, p. 241104, dec 2011.

[16] M. Först, A. D. Caviglia, R. Scherwitzl, R. Mankowsky, P. Zubko, V. Khanna, H. Bromberger, S. B. Wilkins, Y.-D. Chuang, W. S. Lee, W. F. Schlotter, J. J. Turner, G. L. Dakovski, M. P. Minitti, J. Robinson, S. R. Clark, D. Jaksch, J.-M. Triscone, J. P. Hill, S. S. Dhesi, and A. Cavalleri, "Spatially resolved ultrafast magnetic dynamics initiated at a complex oxide heterointerface.," *Nature materials*, vol. 14, no. 9, pp. 883–8, 2015.

[17] D. Fausti, R. I. Tobey, N. Dean, S. Kaiser, a. Dienst, M. C. Hoffmann, S. Pyon, T. Takayama, H. Takagi, and a. Cavalleri, "Light-induced superconductivity in a stripe-ordered cuprate.," *Science (New York, N.Y.)*, vol. 331, pp. 189–91, jan 2011.

[18] S. Kaiser, C. R. Hunt, D. Nicoletti, W. Hu, I. Gierz, H. Y. Liu, M. Le Tacon, T. Loew, D. Haug, B. Keimer, and A. Cavalleri, "Optically induced coherent transport far above Tc in underdoped YBa2Cu2O6+x," *Physical Review B*, vol. 89, p. 184516, may 2014.

[19] W. Hu, S. Kaiser, D. Nicoletti, C. R. Hunt, I. Gierz, M. C. Hoffmann, M. Le Tacon, T. Loew, B. Keimer, and A. Cavalleri, "Optically enhanced coherent transport in YBa2Cu3O6.5 by ultrafast redistribution of interlayer coupling," *Nature Materials*, vol. 13, pp. 705–711, may 2014.

[20] M. Mitrano, a. Cantaluppi, D. Nicoletti, S. Kaiser, a. Perucchi, S. Lupi, P. Di Pietro, D. Pontiroli, M. Riccò, S. R. Clark, D. Jaksch, and a. Cavalleri, "Possible light-induced superconductivity in K3C60 at high temperature.," *Nature*, vol. 530, no. 7591, pp. 461–464, 2016.

[21] M. Rini, R. Tobey, N. Dean, J. Itatani, Y. Tomioka, Y. Tokura, R. W. Schoenlein, and A. Cavalleri, "Control of the electronic phase of a manganite by mode-selective vibrational excitation," *Nature*, vol. 449, pp. 72–74, sep 2007.

[22] A. D. Caviglia, R. Scherwitzl, P. Popovich, W. Hu, H. Bromberger, R. Singla, M. Mitrano, M. C. Hoffmann, S. Kaiser, P. Zubko, S. Gariglio, J.-M. Triscone, M. Först, and A. Cavalleri, "Ultrafast Strain Engineering in Complex Oxide Heterostructures," *Physical Review Letters*, vol. 108, p. 136801, mar 2012.

[23] T. F. Nova, A. Cartella, A. Cantaluppi, M. Först, D. Bossini, R. V. Mikhaylovskiy, A. V. Kimel, R. Merlin, and A. Cavalleri, "An effective magnetic field from optically driven phonons," *Nature Physics*, vol. 13, pp. 132–136, oct 2017.

[24] M. Först, C. Manzoni, S. Kaiser, Y. Tomioka, Y. Tokura, R. Merlin, and A. Cavalleri, "Nonlinear phononics as an ultrafast route to lattice control," *Nature Physics*, vol. 7, pp. 854–856, aug 2011.

[25] A. Subedi, A. Cavalleri, and A. Georges, "Theory of nonlinear phononics for coherent light control of solids," *Physical Review B*, vol. 89, p. 220301, jun 2014.

[26] M. Först, R. Mankowsky, and a. Cavalleri, "Mode-Selective Control of the Crystal Lattice.," *Accounts of chemical research*, jan 2015.

[27] R. Mankowsky, M. Först, and A. Cavalleri, "Non-equilibrium control of complex solids by nonlinear phononics," *Reports on Progress in Physics*, vol. 79, p. 064503, jun 2016.

[28] A. von Hoegen, R. Mankowsky, M. Fechner, M. Först, and A. Cavalleri, "Probing the Interatomic Potential of Solids by Strong-Field Nonlinear Phononics," *arXiv*, 2017.

[29] J. N. Hodgson, *Optical Absorption and Dispersion in Solids*. Boston, MA: Springer US, 1971.

[30] W. G. Spitzer, D. Kleinman, and D. Walsh, "Infrared Properties of Hexagonal Silicon Carbide," *Physical Review*, vol. 113, pp. 127–132, jan 1959.

[31] L. Patrick and W. J. Choyke, "Static Dielectric Constant of SiC," *Physical Review B*, vol. 2, pp. 2255–2256, sep 1970.

[32] K. Huang, "On the interaction between the radiation field and ionic crystals," *Proc. Roy. Soc*, vol. 208, no. A, pp. 352–365, 1951.

[33] M. Born and K. Huang, "Dynamical theory of crystal lattices."

[34] H. J. Round, "A note on carborundum," *Electrical World*, vol. 19, p. 309, 1907.

[35] K. V. Emtsev, F. Speck, T. Seyller, L. Ley, and J. D. Riley, "Interaction, growth, and ordering of epitaxial graphene on SiC{0001} surfaces: A comparative photoelectron spectroscopy study," *Physical Review B - Condensed Matter and Materials Physics*, vol. 77, no. 15, pp. 1–10, 2008.

[36] S. C. Howells and L. a. Schlie, "Transient terahertz reflection spectroscopy of undoped InSb from 0.1 to 1.1 THz," *Applied Physics Letters*, vol. 69, no. 4, p. 550, 1996.

[37] T. I. Jeon and D. Grischkowsky, "Characterization of optically dense, doped semiconductors by reflection THz time domain spectroscopy," *Applied Physics Letters*, vol. 72, no. 23, pp. 3032–3034, 1998.

[38] A. Pashkin, M. Kempa, H. Němec, F. Kadlec, and P. Kužel, "Phase-sensitive time-domain terahertz reflection spectroscopy," *Review of Scientific Instruments*, vol. 74, no. 11, pp. 4711–4717, 2003.

[39] S. Nashima, O. Morikawa, K. Takata, and M. Hangyo, "Measurement of optical properties of highly doped silicon by terahertz time domain reflection spectroscopy," *Applied Physics Letters*, vol. 79, no. 24, pp. 3923–3925, 2001.

[40] M. Khazan, R. Meissner, and I. Wilke, "Convertible transmission-reflection time-domain terahertz spectrometer," *Review of Scientific Instruments*, vol. 72, no. 8, pp. 3427–3430, 2001.

[41] M. C. Beard, G. M. Turner, and C. A. Schmuttenmaer, "Size-Dependent Photoconductivity in CdSe Nanoparticles as Measured by Time-Resolved Terahertz Spectroscopy," *Nano Letters*, vol. 2, no. 9, pp. 983–987, 2002.

[42] J. T. Kindt and C. a. Schmuttenmaer, "Theory for determination of the low-frequency time-dependent response function in liquids using time-resolved terahertz pulse spectroscopy," *Journal of Chemical Physics*, vol. 110, no. 1999, pp. 8589–8596, 1999.

[43] C. Manzoni, M. Först, H. Ehrke, and A. Cavalleri, "Single-shot detection and direct control of carrier phase drift of midinfrared pulses.," *Optics letters*, vol. 35, pp. 757–9, mar 2010.

[44] K. Iwaszczuk, D. G. Cooke, M. Fujiwara, H. Hashimoto, and P. Uhd Jepsen, "Simultaneous reference and differential waveform acquisition in time-resolved terahertz spectroscopy," *Optics Express*, vol. 17, p. 21969, nov 2009.

[45] K. Yee, "Numerical solution of initial boundary value problems involving Maxwell's equations in isotropic media," 1966.

[46] U. S. Inan and R. A. Marshall, *Numerical Electromagnetics: The FDTD Method.* 2011.

[47] A. Taflove and S. C. Hagness, "Computational Electrodynamics: The Finite-Difference Time-Domain Method, Third Edition," 2005.

[48] M. Knap, M. Babadi, G. Refael, I. Martin, and E. Demler, "Dynamical Cooper pairing in nonequilibrium electron-phonon systems," *Physical Review B*, vol. 94, p. 214504, dec 2016.

[49] Y. Murakami, N. Tsuji, M. Eckstein, and P. Werner, "Nonequilibrium steady states and transient dynamics of conventional superconductors under phonon driving," *Physical Review B*, vol. 96, p. 045125, jul 2017.

[50] S. Dai, Z. Fei, Q. Ma, A. S. Rodin, M. Wagner, A. S. McLeod, M. K. Liu, W. Gannett, W. Regan, K. Watanabe, T. Taniguchi, M. Thiemens, G. Dominguez, A. H. C. Neto, A. Zettl, F. Keilmann, P. Jarillo-Herrero, M. M. Fogler, and D. N. Basov, "Tunable Phonon Polaritons in Atomi-

cally Thin van der Waals Crystals of Boron Nitride," *Science*, vol. 343, pp. 1125–1129, mar 2014.

[51] G. Cerullo, A. Baltuška, O. Mücke, and C. Vozzi, "Few-optical-cycle light pulses with passive carrier-envelope phase stabilization," *Laser and Photonics Reviews*, vol. 5, pp. 323–351, may 2011.

[52] D. W. Ward, *Polaritonics : An Intermediate Regime Between Electronics and.* PhD thesis, 2005.

[53] "Electromagnetic analysis using finte-difference time-domain," *http://emlab.utep.edu/ee5390fdtd - University of Texas - El Paso.*

[54] C. Ventalon, J. M. Fraser, M. H. Vos, A. Alexandrou, J.-L. Martin, and M. Joffre, "Coherent vibrational climbing in carboxyhemoglobin.," *Proceedings of the National Academy of Sciences of the United States of America*, vol. 101, pp. 13216–20, sep 2004.

[55] D. Strasfeld, S.-H. Shim, and M. Zanni, "Controlling Vibrational Excitation with Shaped Mid-IR Pulses," *Physical Review Letters*, vol. 99, p. 038102, jul 2007.

[56] A. Cartella, S. Bonora, M. Först, G. Cerullo, A. Cavalleri, and C. Manzoni, "Pulse shaping in the mid-infrared by a deformable mirror," *Optics Letters*, vol. 39, p. 1485, mar 2014.

[57] A. Weiner, "Femtosecond pulse shaping using spatial light modulators," *Review of scientific instruments*, vol. 71, no. 5, p. 1929, 2000.

[58] S.-H. Shim, D. B. Strasfeld, and M. T. Zanni, "Generation and characterization of phase and amplitude shaped femtosecond mid-IR pulses.," *Optics express*, vol. 14, pp. 13120–30, dec 2006.

[59] N. Belabas, J. P. Likforman, L. Canioni, B. Bousquet, and M. Joffre, "Coherent broadband pulse shaping in the mid infrared.," *Optics letters*, vol. 26, pp. 743–5, may 2001.

[60] T. Witte, K. Kompa, and M. Motzkus, "Femtosecond pulse shaping in the mid infrared by difference-frequency mixing," *Applied Physics B: Lasers and Optics*, vol. 76, pp. 467–471, apr 2003.

[61] H.-S. Tan, E. Schreiber, and W. S. Warren, "High-resolution indirect pulse shaping by parametric transfer.," *Optics letters*, vol. 27, pp. 439–41, mar 2002.

[62] H.-S. Tan and W. Warren, "Mid infrared pulse shaping by optical parametric amplification and its application to optical free induction decay measurement.," *Optics express*, vol. 11, pp. 1021–8, may 2003.

[63] R. A. Kaindl, M. Wurm, K. Reimann, P. Hamm, A. M. Weiner, and M. Woerner, "Generation , shaping , and characterization of intense femtosecond pulses tunable from 3 to 20 um," *Journal of the Optical Society of America*, vol. 17, no. 12, pp. 2086–2094, 2000.

[64] E. Zeek, K. Maginnis, S. Backus, U. Russek, M. Murnane, G. Mourou, H. Kapteyn, and G. Vdovin, "Pulse compression by use of deformable mirrors.," *Optics letters*, vol. 24, pp. 493–5, apr 1999.

[65] J. Garduño-Mejía, A. H. Greenaway, and D. T. Reid, "Programmable spectral phase control of femtosecond pulses by use of adaptive optics and real-time pulse measurement," *Journal of the Optical Society of America B*, vol. 21, no. 4, p. 833, 2004.

[66] D. Brida, G. Cirmi, C. Manzoni, S. Bonora, P. Villoresi, S. De Silvestri, and G. Cerullo, "Sub-two-cycle light pulses at 1.6 microm from an optical parametric amplifier.," *Optics letters*, vol. 33, pp. 741–3, apr 2008.

[67] A. Sell, A. Leitenstorfer, and R. Huber, "Phase-locked generation and field-resolved detection of widely tunable terahertz pulses with amplitudes exceeding 100 MV/cm.," *Optics letters*, vol. 33, pp. 2767–9, dec 2008.

[68] K.-H. Hong, J.-H. Kim, Y. Kang, and C. Nam, "Time frequency analysis of chirped femtosecond pulses using Wigner distribution function," *Applied Physics B*, vol. 74, pp. s231–s236, jun 2002.

[69] M. Först, R. Mankowsky, and A. Cavalleri, "Mode-Selective Control of the Crystal Lattice," *Accounts of Chemical Research*, vol. 48, pp. 380–387, feb 2015.

[70] A. Cartella, T. F. Nova, A. Oriana, G. Cerullo, M. Först, C. Manzoni, and A. Cavalleri, "Narrowband carrier-envelope phase stable midinfrared pulses at wavelengths beyond 10 μm by chirped-pulse difference frequency generation," *Optics Letters*, vol. 42, p. 663, feb 2017.

[71] D. W. McCamant, P. Kukura, S. Yoon, and R. A. Mathies, "Femtosecond broadband stimulated Raman spectroscopy: Apparatus and methods," *Review of Scientific Instruments*, vol. 75, no. 11, pp. 4971–4980, 2004.

[72] F. Raoult, A. C. L. Boscheron, D. Husson, C. Sauteret, A. Modena, V. Malka, F. Dorchies, and A. Migus, "Efficient generation of narrow-

bandwidth picosecond pulses by frequency doubling of femtosecond chirped pulses," *Optics Letters*, vol. 23, p. 1117, jul 1998.

[73] G. Veitas and R. Danielius, "Generation of narrow-bandwidth tunable picosecond pulses by difference-frequency mixing of stretched pulses," *Journal of the Optical Society of America B*, vol. 16, p. 1561, sep 1999.

[74] S. Wandel, M.-W. Lin, Y. Yin, G. Xu, and I. Jovanovic, "Bandwidth control in 5 um pulse generation by dual chirped optical parametric amplification," *Journal of the Optical Society of America B*, vol. 33, no. 8, p. 1580, 2016.

[75] F. O. Koller, K. Haiser, M. Huber, T. E. Schrader, N. Regner, W. J. Schreier, and W. Zinth, "Generation of narrowband subpicosecond mid-infrared pulses via difference frequency mixing of chirped near-infrared pulses," *Optics Letters*, vol. 32, p. 3339, nov 2007.

[76] B. Tatian, "Fitting refractive-index data with the Sellmeier dispersion formula," *Applied Optics*, vol. 23, p. 4477, dec 1984.

[77] N. P. Barnes and M. S. Piltch, "Temperature-dependent Sellmeier coefficients and coherence length for cadmium telluride," *Journal of the Optical Society of America*, vol. 67, no. 5, pp. 628–629, 1977.

[78] M. Bass, *Handbook of Optics, Third Edition Volume IV: Optical Properties of Materials, Nonlinear Optics, Quantum Optics*. third edit ed., 2009.

[79] R. Trebino, *Frequency-Resolved Optical Gating: The Measurement of Ultrashort Laser Pulses*. Kluwer Academic, 2000.